8-2016

Interaction between Charge-transfer States Studied by Magnetic Field Effects

Mingxing Li
University of Tennessee, Knoxville, mli21@vols.utk.edu

To the Graduate Council:

I am submitting herewith a dissertation written by Mingxing Li entitled "Interaction between Charge-transfer States Studied by Magnetic Field Effects." I have examined the final electronic copy of this dissertation for form and content and recommend that it be accepted in partial fulfillment of the requirements for the degree of Doctor of Philosophy, with a major in Materials Science and Engineering.

Bin Hu, Major Professor

We have read this dissertation and recommend its acceptance:

Roberto S. Benson, Zheng Gai, Brian K. Long

Accepted for the Council:

Carolyn R. Hodges

Vice Provost and Dean of the Graduate School

(Original signatures are on file with official student records.)

Interaction between Charge-transfer States Studied by Magnetic Field Effects

A Dissertation Presented for the

Doctor of Philosophy

Degree

The University of Tennessee, Knoxville

Mingxing Li

August 2016

Dedication

I dedicate this dissertation to my parents and my wife!

Acknowledgements

First, I am sincerely and heartily thankful to my advisor, Dr. Bin Hu, and my co-advisor Dr. Zheng Gai for their five years' guidance and valuable suggestions on my research work and dissertation. Without their guidance and support, I cannot acquire the enough theoretical and practical knowledge to finish this dissertation. I would also like to sincerely thank my committee members, Dr. Roberto S. Benson, and Dr. Brian K. Long, for their great help.

I should devote my deeply gratitude to my collaborator, Dr. Ilia Ivanov, at the Oak Ridge National Laboratory (ORNL) for his great help in providing facilities and discussions. I would also like to thank Dr. Min Wang and Dr. Long Y. Chiang from the University of Massachusetts for providing materials and fruitful discussions.

I owe my earnest thankfulness to my former and present colleagues in our lab for their instruction and discussions. They are Dr. Ming Shao, Dr. Liang Yan, Dr. Huidong Zang, Dr. Yu-Che Hsiao, Dr. Qing Liu, Hengxing Xu, Ting Wu and Miaosheng Wang. I need to express my thankfulness to the postdocs in our lab, Dr. Lei He, Dr. Dehua Hu, Dr. Hongfeng Wang and Dr. Wei Qin, for their numerous discussions and great support.

Finally, I particularly thank my wife Ying Zheng, my parents, and my parents in law and other family members in China for their great understanding and strong support during the five years in the graduate school.

Abstract

Organic semiconducting materials, consisting mostly of carbon and hydrogen atoms, provide remarkable promise for electronic applications due to their easy processing, chemical tenability, low costs and environmental-friendly characteristics. For realizing electronic applications such as light emitting diodes and photovoltaic cells, charge-transfer states act as an important intermediate state for recombination and dissociation. Interestingly, magnetic field effects on semiconducting materials have been realized based on the suppression of spin mixing in the charge-transfer states. Although lots of studies have been carried out on investigating the properties of charge-transfer states, little has been done to consider the interaction between them. This thesis aims to reveal the interaction between different kinds of charge-transfer states by using the magnetic field effects. Chapter 1 presents a basic introduction to the organic semiconducting materials and magnetic field effects. Chapter 2 gives a simple description of the experiment procedure, such as device fabrication, magnetic field effects measurement and data analysis. Chapter 3 studies the interaction between intermolecular charge-transfer states. Chapter 4 indicates the interaction between intramolecular charge-transfer states and d electrons. Chapter 5 illustrates the interaction between photo-generated and magnetized charge-transfer states. Chapter 6 introduces the interaction between excitons and free charge carriers in organo-metal halide perovskite materials. Chapter 7 performs the study of magneto-electronic interaction at the interface between Rashba perovskite and ferromagnetic metal. Finally, Chapter 8 gives a short conclusion for the entire study in this dissertation.

Table of Contents

List of Tables

List of Figures

CHAPTER 1
INTRODUCTION

This chapter provides the fundamental information about the organic semiconducting materials and magnetic field effects. Main information is focus on the properties of charge-transfer states and mechanisms of magnetic field effects. The motivation of this chapter is to give the correspondence information for the studies in the following chapters. Therefore, the readers whose background are not in this area would feel free to read this chapter.

1.1 Organic Semiconducting Materials

Organic semiconducting materials, showing semiconducting properties, mostly consist of carbon and hydrogen atoms. They can be divided into two categories: (1) small molecules (Figure 1) and (2) polymers (Figure 2), which has a well-defined molecular weight and structure and a long-chain molecule with repeat units respectively.

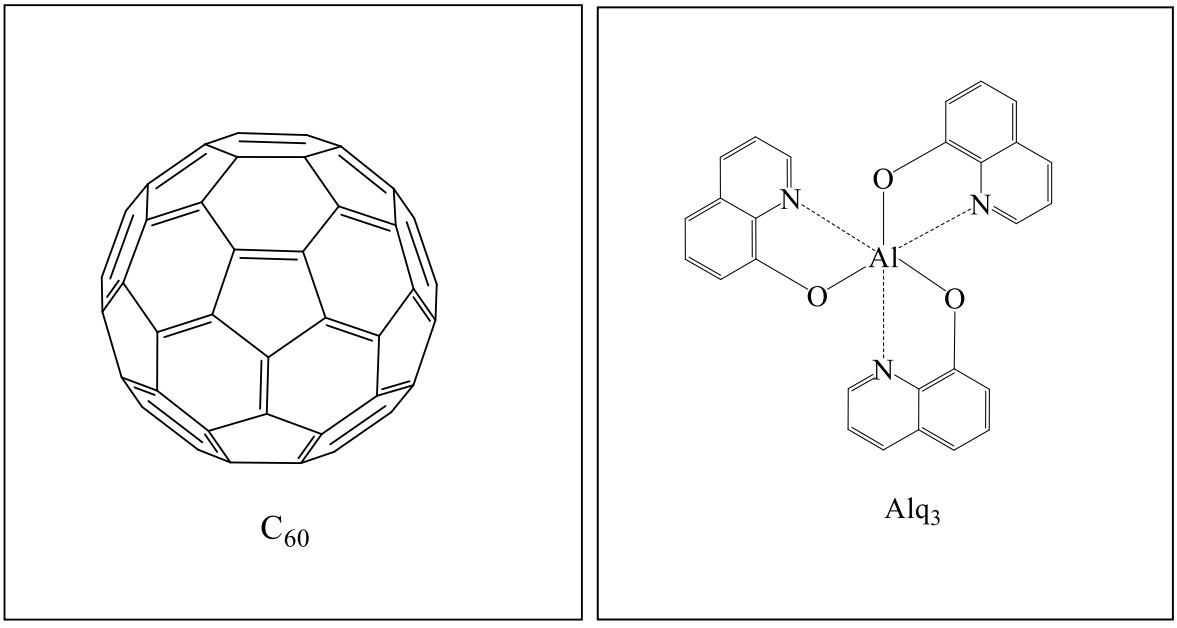

Figure 1 Chemical structures of small molecules: C_{60} and Alq_3.

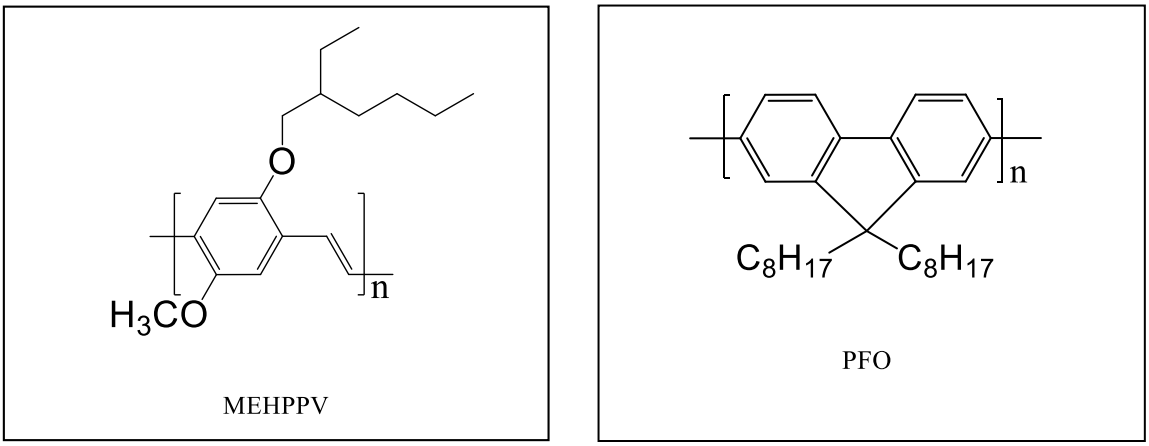

Figure 2 Chemical structures of polymers: P3HT and PFO.

1.1.1 History of organic semiconducting materials

Although organic materials are firstly well known for their electrically insulating properties due to a wide band gap, some specific organic materials were discovered with clear electrical conductivity in 1950s. It was in 1970s when A. J. Heeger, Alan MacDiarm and Hideki Shirakawa found that chemical doping can change the conductivity of organic materials over a full range from insulator to metal, attracting more and more chemists, physicists and engineers to work on the fabrication, fundamental physics and application of organic semiconducting materials.[1] Therefore, they were awarded the Nobel Prize in Chemistry in the year 2000 for "the discovery and development of conductive polymers". Nowadays, many companies have put the OLED into market for display application, which demonstrated the great potential application of organic semiconducting materials. Although comparing with the popular inorganic semiconductors, organic semiconducting materials still have problems such as short lifetime and low efficiency in OPV. However, the unique properties such as solubility, flexibility, and light weight, low cost and controllable bandgap predicts a bright future for organic semiconducting materials in application.[2-4]

1.1.2 Electronic structure of organic semiconducting materials

Organic semiconducting materials are π-conjugated, consisting of alternative single and double bonds along the chain of carbon atoms as shown in Figure 3 (a). Each carbon atom has three sp_2 and one p_z orbitals, forming σ-bonds through overlapping between neighbor carbon atom and hydrogen atom and π-bonds by overlapping with nearby p_z orbitals as shown in Figure 3 (b), respectively. The π-bonds lead to the delocalized π-electrons along the carbon chain in organic semiconducting materials, producing the conductivity. Generally, the occupied bonding π-bonds and empty anti-bonding π-bonds form molecule bonds that are comparable to the valence band and conductance band in inorganic semiconductors. The bonding π-orbital with the highest energy is called the highest occupied molecular orbital (HOMO), while the anti-bonding π-orbital with the lowest energy is called the lowest unoccupied molecular orbital (LUMO).[5, 6] The bandgap between HOMO and LUMO is usually in the range of 1.4-3.0 eV due to the Peierls distortion, generating the semiconducting properties of these organic materials.

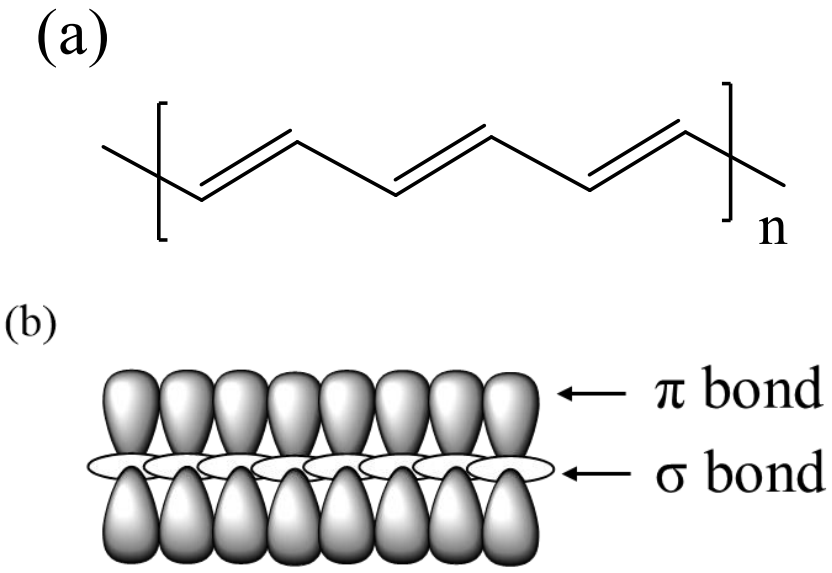

Figure 3 (a) Schematic view of the conjugated polymer backbone. (b) Electronic orbitals and bonds in conjugated carbon atoms.

In general, the organic materials are disordered or amorphous which means the long-range order is negligible between molecules or polymer segments. Due to the distortion and weak interaction between organic semiconducting molecules, the π-electrons are confined at a part of molecule or a segment of polymer. The energy of the site where the π-electrons are localized is also disordered as a Gaussian distribution with an energy difference of 75~150 meV[7, 8] because of the spatial disarray as shown in Figure 4. Consequently, charge carriers hop between localized sites by phonon-assisted tunneling, leading to a mobility with several orders smaller than that of inorganic semiconductors.

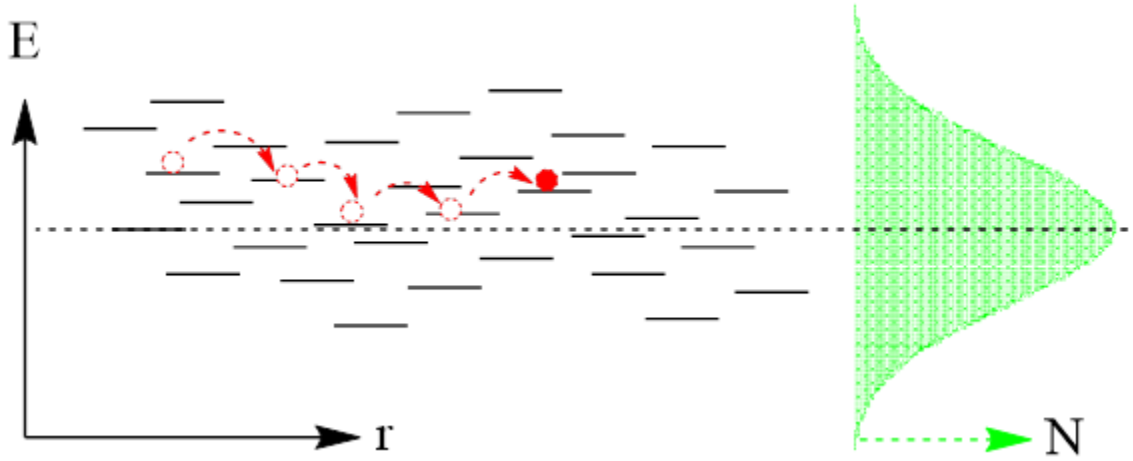

Figure 4 Disorder in the energy (E) of localized sites (left) and the distribution of sites per energy (N) follows a Gaussian density of states. The hopping of a carrier is illustrated by the red dashed arrows.

1.2 Excitations in Organic Semiconducting Materials

Upon photoexcitation and electrical injection, charged (polarons) or neutral (excitons) electronic excited states (excitations) are formed in π-conjugated organic semiconducting materials. Photoexcitation with the energy larger than the bandgap produces neutral and spinless excitations named as singlet excitons. They can either recombine to the ground states with an outcome of luminescence or transfer into a long-lived neutral excitation named triplet excitons through intersystem crossing. In addition,

they can dissociate into positive and negative charged excitations (polarons) with a spin of $\frac{1}{2}$, which can form another type of neutral excitations named polaron pairs. On the other hand, after the charge carriers are injected into organic semiconducting materials from the electrodes, they can transport as polarons, or combining with each other to form polaron pairs or excitons. In the following, we introduce these different types of excitations in organic semiconducting materials.

1.2.1 Polaron

It is known that organic materials are softer than inorganic materials because of the weak interaction between adjacent molecules or polymer chains originating from Van der Vaals forces. Consequently, the transportation of charge carriers in organic materials can distort the organic material, forming a quasi-particle named polaron as shown in Figure 5. Polaron is positively or negatively charged with a spin of $\frac{1}{2}$. Ascribing to the combination of charges and distortions, polarons are localized within the bandgap of organic semiconducting materials. The transportation of polaron is described by hopping process between different localized states.

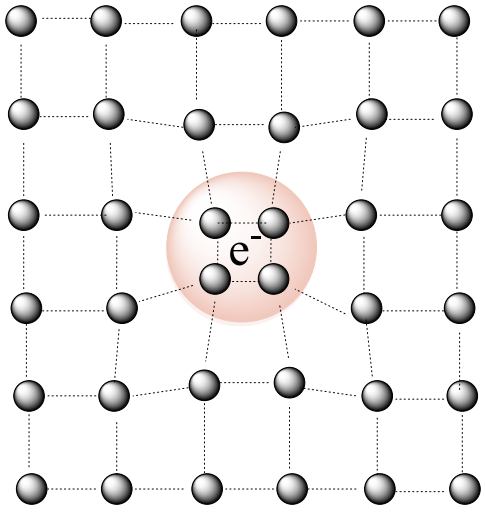

Figure 5 Schematic of polaron.

1.2.2 Polaron pair

When two oppositely charged polarons on neighbor molecules or polymer chains combining with each other through Coulomb interaction, a polaron pair is formed (Figure 6 (a)). It is the intermediate state of polarons and excitons. In optical excitation, polaron pairs derives from the relaxation of high energy singlet exciton at the interface between two molecules or polymer chains. They have the same spin state as the original singlet exciton, which is called geminate polaron pairs. Polaron pairs at the interface can also dissociate into polarons. When these polarons combines with each other through Coulomb interaction at the interface, they can again form polaron pairs with random spin configuration, named as non-geminate polaron pairs. In electrical excitation, injected electrons and holes are captured by Coulomb interaction to form non-geminate polaron pairs. Different from the germinate polaron pairs which have spin of 0, non-germinate polaron pairs can have singlet and triplet configuration with spin of 0 and 1 at a ratio of 1:3. Due to the energy difference between singlets and triplets, the intersystem crossing (ISC) occurs as shown in Figure 6 (b).

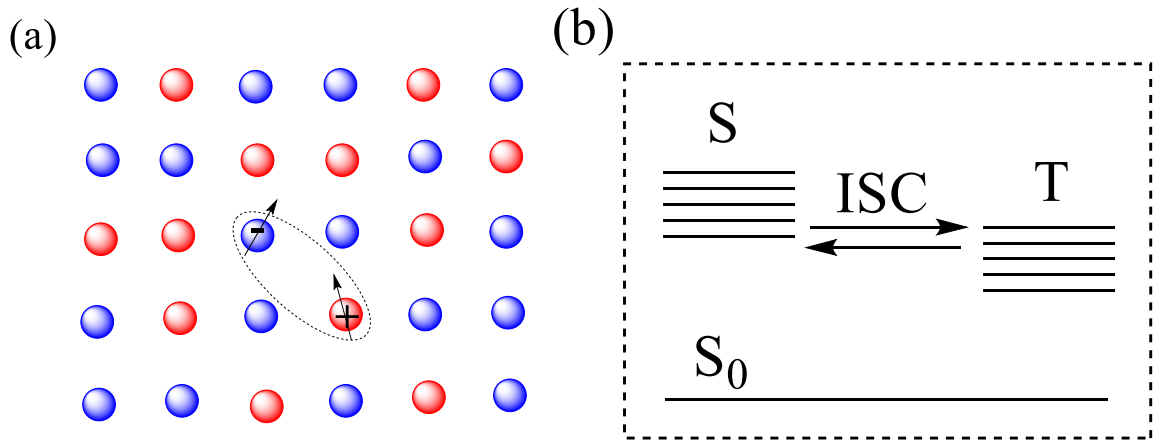

Figure 6 (a) Diagram of polaron pair. (b) Intersystem crossing between singlet and triplet.

1.2.3 Bipolaron

Comparing with polaron pairs who are constructed by oppositely charged polarons, bipolaron is formed by two polarons with the same charge on the same site which is shown in Figure 7. The bipolaron can either be two positive polarons (P+P+) or two negative polarons (P-P-), leading to a lower energy than that of each individual polaron.

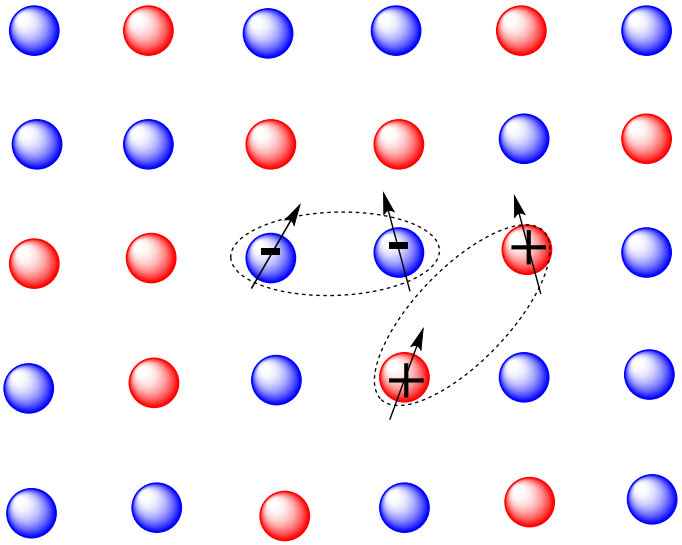

Figure 7. Diagram of bipolaron with P+P+ or P-P-.

1.2.4 Exciton

Excitons are electron-hole pairs combined by the Coulomb interaction between them in a single molecule or single polymer chain. Basically, the Coulomb interaction in excitons is stronger than that in the polaron pairs due to the short distance between electron and hole in exciton. Upon photoexcitation, singlet exciton is directly formed by promoting an electron from lower energy level to higher energy level as shown in Figure 8. This excitation causes a structural distortion of surroundings, leading to exciton binding energy round 0.3~0.5eV in most organic semiconducting materials. Due to the spin orbital coupling, hyperfine interaction or the impurities, singlet excitons can transfer into triplet excitons via intersystem crossing.

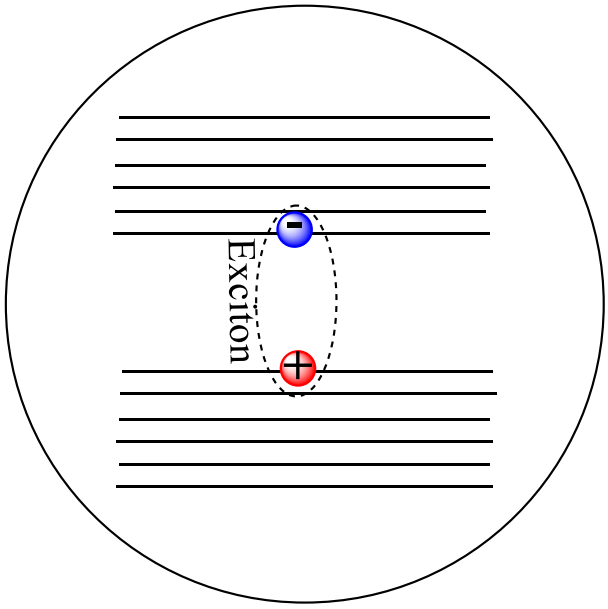

Figure 8 Diagram of exciton.

1.3 Spins in organic semiconducting materials

Nowadays, more and more enthusiasm on the research of spins arises because of the application of inorganic spintronics in read head and modern hard disk drive. Considering the spin states of polarons, polaron pairs, bipolarons and excitons in organic semiconducting materials, researchers have moved their attention of spin study into organic materials. On one hand, people find that organic semiconducting materials can be used as a space layer sandwiched by two different ferromagnetic electrodes for realization of GMR or TMR, leading to organic spintronics.[9, 10] On the other hand, people also notice that the electronic properties of organic semiconducting materials can be changed by an external magnetic field without coupling with ferromagnetic electrodes, leading to magnetic field effects.[11-26] The following paragraphs discuss these two effects in organic semiconducting materials.

1.3.1 Organic spintronics: GMR and TMR

Generally, the weak spin orbital coupling due to the absence of high-weight atoms in organic semiconducting materials generates a longer spin lifetime than that of inorganic semiconductors.[27, 28] Together with other properties such as cheap price, easy processing method and chemical tenability, organic semiconducting materials have attracted much attention on the research of spintronics. The spin injection into organic materials was first realized in 2002 by using a device with the structure of LSMO/sexithiophene/LSMO.[29] However, the correlation of the observed magnetoresistance in this device with the orientation of the magnetization is unclear at that time. In 2004, Xiong *et al*, reported the first organic spin valve by using small molecule Alq_3 as the space layer with 100 nm sandwiched by LSMO and Co as shown in Figure 9 (a). They observed a large resistance change with the value of 40% in Alq_3 when switching the magnetization direction of the ferromagnetic electrode, which is a clear characterization of giant magnetoresistance (GMR) (Figure 9 (b)). This experiment also demonstrates the long spin diffusion length in organic materials. After this discovery, many spin valves with the application of other molecules or polymers are carried out, proving the probability of organic spin valve in future application.[30-33]

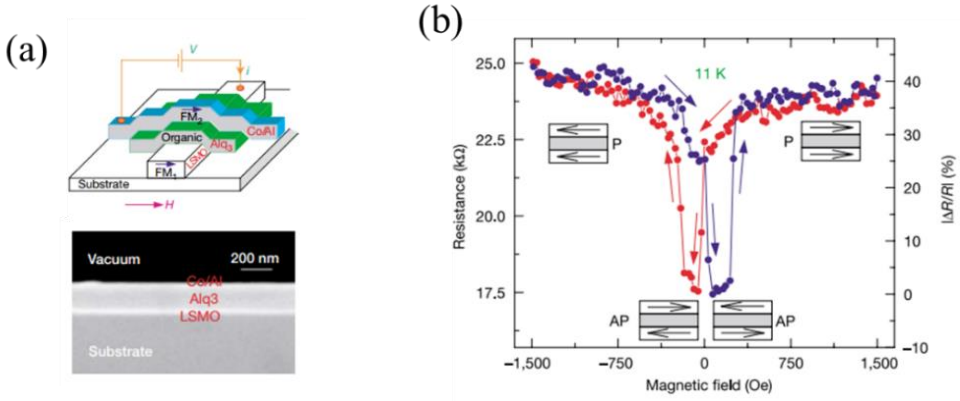

Figure 9 (a) The device structure and SEM image, (b) magnetoresistance of the first organic spin valve measurement by Xiong et al., measured on a LSMO/Alq_3/Co device at 11 K. Data adapted from Ref. 9.

Another approach to realize organic spin valve is to use a very thin organic layer as a tunnel layer to produce TMR.[10, 34-38] By comparing an Alq_3 layer with an inorganic tunnel layer Al_2O_3, researchers found that when Alq3 layer is very thin, charge carriers can tunnel through it to form a typical TMR device as shown in Figure 10. In conclusion, organic semiconducting materials have been proved for realization in spintronics, leading to a potential application in future data reading and storage.

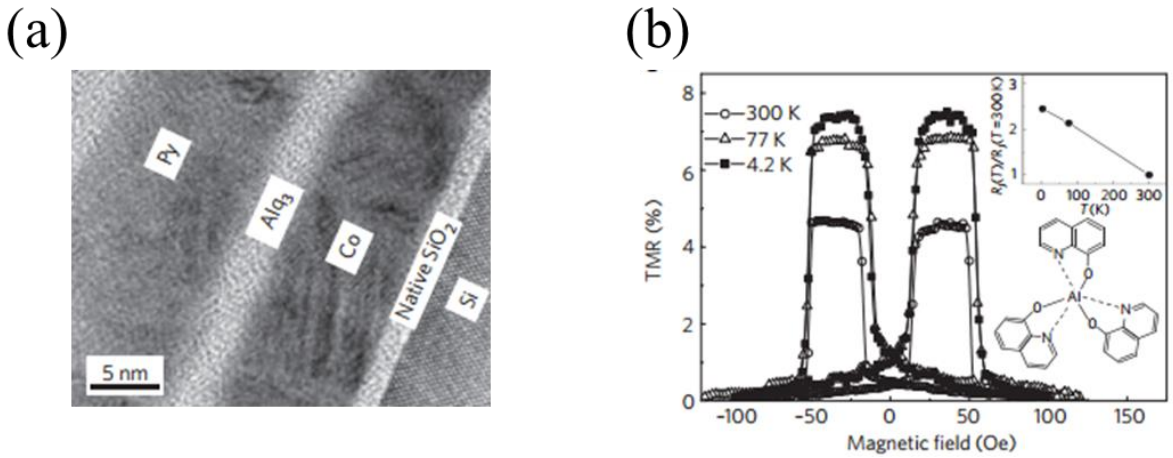

Figure 10 (a) HRTEM image of a magnetic tunnel junction with a thin (few nm) Alq_3 barrier. (b) TMR of the tunnel junction shown in (a). The inset shows the temperature dependence of TMR. Data adapted from Ref. 40.

1.3.2 Magnetic field effects

A long time before the realization of organic spin valve, magnetic field effects on chemical reaction and delayed photoluminescence had been discovered.[39-41] The magnetic field effects are defined as MFEs $= \frac{S_B - S_0}{S_0}$, where S_B and S_0 are signals with and without magnetic field. Researchers missed to pay much attention to this kind of phenomenon until 21st century when different groups over the world found that many properties of organic semiconducting materials, such as resistance, electroluminescence, photoluminescence, photocurrent and capacitance *et al.* can be changed by an external magnetic field without coupling with ferromagnetic electrode.[11-26] Wohlgenant group found that both molecule

and polymer shows a large magnetoresistance without ferromagnetic electrode at room temperature.[11] Further studies shown that this organic magnetoresistance (OMAR) changes with temperature, bias voltage, thickness of the organic semiconducting layer and also the device structure.[11, 20-22, 42-45] At the same time, Kalinowski et.al reported that the electroluminescence and current of Alq3 in an OLED device can be improved up to 5% and 3% respectively upon applying of an external magnetic field to 300 mT.[46] In addition, Frankevich found the change of photocurrent from PPV is enhanced up to several percentages by an external magnetic field.[47] Ito et.al also studied the photocurrent and luminescence of a doped photoconductive polymer films by applying a magnetic field, showing the magnetic field effects on photocurrent and luminescence.[48] Recently, Zang et.al discovered that magnetic field can even change the capacitance of an organic donor: acceptor bulk heterojunction under photoexcitation.[13, 14] Distinguished from spin valve, magnetic field effects on organic semiconducting materials observed at room temperature and small magnetic field are without the application of ferromagnetic electrodes. It is strongly believed that these magnetic field effects are related to the spin process in organic semiconducting materials. Even many mechanisms are proposed to explain these phenomena, however, there are still controversies between different models.

1.4 Mechanisms for magnetic field effects

Different models have been provided by various groups to explain the magnetic field effects. Generally, there are four major types of models. The first one is the polaron pair model which is related to the magnetic field sensitive intersystem crossing. The second one is bipolaron model relating to the carrier mobility mediated by hyperfine interaction. The third one is the spin dependent exciton interaction which includes excitons interaction and exciton charge interaction. The last one is Δg effect caused by the difference between g factors of electron and hole. Each mechanism is discussed in detail in the following.

1.4.1 Polaron pair model

The polaron pair mechanism originates from the spin mixing between the singlet and triplet polaron pairs which can be influenced by external magnetic field. The diagram of this mechanism is illustrated in Figure 11. When electrons and holes are combined by Coulomb interaction to form polaron pairs, the spin of electrons or holes can be flipped by the internal magnetic field from spin orbital coupling (SOC) or hyperfine interaction (HPI), leading to the spin mixing between singlet polaron pairs and triplet polaron pairs through intersystem crossing (ISC).[49-55] Generally, the energy difference between singlet polaron pairs and triplet polaron pairs is negligible without external magnetic field due to the small exchange energy caused by the large distance between electrons and holes. This leads the spin mixing occurs between singlet polaron pairs and triplet polaron pairs. After adding an external magnetic field, the triplets are split into three states with spin of +1, -1 and 0 due to the external Zeeman splitting. Therefore, spin mixing crossing only happens between singlet polaron pairs and the triplet polaron pairs with spin of 0. Consequently, the spin mixing is reduced by the external magnetic field, increasing the ratio between singlet and triplet. Together with the fact that singlet and triplet have different recombination outcome, dissociation rate and electric polarization, the electroluminescence, photoluminescence, current, photocurrent and capacitance can be changed by the external magnetic field.

1.4.2 Bipolaron model

Magnetic field effects were also found in unipolar devices which cannot be explained by polaron pair models since there are no polaron pairs formed. Bobbert proposed the bipolaron model to explain this phenomenon based on the changeable mobility of charge carriers due to the external magnetic field as shown in Figure 12.[23] In the bipolaron model, one polaron is assumed to be localized at one site while the other polarons with the same charge hop from other sites to this site. The two polarons with the opposite spins tend to form bipolaron due to the reduced energy while the two polarons with the same spins are blocked to form bipolaron because Pauli Exclusion Principle. Therefore, they allow or disallow carriers to pass the site to contribute the current. The spin

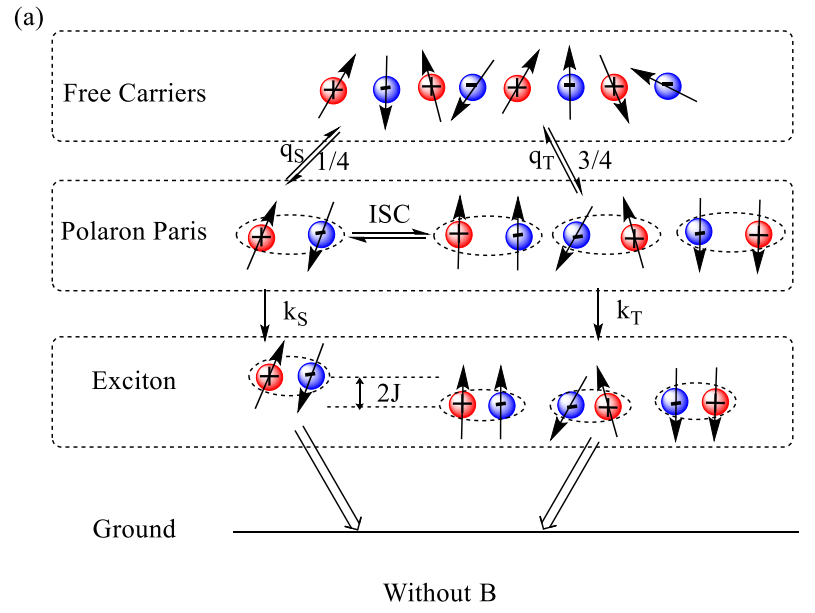

Figure 11 (a) Diagram of possible routes for recombination of free electrons and holes to the ground state with (a) and without (b) magnetic field.

of electrons or holes processes around the hyperfine field when there is no external magnetic field, leading to a mixing between formations and blocking of the bipolarons. Applying an external magnetic field affects the procession of spins with an outcome of more parallel spins. Consequently, the spin blocking is increased, leading to positive magnetoresistance. On the other hand, the formation of bipolaron reduces the mobility of free carrier for carrying the current. Therefore, the reduction of bipolaron formation can increase the mobility of free carriers to improve the current, producing a negative magnetoresistance. Therefore, it is possible to get the magnetic field effects with different signs based on the bipolaron mechanism. The sign of the magnetoresistance based on bipolaron model is determined by the density of free carriers and the branch ratio between the hopping rate and the formation rate of bipolaron.

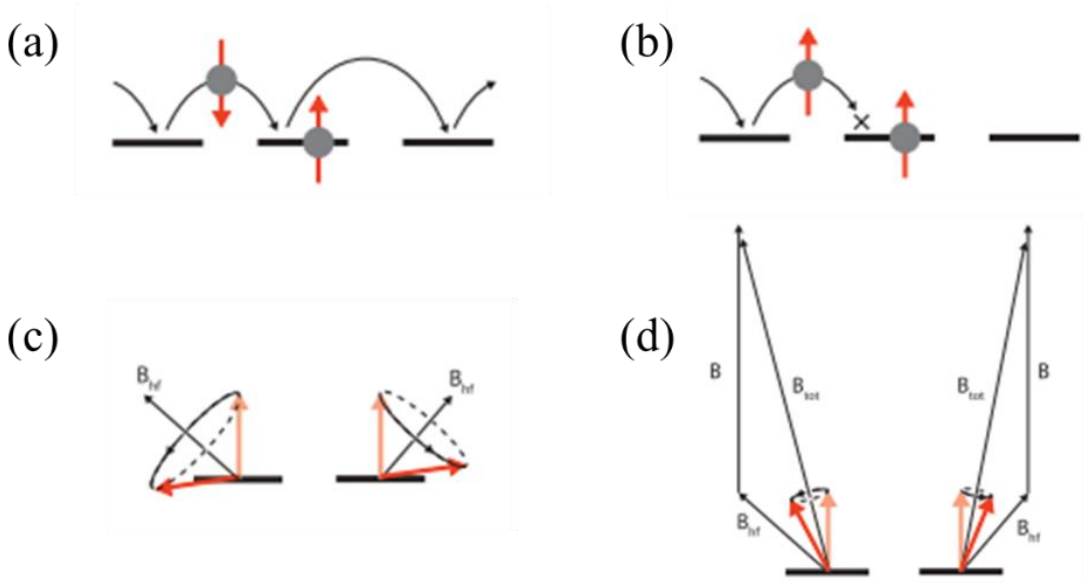

Figure 12 (a, b) The effect of spin-blocking during bipolaron formation. Two polarons with parallel spins cannot form a bipolaron. (c, d) Illustration of spin precession in bipolaron with (c) only the local hyperfine fields or (d) in the total field from the sum of the local hyperfine field and the external magnetic field. Data adapted from Ref. [56].

1.4.3 Exciton model

After the formation of excitons by tightly bonding electrons and holes, the excitons diffuse in organic semiconducting materials. During this process, excitons collide with other excitons and free charge carriers or trapped charge carriers, leading to the exciton-exciton interaction and exciton-charge interaction respectively.[25, 41, 57] Generally, both singlet excitons and triplet excitons can involve into these interactions. However, the triplet excitons dominate these two process due to their long lifetime, namely triplet-triplet annihilation and triplet-charge reaction respectively.

Triplet-triplet interaction is described in Figure 13. Two triplets interact with each other to form an intermediate state (TT) with a rate of k_1. The intermediate state (TT) on one hand can dissociate into two triplets with a rate of k_{-1}, and on the other hand can annihilate into a ground singlet S_0 and an excited singlet S* with a rate of k_2, which produces the delayed fluorescence. The intermediate state (TT) has nine spin states according to the spin orientation: one singlet state, three triplet states and five quintet states. Similar to the polaron pair model, an external magnetic field can change the spin mixing of the intermediate states (TT), resulting in a change in annihilation rate of k_2. Consequently, the singlet states in the outcome of the triplet-triplet annihilation is changed, leading to magnetic field effects.

$$T+T \underset{k_{-1}}{\overset{k_1}{\rightleftharpoons}} (TT) \xrightarrow{k_2} S^*+S_0$$

$$(TT) \begin{cases} (TT)^5 \\ (TT)^3 \\ (TT)^1 \end{cases}$$

Figure 13 Diagram for triplet-triplet interaction.

Triplet-charge reaction can be expressed in Figure 14. Triplet exciton can interact with a free charge carrier or a trapped charge carrier to form a (TD) intermediate state with rate of k_1. The intermediate state (TD) can annihilate the triplet into a ground singlet state (S_0) and a new free carriers (D) with a rate of k_2. Additionally, they can dissociate back into the originate state with rate of k_{-1}. According to the spin orientation, intermediate state (TD) has six spin states: two doublets and four quartets. Only the intermediate state with doublet spin configuration undergo the annihilation to produce ground singlet state and free carriers. An external magnetic field can change the doublet intermediate states with an outcome of changing reaction rate. Therefore, the property of organic semiconducting materials is changed. Recently, it was also proposed that the quenching of triplet or the free charge scattering caused by the triplet-charge reaction can be changed by the external magnetic field, leading to a change of charge mobility to generate magnetoresistance. The researchers found that reducing the triplet concentration through intersystem crossing under magnetic field increases the charge mobility by weakening the triplet-charge reaction, generating a negative magnetoresistance.

$$T+D \underset{k_{-1}}{\overset{k_1}{\rightleftharpoons}} (TD) \xrightarrow{k_2} S_0+D$$

$$(TD) \begin{cases} (TD)^4 \\ \\ (TD)^2 \end{cases}$$

Figure 14 Diagram for triplet-charge interaction.

1.4.4 Δg model

It is known that electrons and holes have different g values. Therefore, electrons and holes process around the magnetic field with a different frequency of $g_e\mu_B B/\hbar$ and $g_h\mu_B B/\hbar$. Consequently, singlet and triplet polaron pairs are formed due to the difference in precision frequencies, i.e. $\Delta g\mu_B B/\hbar$, where $\Delta g=g_e-g_h$. Apparently, applying an external magnetic field can directly change the difference in precision frequencies, leading to the change of singlet/triplet ratio as shown in Figure 15.[58-60] Therefore, the magnetic field effects are produced by combing the different properties of singlets and triplets such as recombination rate, dissociation rate and so on.

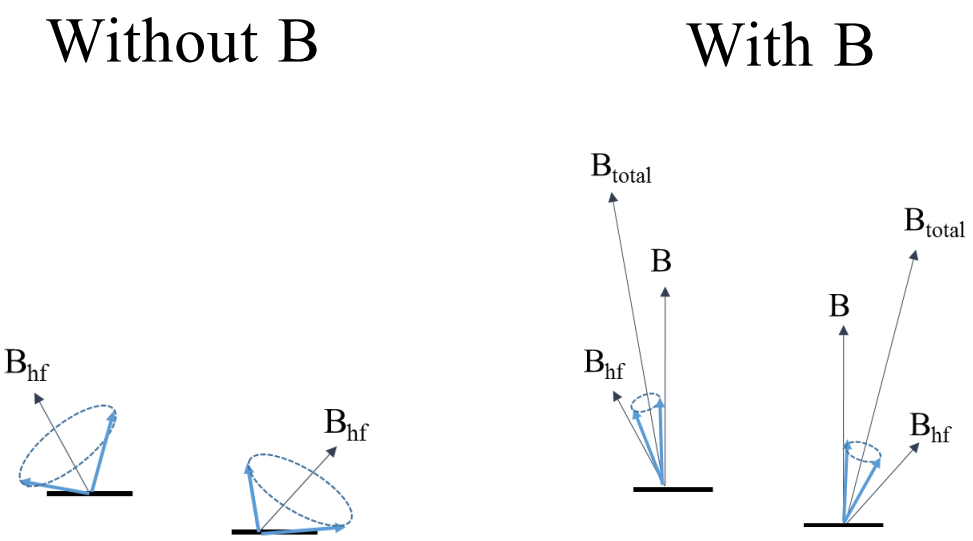

Figure 15 Diagram for Δg model.

1.5 Organo-metal Halide Perovskite

In recent years, the organo-metal halide perovskites with the structure of ABX_3 as shown in Figure 16, where A as the organic molecules, B as the lead and X as the halide atoms, have attracted tremendous attention due to their excellent optical and electronic properties for realizing the photovoltaics and optoelectronic devices.[61-71]

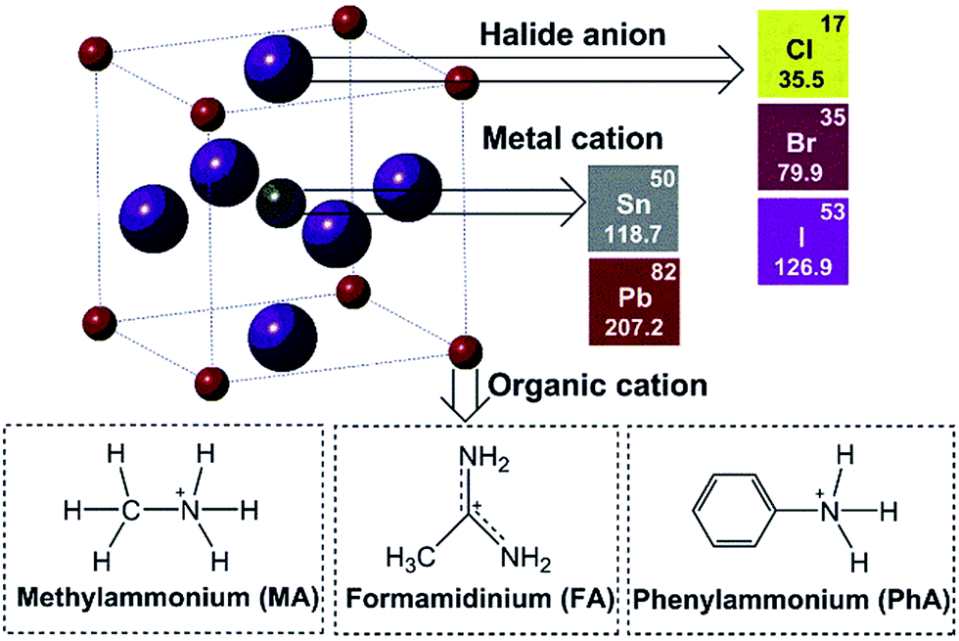

Figure 16 crystal structure of ABX_3.

Over the past 6 years, the power conversion efficiencies (PCE) of perovskite photovoltaic cells have boosted from ~3% to >20%.[72-75] This excellent achievement is based on their near-optimal direct band gap,[72, 76] high optical absorption,[73, 77] high carrier mobility,[74, 78-82] long carrier diffusion length,[83, 84] and its spontaneous electronic polarization.[85-88] In addition, these materials are also found to perform greatly in light emitting diode. Besides the characteristic of tunable wavelength in light emitting diode devices made from these perovskites, researchers discovered the wavelength-tunable lasing phenomenon from the perovskites with low lasing thresholds and high quality factors at room temperature.[89] Interestingly, the photodetectors built from the perovskite materials were demonstrated recently, with the detection wavelength changing from infrared light to X-rays.[90-94] Now, more and more efforts are devoted into the studying of the fundamental physics in these materials such as the spin properties. Magneto-absorption from organo-metal halide perovskites under high magnetic field at low temperature has been discovered in 1990s.[95] However, magnetic field effects from these perovskite materials at room temperature with small magnetic field were discovered recently, proving an easy and useful

method to study the fundamental physics.[96, 97] In conclusion, organo-metal halide perovskites have shown pronounced potentials in electronic applications. More fundamental studies are needed for understating the working principle in perovskites to further improve the efficiencies.

1.6 Outline of the dissertation

Until now, less research on the interaction between intermolecular charge-transfer states have been carried out. It is important that intermolecular charge-transfer sates determine the organic device performance such as photocurrent, photoluminescence, electroluminescence, current and capacitance. Therefore, studying the interactions between intermolecular charge-transfer states becomes necessary and important since it can affect the property of individual intermolecular charge-transfer state. The metal-organic framework molecules have play an important role in application such as spin filter or spin injection for the spintronics. However, the interaction between metal atoms and the organic molecules is lack of studying. Studying the interaction between intramolecular charge-transfer states and d electrons not only provides the interaction mechanism between them, but also suggests new ways for magneto-electric coupling. Due to the development of organic spintronics, the spin injection from ferromagnetic electrode into organic materials needs further study to improve the efficiency. However, the existence of charge-transfer states in the organic space layer ignites the study of interaction between photo-generated charge-transfer states and magnetized charge-transfer states, which on one hand can help improve the spin injection and on the other hand can provide a way for magneto-optical-electrical application.

Based on the research progress in this field, my work in the thesis will focus on the following issues. (1) Examining the interaction between intermolecular charge-transfer states through magneto-photocurrent and magneto-capacitance. (2) Exploring the interaction between intramolecular charge-transfer states and d electrons via magneto-capacitance. (3) Studying the interaction between photo-generated charge-transfer states and magnetized charge-transfer states by magneto-capacitance. (4) Studying the interaction between excitons and free charge carriers in organo-metal halide perovskite. (5) Inspecting

the spin-orbital interaction at the interface between organo-metal halide perovskite and ferromagnetic metal.

This thesis will include eight chapters. Chapter 1 introduces the fundamental knowledge of organic semiconducting materials, organo-metal halide perovskites and the magnetic field effects. Both the excitations and spins in organic semiconducting materials are summarized. Different mechanisms for explaining the magnetic field effects are presented. Chapter 2 covers the materials and the device fabrication techniques used in this thesis. In addition, the setup of magnetic field effects measurements is also introduced. Chapter 3 presents the interaction between intermolecular charge-transfer states in P3HT:$PC_{60}BM$ solar cell studied by magneto-photocurrent. The interaction is changed by the photoexcitation intensities due to the change of distance between intermolecular charge-transfer states. Three possible mechanisms including long-range Coulomb interaction, medium-range spin-orbital coupling and short-range spin interaction are suggested. Chapter 4 reports the interaction between intramolecular charge-transfer states and d electrons in organic-magnetic nanocomposites γ-FeO_x/C_{60}(DPAF>C_9) under photoexcitation. The interaction strength is tuned by the photoexcitation intensities and the distance between intermolecular charge-transfer states and d electrons. Coulomb interaction and spin-orbital coupling is used to explain the phenomenon. Chapter 5 describes the interaction between photo-generated charge-transfer states and magnetized charge-transfer states. Through tuning the photoexcitation intensities and distance between photo-generated charge-transfer states and magnetized charge-transfer states, Coulomb interaction and spin-orbital coupling are demonstrated to explain the interaction. Chapter 6 discusses the interaction between excitons and free charge carriers through tuning the concentration of excitons based on changing injection current, photoexcitation, temperature and interface confinement. Chapter 7 indicates the spin-orbital interaction at the $CH_3NH_3PbI_{3-x}Cl_x$/Co interface. By changing the spins and orbitals at the interface, this interaction is proved from the spin-orbital interaction. Chapter 8 will summarize the whole discussion in this thesis.

CHAPTER 2
DEVICE FABRICATION AND MAGENTIC FIELD EFFECTS MEASUREMENT

In this chapter, we introduce the detail information about device fabrication and the magnetic field effects measurement. The device fabrication procedures are described step by step such as substrate cleaning, organic layer fabrication and metal deposition. Additionally, the measurements and results analysis for magnetic field effects are also presented.

2.1 Device fabrication

The organic semiconducting materials used in this thesis are purchased commercially or synthesized by our cooperators and used as received. All the materials are carefully sealed and storage in a glove box filled with nitrogen gas to prevent the degradation caused by oxidation and humidity. All materials are weighted by a precise balance (Ohas Analytical plus) every time before use. The device fabrication undergoes the standard procedures including substrate cleaning, active layer deposition and metal deposition.

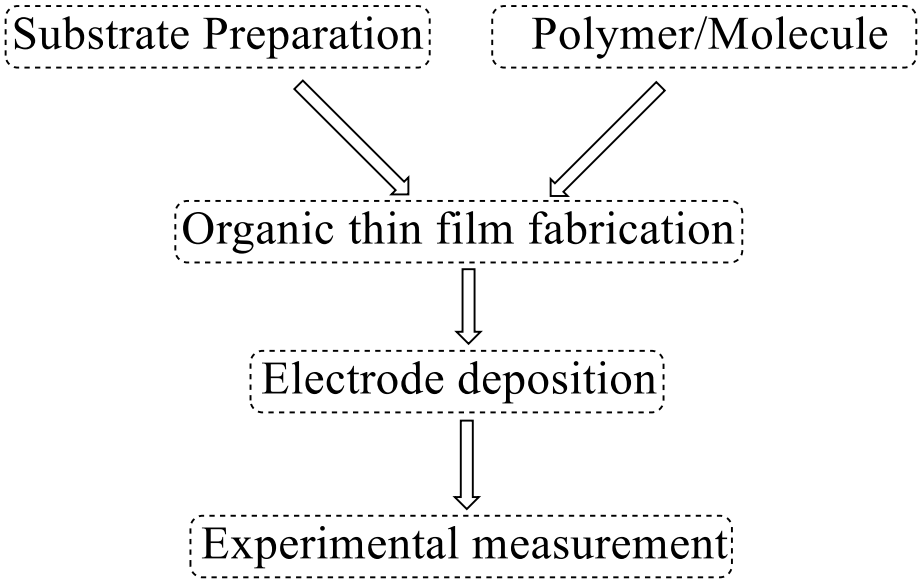

Figure 17 Procedures for device fabrication and characterization**.**

2.1.1 Substrate cleaning

The substrate used in our experiment is customized patterned ITO glass with a dimension of 15mm×15mm. The ITO thin layer has a high quality of 200nm thickness with the average roughness of 2nm, a high optical transmission of 85% and a low electrical square resistance about 15Ω/□. Before fabrication of active layer on the substrates, they are cleaned by detergent for 15 minutes in ultrasonic bath followed by ultrasonic cleaning with deionized water, 2-propanol and acetone for 15 minutes of each step. The solvent-cleaned substrates are dried with a nitrogen gun and subsequently put into a UV-Ozone for surface treatment before using. It is really important of the substrate cleaning for device performance. Otherwise, the device is easy to be short-circuit due to the pinholes formed in the active layer.

2.1.2 Organic layer fabrication

In general, organic thin films can be deposited through spin-casing and thermal deposition. Basically, there are three steps for spin-casting a thin film of polymer: (1) polymers are weighed precisely before use; (2) solutions are made by dissolving the polymers into a chosen solvent; (3) solvent are dropped onto the ITO substrate and spin-casted in a nitrogen filled glovebox. During the spin-casting, the solvent is evaporated and left the polymers to form thin films. The thickness of the polymer layer, which is calibrated by the AFM measurement, can be controlled by the spin-casting speed and solvent concentration.

It is difficult to make a thin film of small molecule directly by spin-casting due to the low viscosity of small molecules. On one hand, we can mix the small molecules into a polymer matrix in solution and then spin-cast to form thin films. On the other hand, thermal evaporation is a convenient and precise way to deposit a thin layer of small molecules. After loading the small molecules in the evaporation and the vacuum of chamber reaching 2×10^{-6} Torr, the current is gradually added to evaporate the small molecule. The evaporation rate and deposition thickness is recorded by a thickness monitor. The shutter is turned on after reaching a steady evaporation speed. When achieving the aimed thickness, the shutter is turned off and the current is shut down.

2.1.3 Metal deposition

In this dissertation, the Co layer and the metal electrode are deposited by thermal evaporation. The process for metal evaporation is similar to that for small molecule evaporation except the different current and temperature. For Co evaporation, we need first melt the Co wire with a higher current and then decrease the current for a steady evaporation rate. In order to make electrodes, the fabricated active layers on substrate are covered by a mask to define the device active area and then transferred into the chamber. After reaching the vacuum level around 2×10^{-6} Torr, electrodes are deposited.

2.2 Magnetic field effects measurements and results analysis

Magnetic field effects from the fabricated devices are carried out for studying the interaction between intermolecular charge-transfer states, interaction between intramolecular charge-transfer states and d electrons, interaction between photo-generated charge-transfer states and magnetized charge-transfer states, interaction between excitons and free charge carriers in organo-metal halide perovskite and magneto-electronic coupling at the interface between organo-metal halide perovskite and ferromagnetic metal. The amplitude and line-shape of the magnetic field effects curves are compared to illustrate these interactions. Furthermore, the results are fitted with Lorenz and Non-Lorenz equations, furthering confirming the interactions.

2.2.1 Magnetic field effects measurement

After fabrication of devices, the basic properties such as absorption, photoluminescence and current-voltage characterization are characterized. For the study of interactions, a specific setup was built-up in our lab for the magnetic field effects measurements as shown in Figure 18. The magnetic field of the electromagnet is driven and controlled by the current from Sorensen DLM80-7.5. The strength is monitored by a Hall gauss meter. The devices are placed between the two poles of the electromagnet for measurement. The current both under photoexcitation and injection are recorded by the Keithley 2400. Therefore, the change of the currents from the device caused by applying magnetic field are detected to produce magneto-photocurrent or magneto-current

respectively. Additionally, the electroluminescence and the photoluminescence are monitored by the spectrometer after transferring through the fiber. The change of them under the external magnetic field are defined as magneto-electroluminescence and magneto-photoluminescence. Moreover, the capacitance under magnetic field are recorded by the impedance spectrometer and then compared with the value without magnetic field to generate magneto-capacitance. Their definitions are shown in the following Equations:

$$MFE_{PC} = \frac{PC_B - PC_0}{PC_0}$$

$$MFE_{PL} = \frac{PL_B - PL_0}{PL_0}$$

$$MFC = \frac{C_B - C_0}{C_0}$$

Where PC, PL and C are photocurrent, photoluminescence and capacitance respectively. B and 0 represents the signals with and without magnetic field.

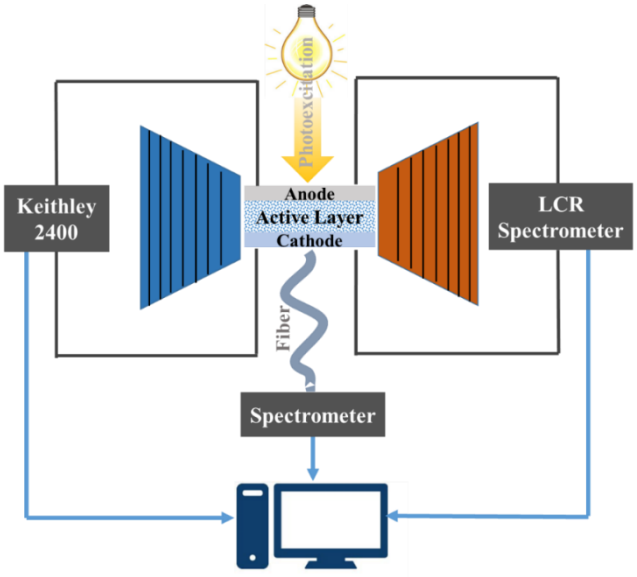

Figure 18 Experiment setup for the magnetic field effects measurements.

2.2.2 Results analysis

It is known that the magnetic field effects can be fitted with Lorenz or Non-Lorenz equations as shown in Figure 19. In the fitting equations, B is the external magnetic field and B_0 is the internal magnetic field of charge-transfer states. The parameter B_0 is related to the exchange interaction and the hyperfine field or the spin orbital coupling in the semiconducting materials. Consequently, fitting the curve with these equations can illustrate the interaction more directly by comparing the change of internal magnetic field B_0。

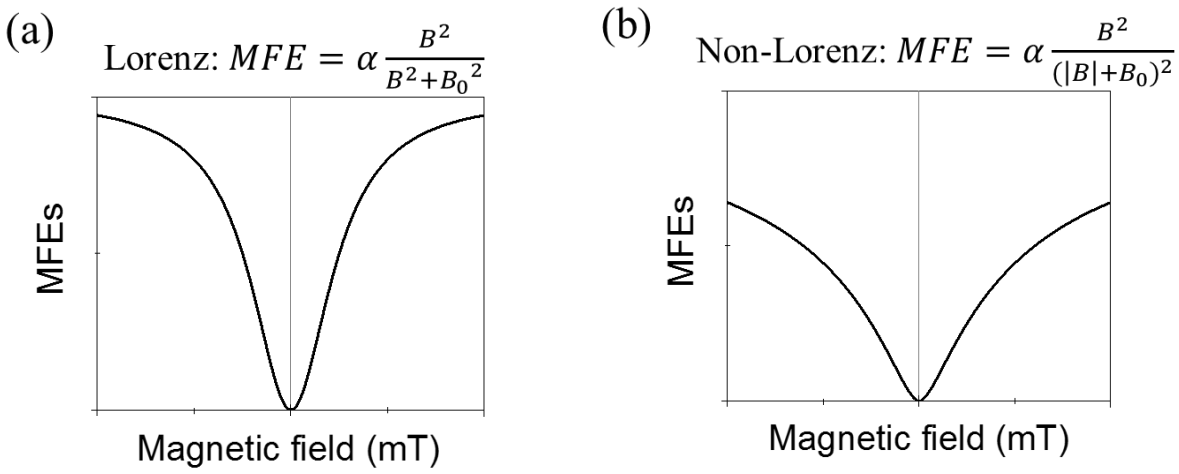

Figure 19 Characterization of Lorenz equation (a) and Non-Lorenz equation (b).

CHAPTER 3

INTERACTION BETWEEN INTERMOLECULAR CHARGE-TRANSFER STATES

We present the interaction between intermolecular charge-transfer states studied by the magneto-photocurrent and magneto-capacitance in this chapter. Increasing the density of intermolecular charge-transfer states leads to an enhancement of interaction between the intermolecular charge-transfer states, reducing the spin-exchange energy between electron and hole in the individual intermolecular charge-transfer state.

3.1 Introduction

Intermolecular charge-transfer (CT) states with singlet and triplet configurations are inevitably formed at the donor: acceptor (D:A) interfaces under photoexcitation. In general, the spin-exchange energy between electron and hole in the intermolecular CT states at D:A interfaces is an important parameter, which can characterize spin-dependent optic, electronic, and magnetic properties.[23, 98-106] Experimental studies have shown that the intermolecular CT states can exhibit magnetic field effects in various functionalities, such as magneto-current, magneto-photocurrent, magneto-photoluminescence, magneto-electroluminescence and magneto-capacitance, with largely tunable properties.[23, 98-104, 107-111] In this chapter we use magneto-photocurrent as a tool to explore the possibilities of optically tunable spin-exchange energy in intermolecular CT states at D:A interfaces. The magneto-photocurrent from intermolecular CT states are essentially generated based on the following two experimental arguments. First, a magnetic field can change the singlet/triplet ratio through perturbing the equilibrium in the singlet-triplet intersystem crossing. This equilibrium is established by the competition between spin mixing and spin conversing based on the internal magnetic interaction and the spin-exchange energy in intermolecular CT states respectively.[98, 112, 113] Second, the singlets and triplets in intermolecular CT states can exhibit high and low dissociation rates due to their different ionic properties.[114, 115] Previous studies have found that intermolecular excited states can conveniently generate magneto-photocurrent due to the fact that a magnetic field can considerably disturb the equilibrium in singlet-triplet transition through spin mixing in organic materials.[108] Now, we use the line-shape characteristics of magneto-photocurrent curves to investigate optically tunable spin-exchange energy at the D:A interfaces. The line-shape in magnetic field effects has been studied to discuss the positive and negative effects by

considering the polaron pairs and bipolarons.[23, 116] In order to explicitly understand the effect of spin-exchange energy, we consider that the line-shape is essentially determined by the changing rate of singlet/triplet ratio, namely $\frac{\partial\left(\frac{S}{T}\right)}{\partial B}$, when the equilibrium in singlet-triplet transition in intermolecular CT states at D:A interfaces is disturbed by the external magnetic field. In general, perturbing the equilibrium in singlet-triplet ratio can lead to magnetic field effects (MFE) at hyperfine and spin-exchange regimes occurring at low (< 10 mT) and high (> 10 mT) magnetic fields respectively in organic materials.[12, 117, 118], Therefore, a magnetic field effect can consist of hyperfine and spin-exchange components, as shown in Eq. (1).

$$\mathrm{MFE} = \mathrm{MFE}_{\mathrm{hyperfine}} + \mathrm{MFE}_{\mathrm{spin-exchange}} \quad (1)$$

In particular regime, the competition between magnetic field and spin-exchange energy at the high-field can determine the changing rate of singlet/triplet ratio in intermolecular CT states and consequently controls the line-shape characteristics in magneto-photocurrent in this study. Therefore, investigating the line-shape characteristics of magnetic field effects in spin-exchange regime can advance the understanding on the critical parameters controlling the spin-exchange energy in organic semiconducting materials. Experimental results indicate that the spin-exchange energy in intermolecular CT states at D:A interfaces can be optically changed by using different photoexcitation intensities through the interactions between intermolecular CT states.

3.2 Experimental

Photo-induced charge-transfer states are generated in a bulk heterojunction organic solar cell constructed by organic semiconducting materials P3HT and PCBM (Figure 20 (a) and (b)) as donor and acceptor respectively. The bulk heterojunction thin films were spin-casted on precleaned indium tin oxide (ITO) conducting glass substrates coated with poly(3,4-ethylenedioxythiophene) poly(styrenesulfonate) (PEDOT-PSS), from chloroform solutions of P3HT:PCBM composites with a calculated weight ratio in a nitrogen atmosphere. The cathode Ca/Al were thermally deposited onto the bulk-heterojunction thin

films continuously under a vacuum of $2x10^{-6}$ Torr. The solar cells were thermally annealed at 150 ^{o}C for 10 min in a nitrogen atmosphere to optimize the device performance.

3.3 Results and Discussions

3.3.1 Generation of intermolecular charge-transfer states

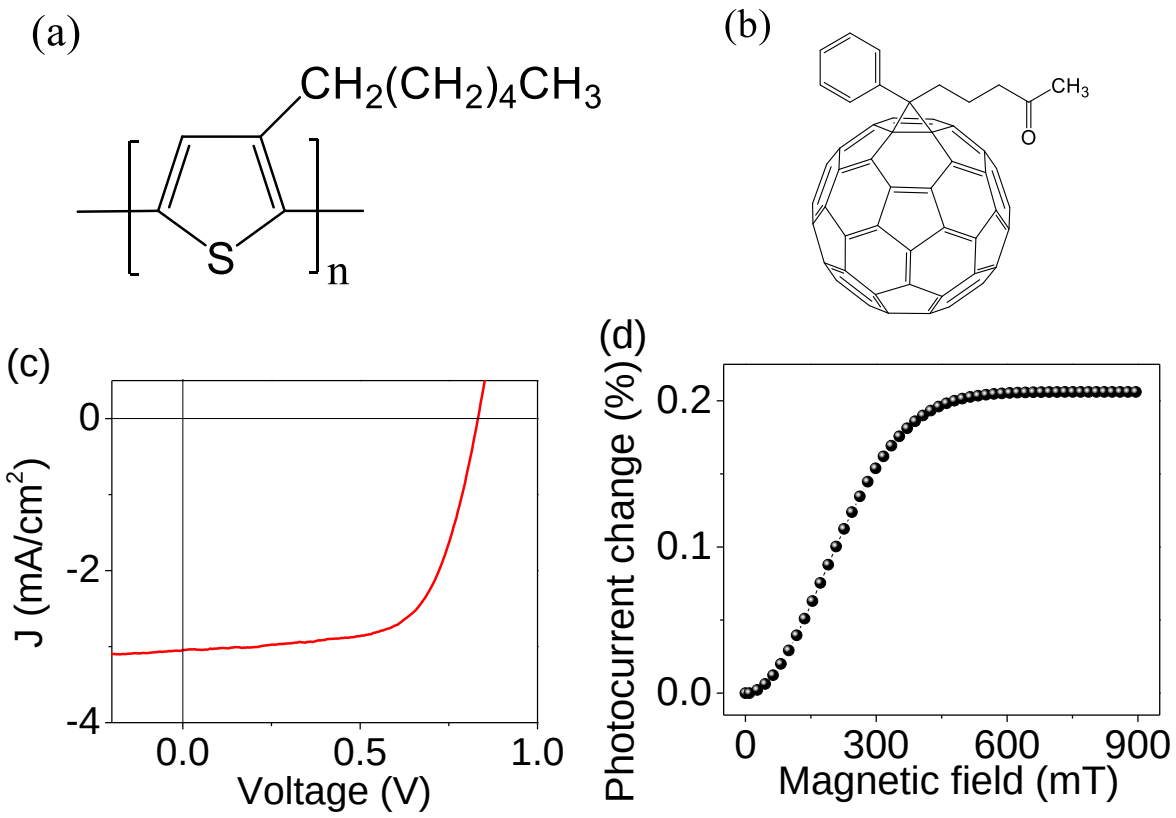

Figure 20 Chemical structure of (a) P3HT and (b)PCBM. (c) IV characterization of the P3HT:PCBM solar cell. (d) Magneto-photocurrent from intermolecular charge-transfer states.

The solar cells based on the P3HT:PCBM heterojunction structure give a short-circuit current density (J_{sc}) of 3.04 mA/cm^2, an open-circuit voltage (V_{oc}) of 0.83 V and a fill factor (FF) of 0.65, leading to a PCE of 1.66% under the 532 nm CW laser photoexcitation (Figure 20 (c)). Generally, the photocurrent is from the dissociation of

intermolecular CT states generated by the photoexcitation. Therefore, the IV characterization illustrates the formation and dissociation of intermolecular CT states at P3HT:PCBM interface. Further study of magneto-photocurrent is carried out to illustrate the existence of intermolecular CT states. Figure 20 (d) shows that magneto-photocurrent amplitude increases quickly from 0 mT to 500 mT, reaching a value around 0.2%. The external magnetic field can compete with the spin-exchange energy of intermolecular CT states to change the singlet/triplet ratio, resulting in a magneto-photocurrent.[108, 112, 113, 115, 119, 120] Our previous studies show that positive magneto-photocurrent dominantly originates from the intermolecular CT states at the D:A interfaces.[108] Recent results also provide an evidence that the observed magneto-current comes from the intermolecular CT states at the D:A interfaces.[121] Consequently, the positive magneto-photocurrent further indicates the formation of intermolecular CT states.

3.3.2 Interaction between intermolecular charge-transfer states

Figure 21 (a) depicts two important differences between magneto-photocurrent under different photoexcitation intensities. First, increasing photoexcitation intensity generates a narrower line shape of magneto-photocurrent curve. The full width at half maximum (FWHM) of decreases from 720 mT to 460 mT when the photoexcitation intensity increases from 9 mW/cm^2 to 24 mW/cm^2 as described by the normalized magneto-photocurrent curves in Figure 21 (b). Second, increasing the photoexcitation intensity improves the magnitude of magneto-photocurrent from 0.1% to 0.2%. Former studies have shown that positive magneto-photocurrent dominantly originates from the intermolecular CT states at the D:A interfaces.[108, 122] Recent published results also provide an evidence that the magneto-current originates from the intermolecular CT states at the D:A interfaces in D:A system.[104] Therefore, the positive magneto-photocurrent can reflect the properties of the intermolecular CT states in this study. In intermolecular CT states, the spin-exchange energy and internal magnetic interaction disallows and allows the singlet-triplet intersystem crossing respectively, resulting in a certain singlet/triplet ratio with a dynamic equilibrium established in the singlet-triplet intersystem crossing. The spin-orbital interaction is weak in organic materials such as P3HT and PCBM with aromatic structures

due to the lack of heavy elements. Therefore, the hyperfine interaction dominates the internal magnetic interaction for spin mixing. However, the hyperfine interaction in organic materials is normally small (< 10 mT).[117, 123] Together with the fact that the magneto-photocurrent studied here is in the field range above hyperfine interaction (> 10 mT), the magneto-photocurrent is essentially controlled by the competition between spin-exchange energy and external magnetic field that are responsible for spin-conversing process and spin-mixing process, respectively. Consequently, the spin-exchange energy plays a key role in determining the line-shape of magneto-photocurrent. The line-shape of magneto-photocurrent essentially describes how fast the singlet/triplet ratio changes with an external magnetic field when it perturbs the intersystem crossing within individual intermolecular CT states. The narrower and broader line-shape at higher and lower photoexcitation intensities indicates a faster and slower changing rate of singlet/triplet ratio, corresponding to a smaller and lager spin-exchange energy. Therefore, the line-shape characteristics of magneto-photocurrent illustrates that the spin-exchange energy can be manipulated through the interactions between intermolecular CT states.

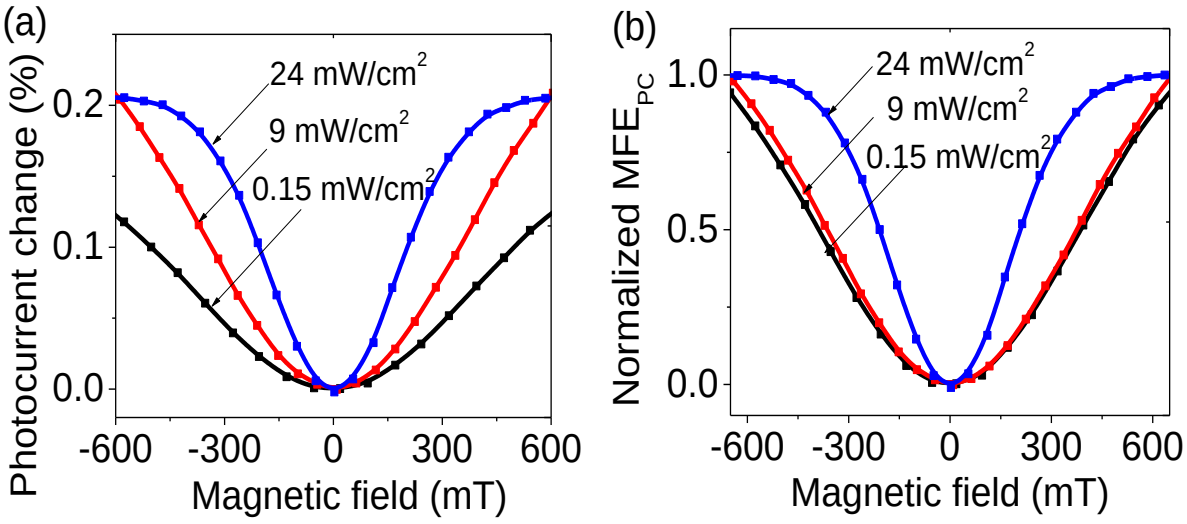

Figure 21 (a) Magneto-photocurrent from the P3HT:PCBM solar cell with 20 wt% PCBM under different photoexcitation. (b) Normalized magneto-photocurrent curves under different photoexcitation intensities.

Now we use the magnitude of magneto-photocurrent to predict the effect of photoexcitation intensity on the density of CT states. Generally, photocurrent in the D:A composite derives from the dissociation of excitons and intermolecular CT states, describing as $I_{ph} = I_{exciton} + I_{CT}$. The exciton-based and intermolecular CT states-based photocurrents are insensitive and sensitive to external magnetic field due to the large and small spin-exchange energies, respectively. Based on the definition of magneto-photocurrent given by equation (2):

$$MFE = \frac{I_{ph(B)} - I_{ph(0)}}{I_{ph(0)}} \quad (2)$$

where $I_{ph(B)}$ and $I_{ph(0)}$ are photocurrents with and without an external magnetic field. The magnitude of magneto-photocurrent can be described by:

$$MFE_{PC} = \frac{I_{CT(B)} - I_{CT(0)}}{I_{exciton} + I_{CT(0)}} \quad (3)$$

where $I_{CT(B)}$, and $I_{CT(0)}$ are photocurrents from CT states with and without external magnetic field. $I_{exciton}$ is the photocurrent from excitons. Eq. (3) indicates that the photocurrent generated from the dissociation of CT states is responsible for the magneto-photocurrent. Furthermore, the photocurrent from intermolecular CT states can be approximately expressed as $I_{CT} = \alpha D_{CT}$, where α is the dissociation rate, and D_{CT} is the density of charge-transfer states at D:A interfaces. Therefore, the magnitude of MFE_{PC} can be written as:

$$MFE_{PC} = \frac{\alpha D_{CT(B)} - \alpha D_{CT(0)}}{I_{exciton(0)} + \alpha D_{CT(0)}} \quad (4)$$

where the $D_{CT(B)}$ and $D_{CT(0)}$ are the densities of intermolecular CT states with and without magnetic field. According to the Eq. (4), a larger signal amplitude in the magneto-photocurrent corresponds to a higher density of CT states. At D:A interface the intermolecular CT states can interact with each other to affect the spin-exchange energy in individual intermolecular CT states. This can modify the changing rate of singlet/triplet ratio which leads to a change on the line-shape in magneto-photocurrent. Consequently,

under a higher photoexcitation, more intermolecular CT states are formed with stronger mutual interactions which are responsible for a faster rate of changing singlet/triplet ratio indicated by the narrower magneto-photocurrent curve.

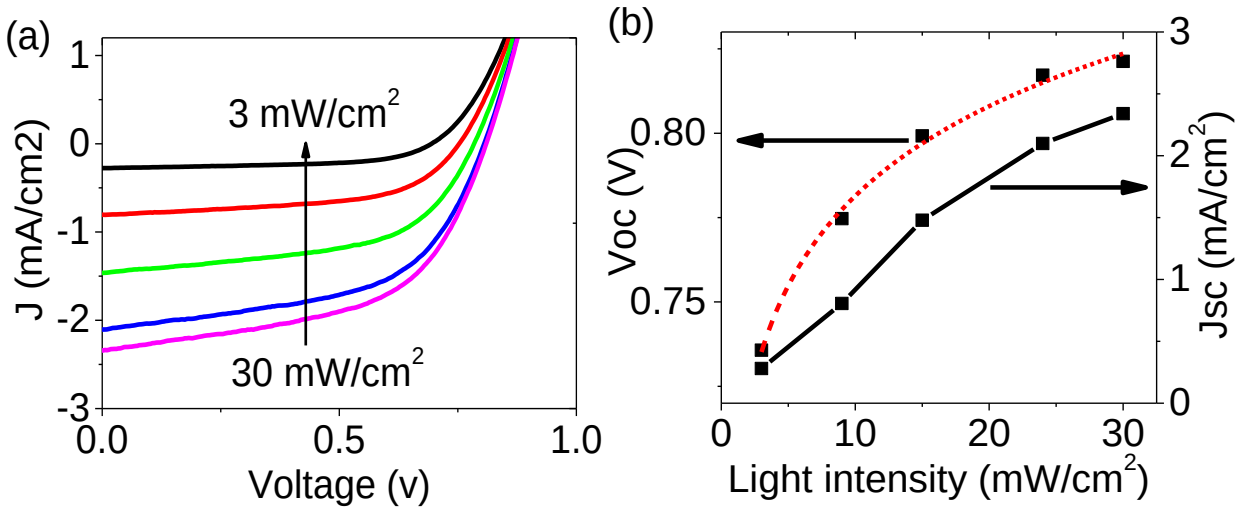

Figure 22 (a) Current-Voltage curves under photoexcitation intensities. (b) Open-circuit voltage and short-circuit current as a function of photoexcitation intensity. Red dotted line is the fitting curve by using the Eq. 5.

The higher density of intermolecular CT states induced by a higher photoexcitation at the D:A interface is further confirmed by analyzing V_{oc} and J_{sc} under different light intensities. Experimental studies have shown that increasing photoexcitation can introduce a nonlinear increase on V_{oc} and J_{sc} by increasing the density of intermolecular CT states at the D:A interface. The V_{oc} increases from 0.69 V to 0.81 V when photoexcitation intensity changes from 3 mW/cm^2 to 30 mW/cm^2. At the same time, J_{sc} increases from 0.28 mA/cm^2 to 2.36 mW/cm^2 (Figure 22 (a)). The nonlinearly increased V_{oc} with a light intensity can be fitted by Eq. (5):[124]

$$V_{OC} = \frac{E_{gap}}{e} - n\frac{kT}{e}\ln\left(\frac{(1-\alpha)\gamma {N_C}^2}{\alpha G}\right) \qquad (5)$$

where E_{gap} is the energy difference between PCBM's LUMO and P3HT's HOMO, α is the dissociation probability of a bound electron-hole pair into free charge carriers, γ is the

Langevin recombination constant, and G is the generation rate of intermolecular CT states at the D:A interface. Since α and γ do not depend on the light intensity while G is light intensity dependent, the fitted V_{oc} curve (Figure 22 (b)) illustrates that a higher photoexcitation produces more intermolecular CT states through the increasing G factor. The increasing intermolecular CT states production rate G with higher photoexcitation can be further explained by photoexcitation-enhanced photocurrent. The increasing intermolecular CT states production rate G introduces more intermolecular CT states under a higher photoexcitation to dissociate into free charges, increasing the short-circuit current. Therefore, the increase of V_{oc} and J_{sc} with light intensity further indicates that more intermolecular CT states are produced at the D:A interface under a higher photoexcitation.

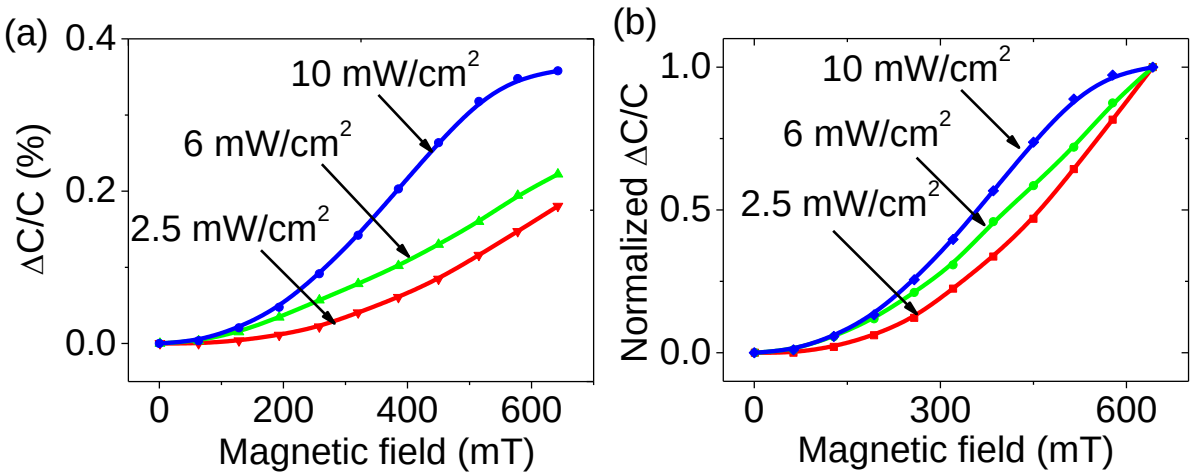

Figure 23 (a) Magneto-capacitance from intermolecular CT states under different photoexcitation intensities. (b) Normalized magneto-capacitance curves.

The tunable spin-exchange energy in intermolecular CT states caused by interaction between intermolecular CT states is further demonstrated by analyzing the photo-induced magneto-capacitance from the ITO/PEDOT:PSS/P3HT:PCBM/Ca/Al device operating in a capacitance mode under an alternating bias of 50 mV at 1 kHz. It is known that the magneto-capacitance from organic semiconducting materials is established upon two basic experiment arguments: (1) the singlet/triplet ratio of intermolecular CT states is disturbed by the external magnetic field through perturbing the intersystem crossing; (2) the singlets

and triplets have strong and weak electrical polarizations due to their differently spin-configuration modulated wavefunctions. Generally, magneto-capacitance has two channels from intermolecular CT states: polarization-based magneto-capacitance and transport-based magneto-capacitance.[125-128] However, our studies show that polarization-based magneto-capacitance dominates in the situation of intermolecular CT states.[111, 118] As a result, the changing rate of singlet/triplet ratio $\frac{\partial\left(\frac{S}{T}\right)}{\partial B}$ can be also used to explain the magneto-capacitance line-shape. Here, the capacitance is developed by the polarizations from both the exciton ($P_{exciton}$) and intermolecular CT states (P_{CT}) which are magnetic field-independent and magnetic field-dependent respectively. Based on these conditions, the magnitude of magneto-capacitance can be expressed as

$$\mathrm{MFC} = \frac{P_{CT(B)} - P_{CT(0)}}{P_{exciton(0)} + P_{CT(0)}} \qquad (6)$$

where $P_{CT(B)}$ and $P_{CT(0)}$ are the polarizations of intermolecular CT states with and without an external magnetic field, $P_{exciton(0)}$ is the polarization of excitons. Meanwhile, the polarization of intermolecular CT states is proportional to the density of intermolecular CT states. With photoexcitation intensity increasing from 2.5 mW/cm^2 to 10 mW/cm^2, the magneto-capacitance magnitude increases from 0.16% to 0.36% at 600 mT (Figure 23 (a)), indicating an increase in the density of intermolecular CT states. It is further noticed that the line-shape of magneto-capacitance curve turns to be narrower under a higher photoexcitation (Figure. 23 (b)) in high magnetic field region. The narrower curve shape of magneto-capacitance corresponds to the faster changing rate of singlet/triplet ratio $\frac{\partial\left(\frac{S}{T}\right)}{\partial B}$ in intermolecular CT states. This means that the spin-exchange energy is decreased upon increasing the density of intermolecular CT states, confirming that changing the density of intermolecular CT states can modify the spin-exchange energy in intermolecular CT states.

3.3.3 Discussion

This optically tunable spin-exchange energy is suggested to relate to the interactions between intermolecular CT states. There are three possible mechanisms accountable for

the interactions between intermolecular CT states to explain the line-shape change. Firstly, long-range Coulomb interaction can exist between intermolecular CT states due to the electrical dipole-dipole coupling.[12, 118] The long-range Coulomb interaction has two effects: (i) weakening the electron-hole Coulomb attraction within individual CT states due to the dipole field redistribution and (ii) increasing the electron-hole separation distance due to Coulomb shielding effect. These two outcomes can elongate the distance between electron and hole in a single CT state and lead to a decrease in the spin-exchange energy which results in a line-shape narrowing in magneto-photocurrent and magneto-capacitance. Secondly, mid-range spin-orbital interaction can occur when an electron spin of one intermolecular CT state interacts with the orbital field of the neighbor intermolecular CT state. The interaction can essentially enhance the effective spin-orbital coupling in each intermolecular CT state and results in a broadening magneto-photocurrent and magneto-capacitance line-shape. Thirdly, short-range spin interaction can exist between two adjacent intermolecular CT states with different spin configurations. Due to the spin dipole field redistribution, the spin interaction between intermolecular CT states can weaken the spin contribution to the spin-orbital coupling and spin-exchange energy intermolecular CT states and causes a narrower line-shape in the magneto-photocurrent and magneto-capacitance. Spin interaction have been demonstrated between spin radicals and intermolecular CT states which enhances the photovoltaic function and magneto-capacitance.[129, 130] Here, we suggest that the long-range Coulomb interaction between intermolecular CT states functions as an effective mechanism to change the spin-exchange energy in intermolecular CT states upon increasing the photoexcitation intensity. Figure 24 (a) schematically depicts that under a lower photoexcitation intensity, the Coulomb interaction between intermolecular CT states becomes weak, leading to a larger spin-exchange energy. On the contrary, a higher photoexcitation intensity generates more intermolecular CT states at the D:A interfaces with a stronger Coulomb interaction, yielding a smaller spin-exchange energy. Figure 24 (b) summarizes the effect of interaction between intermolecular CT states on the curve shape in magnetic field effects through changing the spin-exchange energy in CT states. In an intermolecular CT state, the internal magnetic field energy and spin-exchange energy compete with each other to establish an

equilibrium with a certain singlet/triplet ratio through intersystem crossing. Above the hyperfine field, when an external magnetic field can compete with the spin-exchange energy, the intersystem crossing can be perturbed to change the singlet/triplet ratio. The changing rate of singlet/triplet ratio $\frac{\partial\left(\frac{S}{T}\right)}{\partial B}$ is reflected by the line-shape in magnetic field effects. Under a higher photoexcitation intensity, more intermolecular CT states interact with each other Coulombically, reducing the spin exchange energy. This can lead to a faster changing rate of singlet/triplet ratio $\frac{\partial\left(\frac{S}{T}\right)}{\partial B}$ with a narrower line-shape in magnetic field effects.

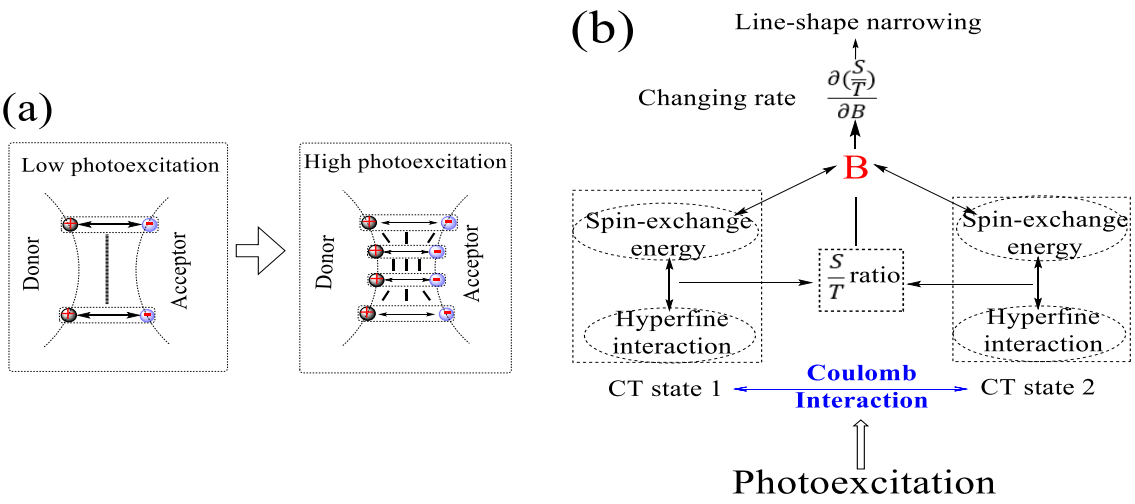

Figure 24 (a) Diagram to show the intensity of intermolecular CT states under low and high photoexcitation intensities. (b) Schematic illustration of the effects of photoexcitation intensity on spin-exchange energy.

3.4 Conclusion

In summary, changing photoexcitation intensity can change the spin-exchange energy in intermolecular CT states through the interactions between different intermolecular CT states by studying the line-shape and magnitude of both magneto-photocurrent and magneto-capacitance in organic bulk heterojunction (P3HT:PCBM) solar

cells. The line-shape narrowing with increasing photoexcitation intensity reflects an optically tunable spin-exchange energy in intermolecular CT states. Our analysis indicates that the long-range Coulomb interaction between intermolecular CT states can decrease the spin-exchange energy at the D:A interface upon changing photoexcitation intensity. As a result, our work presents a convenient approach to optically change the spin-exchange energy at organic D:A interfaces by using intermolecular CT states.

CHAPTER 4

INTERACTION BETWEEN INTRAMOLECULAR CHARGE-TRANSFER STATES AND D ELECTRONS

This article reports the interaction between intramolecular charge-transfer states and d electrons based on magneto-capacitance studies by using organic-magnetic nanocomposites γ-FeO_x-C_{60}(>DPAF-C_9). We observe that the intramolecular charge-transfer states and magnetic d electrons exhibit stronger coupling in excited state than that in ground state. By changing the densities of electric polarization and spin polarization, we show that this coupling originates from the Coulomb interaction and spin-spin interaction.

4.1 Introduction

Delocalized π electrons have shown fascinating semiconducting properties in organic material and significant responses to external electrical and optical excitations.[131-133] However, semiconducting π electrons lack magnetic properties due to their weak spin interactions.[123, 134] The d electrons, on the other hand, have shown tremendous magnetic properties due to their spin interactions, though they often lack semiconducting functions.[135, 136] Therefore, combining semiconducting π electrons and magnetic d electrons can generate electric-magnetic coupling to create magneto-electronic and magneto-optic actions through materials processing. Studies have indicated materials mixing as an effective way to combine different functional materials.[137, 138] Here, we incorporate organic semiconducting materials with surface-modified solvent-soluble magnetic nanoparticles to synthesize nanocomposites for studying the interaction between the intramolecular charge-transfer states and magnetic d electrons.

Experimental studies have shown that charge-transfer states in organic semiconducting materials can generate magneto-capacitance phenomena in semiconducting π electron systems.[130, 139, 140] This can be attributed to (i) the magnetic field-dependent singlet/triplet branching ratio in charge transfer states and (ii) the singlet and triplet charge-transfer states have different electric polarizations.[99, 110-112, 115, 118, 122, 141-143] In addition, ferromagnetic materials can demonstrate magneto-capacitance due to the coupling between the electronic polarization and the magnetic polarization in d electron systems.[103, 107, 126, 144] Therefore, combining charge-transfer states in semiconducting π electron systems with magnetic dipoles in d electrons systems provides an opportunity to

investigate the π-d coupling in excited state by using magneto-capacitance studies based on organic-magnetic γ-FeO_x-C_{60}(>DPAF-C_9) nanoparticles.

In this study, intramolecular charge-transfer states function as electrical dipoles in π electron systems that have tunable moments under photoexcitation; applying photoexcitation can thereby greatly change the density of the electrical dipoles.[145] Surface modified solvent-soluble magnetic particles, when combined with these π electron systems, provide magnetic d electron systems ready to couple with the electrical dipoles from the intramolecular charge-transfer states. Combining intramolecular charge-transfer states and surface modified magnetic nanoparticles presents a unique way of exploring π-d electron coupling in excited state under photoexcitation. In this study we use magneto-capacitance measurements to explore π-d electron coupling in excited state. Our magneto-capacitance measurements show that combining intramolecular charge-transfer states with surface modified solvent-soluble magnetic nanoparticles leads to a π-d electron coupling that is much stronger in excited state than in ground state. Our analysis indicates that the π-d electron coupling results from the Coulomb interaction and the spin-spin interaction.

4.2 Experiments

The organic-magnetic γ-FeO_x-C_{60}(>DPAF-C_9) nanocomposites as shown in Figure 25 are designed by combining the charge-polarizable fullerenyl chromophore C_{60}(>DPAF-C_9), in a form of nanocomposite with magnetic γ-FeO_x, as a well-defined, covalently periconjugated acceptor-donor nanostructure.[146] The fullerenyl chromophore C_{60}(>DPAF-C_9) was made by combining a highly photoresponsive dialkyldiphenylaminofluorene (DPAF-C_n) donor-chromophore subunit, used as an antenna for absorbing electro-magnetic wave in the visible range, with the electron-accepting C_{60} cage.. In the excited state, this combination facilitates the facile intramolecular electron transfer from the DPAF-C_n moiety to the moiety of the C_{60}. The C_{60}(>DPAF-C_9) is also coupled with a cyclopropanyl keto-linker to enable the keto-enol isomerization mechanism within the material to increase the rate of electron transfer from the donor to the acceptor subunits. The magnetic nanoparticle γ-FeO_x, which provides d electrons, was created by binding n-octylamine to the surface of iron oxide nanoparticles. The d electrons in γ-FeO_x

interact with the π electrons in C_{60}(>DPAF-C_9) by coupling in the organic-magnetic γ-FeO_x-C_{60}(>DPAF-C_9) nanocomposites.

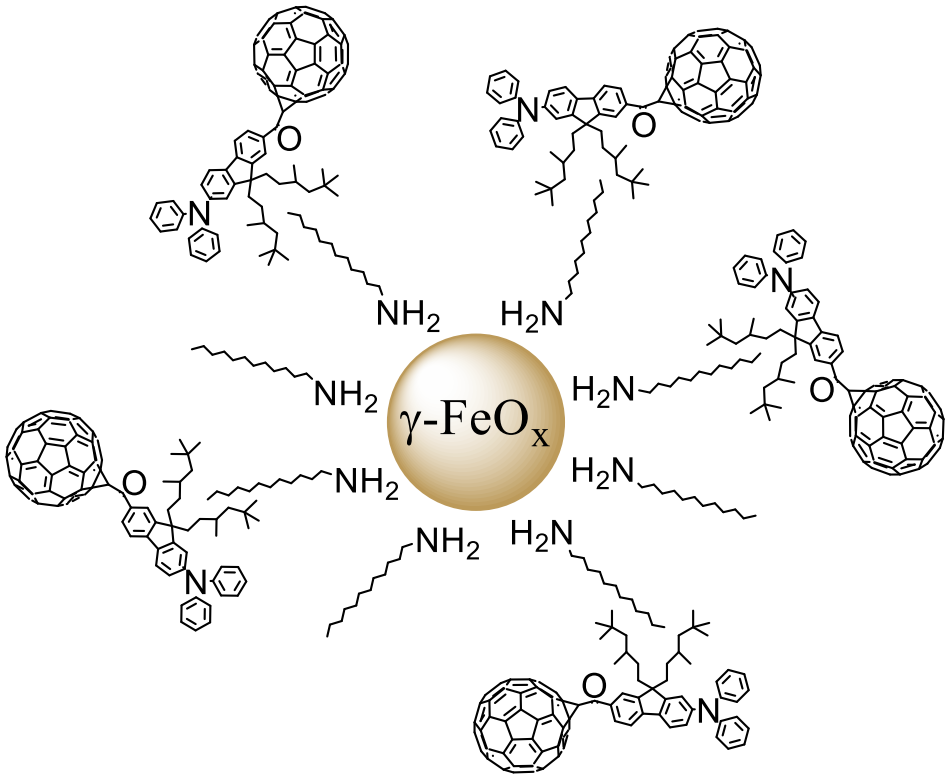

Figure 25 Chemical structure of organic-magnetic γ-FeO_x-C_{60}(>DPAF-C_9) nanocomposite.

The thin-film devices were fabricated with a sandwiched architecture of ITO/active layer/Al. The active layers were spin cast on pre-cleaned ITO substrates with a thickness of 50 nm from the chloroform solution containing the PMMA and γ-FeO_x, C_{60}(>DPAF-C_9) and γ-FeO_x-C_{60}(>DPAF-C_9) in a weight ratio of 8:4. Aluminum (Al) electrodes were thermally deposited under the vacuum of 8×10^{-7} torr with the thickness of 80 nm. The magneto-capacitance measurements were performed on the fabricated devices located in a magnetic field by using an Agilent E4980A LCR meter with zero DC bias and 50 mV AC field at 1 kHz. The magneto-current measurements were performed on the fabricated devices located in a magnetic field by using Keithley 2400. The 405 nm solid state laser was used as photoexcitation to generate intramolecular excited state of C_{60}(>DPAF-C_9).

The magneto-capacitance was defined as $MFC = \frac{C_B - C_0}{C_0}$, the C_B and C_0 are the capacitances with and without magnetic field, respectively. The magneto-current was defined as $MC = \frac{I_B - I_0}{I_0}$, the I_B and I_0 are the currents with and without magnetic field, respectively. All the measurements are done under nitrogen atmosphere at room temperature.

4.3 Results and discussion

4.3.1 Ground state-based π-d electron coupling

Figure 26 (a) describes the magneto-capacitance phenomena produced by C_{60}(>DPAF-C_9), γ-FeO_x, and γ-FeO_x-C_{60}(>DPAF-C_9) in ground states. Clearly, C_{60}(>DPAF-C_9) shows negligible magneto-capacitance while γ-FeO_x exhibits clear magneto-capacitance. More importantly, γ-FeO_x-C_{60}(>DPAF-C_9) shows even larger magneto-capacitance than γ-FeOx. The positive magneto-capacitance from γ-FeO_x clearly demonstrates the coupling between spin and electric polarizations of d electrons in γ-FeO_x particles. It indicates that the spin polarization of γ-FeO_x can be changed by an external magnetic field, thereby changing electric polarization as well to produce the magneto-capacitance signal. Previous studies have shown that charge-transfer states can be formed in ground state at the interface between donor and acceptor based on charge transfer through Van der Walls-type bonding and electron tunneling.[147-149] This means that the π-d electron coupling in ground state can theoretically occur in the γ-FeO_x-C_{60}(>DPAF-C_9) composite. Our magneto-capacitance measurements demonstrate the existence of this coupling experimentally. The increased magneto-capacitance of γ-FeO_x-C_{60}(>DPAF-C_9) shown in Figure 26 (a) demonstrates plainly that the π-electron in C_{60}(>DPAF-C_9) couples with the d-electron in γ-FeO_x. The coupling is further confirmed by the line-shape of the magneto-capacitance from γ-FeO_x-C_{60}(>DPAF-C_9), which is narrower than that from the γ-FeO_x, as shown in Figure 26 (b).

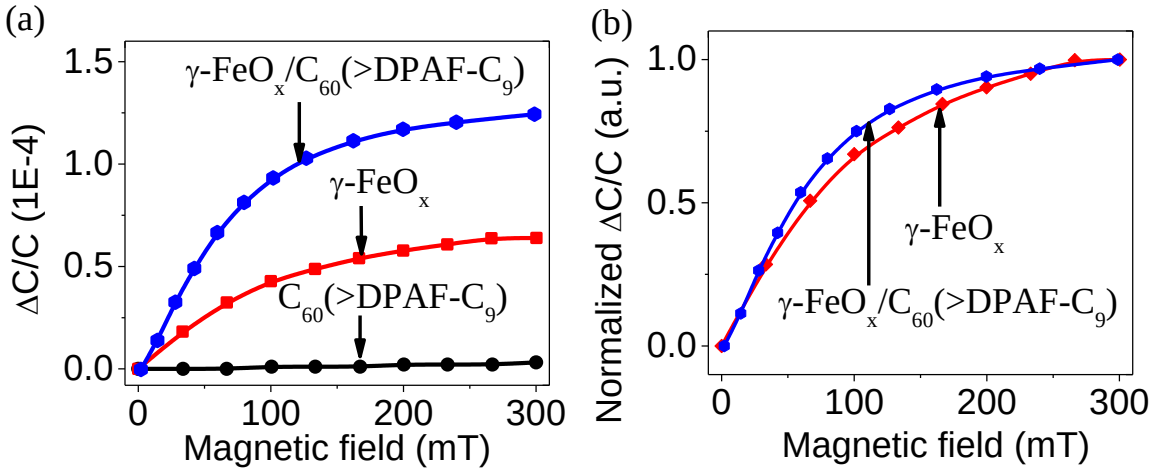

Figure 26 (a) Magneto-capacitance from γ-FeO_x-C_{60}(>DPAF-C_9), γ-FeO_x and C_{60}(>DPAF-C_9) in ground state; (b) Normalized magneto-capacitance in ground state.

4.3.2 Excited state-based π-d electron coupling

Now we show the π-d electron coupling is enhanced in excited state by measuring magneto-capacitance under photoexcitation. Figure 27 (a) describes the magneto-capacitance phenomenon from the γ-FeO_x-C_{60}(>DPAF-C_9) composite in both ground and excited state. It is interesting that the magneto-capacitance signal from the γ-FeO_x-C_{60}(>DPAF-C_9) composite in excited state can be divided into two components with different slopes. The first component with smaller slope shows a slow increase below 20 mT while the second component with larger slope exhibits a fast increase above 20 mT. The phenomenon of two components in the magneto-capacitance of γ-FeO_x-C_{60}(>DPAF-C_9) suggests that π-d electron coupling is stronger when the nanocomposite is in the excited state. It is also clear that applying photoexcitation dramatically increases the amplitude of the magneto-capacitance signal as comparing to the ground state. The magneto-capacitance of C_{60}(>DPAF-C_9) in both ground state and excited state shown in Figure 27 (b) illustrates distinctly that the photo-induced magneto-capacitance of C_{60}(>DPAF-C_9) contributes to the increase of the magneto-capacitance of the nanocomposites γ-FeO_x-C_{60}(>DPAF-C_9). However, the magneto-capacitance of the nanocomposites γ-FeO_x-C_{60}(>DPAF-C_9) shows

a much greater value (6.0E-4) than the C_{60}(>DPAF-C_9) (2.28E-6) under photoexcitation, confirming that the π-d electron coupling is stronger in excited state.

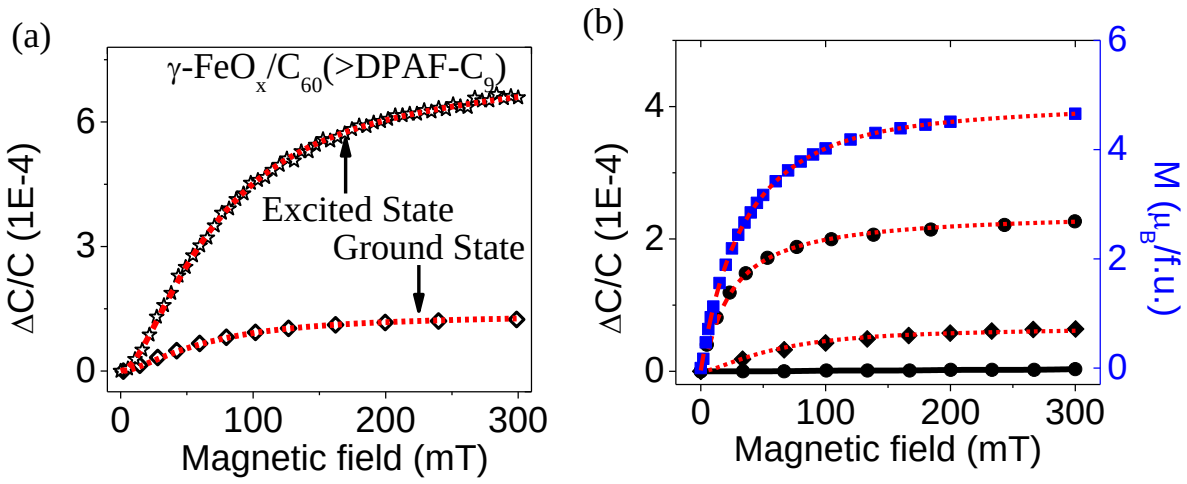

Figure 27 (a) Magneto-capacitance of γ-FeO_x-C_{60}(>DPAF-C_9) in ground state and excited state; (b) Left axis: magneto-capacitance of C_{60}(>DPAF-C_9) in ground state and excited state (black dot) and magneto-capacitance of γ-FeO_x (black diamond). Right axis: M-H curve of γ-FeO_x at room temperature. Red dotted lines are the fitting curves.

4.3.3 Confirmation of polarization-based magneto-capacitance

It is known that a magneto-current can exist during the magneto-capacitance measurement, which can also be shown as a magneto-capacitance phenomenon in capacitance measurements.[127, 128] Therefore, a magneto-capacitance phenomenon can be generated in two different ways: polarization-based magneto-capacitance and transport-based magneto-capacitance developed from magneto-polarization and magneto-current respectively.[111, 118, 127, 128] The polarization-based magneto-capacitance is essentially developed by the different electrical polarizations from singlet and triplet charge-transfer states.[142, 143] The argument that singlets and triplets have stronger and weaker electrical polarizations is supported theoretically by their higher and lower ionic properties originating from spin configuration-modulated orbital wavefunctions.[150] It is also supported by the experimental result that singlets and triplets have higher and lower

dissociation rates, shown in photocurrent studies in organic solar cells.[108, 114, 151] The transport-based magneto-capacitance comes from the experimental phenomenon that the singlet and triplet charge-transfer states generate higher and lower electrical conductivities though charge dissociation, which is a primary mechanism for realizing magneto-current in organic semiconducting materials.[20, 23, 102-104] We find that the transport-based magneto-capacitance contributes negligibly to the magneto-capacitance measurements under photoexcitation.[118] This is the case because the magneto-current has no detectable response to capacitance measurements at AC frequencies.

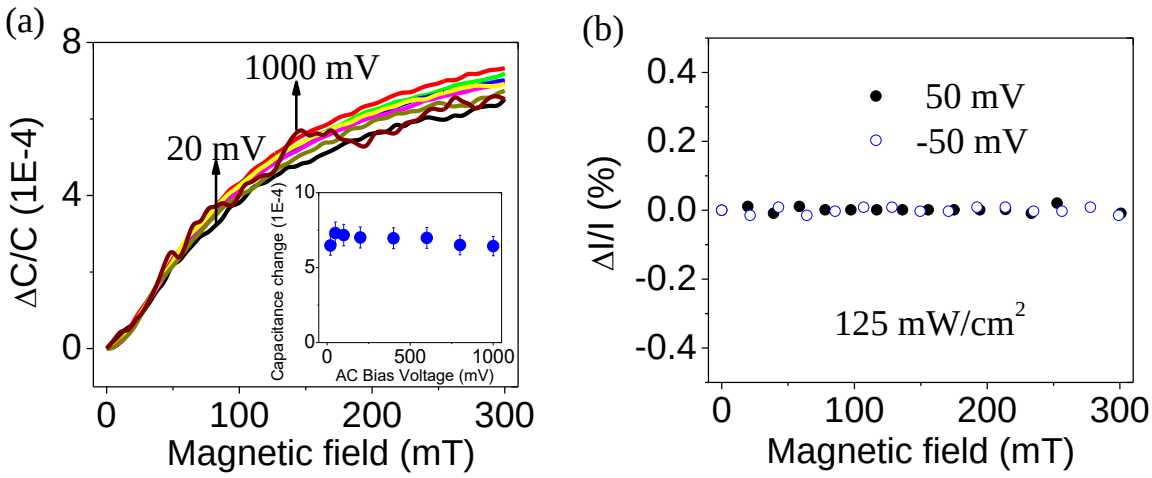

Figure 28 (a) Magneto-capacitance of ITO/γ-FeO_x-C_{60}(>DPAF-C_9):PMMA/Al with 250mW/cm^2 phtoexcitation under different AC bias, inset showing the magneto-capacitance value at 300 mT under different AC bias voltage; (b) Current change of device ITO/γ-FeO_x-C_{60}(>DPAF-C_9):PMMA/Al with 125 mW/cm^2 in magnetic field. The +50 mV and -50 mV is the magnitude of AC bias during the magneto-capacitance measurement.

The following two measurements are used to confirm that the magneto-capacitance observed in this study is from magneto-polarization instead of magneto-current. First, the magneto-capacitances shown in Figure 28 (a) are almost unchanged after the AC bias is increased from 20 mV to 1000 mV, suggesting that the observed magneto-capacitance arises predominantly from magneto-polarization rather than magneto-current. Second, Figure 28 (b) indicates a negligible change in magneto-current between +50 mV and -50

mV bias with photoexcitation under which the magneto-capacitance measurements are taken. This non-detectable magneto-current phenomenon illustrates that during the magneto-capacitance measurements, transport-based magneto-capacitance is negligible. All these experiment results support our argument that the observed magneto-capacitance comes primarily from magneto-polarization.

4.3.4 Comparison between excited state- and ground state-based π-d electron couplings

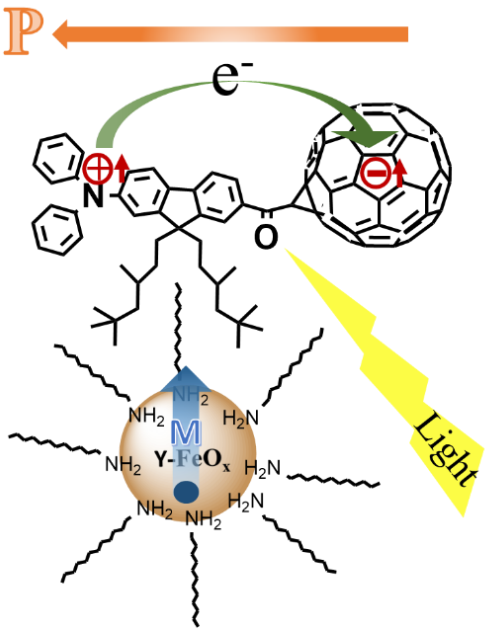

Figure 29 Schematic of the three components in magneto-capacitance from γ-FeO_x-C_{60}(>DPAF-C_9) nanocomposite.

The coupling between π-electron and d-electron in the γ-FeO_x-C_{60}(>DPAF-C_9) nanocomposite in both ground and excited state is further analyzed by using curve fitting from theoretical analysis. Since the organic-magnetic nanocomposite γ-FeO_x-C_{60}(>DPAF-C_9) consists of an organic C_{60}(>DPAF-C_9) component and magnetic γ-FeO_x nanoparticles as shown in Figure 29, the magneto-capacitance can be expressed as:

$$\mathrm{MFC} = C_1 * \frac{B^2}{(|B| + B_0)^2} + C_2 * {M_B}^2 + C_3 * \frac{B^2}{(|B| + B_0)^2} * {M_B}^2 \qquad (7)$$

C_1, C_2, C_3 are the coefficients for the magneto-capacitance signals from C_{60}(>DPAF-C_9), γ-FeO_x, and π-d electron coupling, respectively. B is external magnetic field. B_0 is related to the spin exchange energy in charge-transfer states in the C_{60}(>DPAF-C_9) component. M_B is the magnetization of magnetic γ-FeO_x nanoparticles.

The magneto-capacitance from the organic C_{60}(>DPAF-C_9) component is negligible in dark condition while an appreciable magneto-capacitance occurs when photoexcitation is applied as shown in Figure 27 (b). This magneto-capacitance under photoexcitation can be fitted by the non-Lorentzian function: $\mathrm{MFC(organic)} = P_1 * \frac{B^2}{(|B|+B_0)^2}$ with P_1=2.417E-4 and B_0=10.251 mT.[152-154] The magneto-capacitance from the γ-FeO_x nanoparticles is proportional to the square of its magnetization, given by $\mathrm{MFC(magnetic)} = P_2 * {M_B}^2$.[145, 146, 155, 156] The M-H curve of magnetic γ-FeO_x nanoparticles can be fitted by the equation: $M_B = A_1 e^{-\frac{B}{t_1}} + A_2 e^{-\frac{B}{t_2}} + A_3 e^{-\frac{B}{t_3}} + y_0$ with y_0=5.1465; A_1=-3.2263; t_1=48.7131; A_2=-0.8621; t_2=516.9337; A_3=-1006; and t_3=14.6706. Consequently, the magneto-capacitance from the γ-FeO_x-C_{60}(>DPAF-C_9) composite can be described by Eq. (7) in both ground and excited state. The coefficients of magneto-capacitance from different components are shown in Table I.

Table 1. Parameters from curve fitting with Eq. (7) in Figure 27 (a).

	C_1	C_2	C_3	B_0
0 mW/cm^2	0	4.457E-6	1.490E-6	11.587
31.25 mW/cm^2	4.289E-5	4.659E-6	2.558E-5	10.181

The increase of the magneto-capacitance coefficient (C_1) from negligible to 4.289E-5 upon photoexcitation clearly illustrates that charge-transfer states are formed in the organic C_{60}(>DPAF-C_9) component in the excited state. The negligible change of the magneto-capacitance coefficient (C_2) from 4.457E-6 to 4.659E-6 confirms that the spin polarization of d electrons in γ-FeO_x shows a non-detectable response to photoexcitation. The large change of the magneto-capacitance coupling coefficient (C_3) from 1.490E-6 to

2.558E-5 by a factor of 17 demonstrates that the π-d electron coupling is much stronger in excited state than in ground state. This stronger π-d coupling is confirmed again by the decrease of the spin-exchange energy (B_0) from 11.587 mT to 10.181 mT when the photoexcitation is introduced. Our early studies have shown that interaction between charge-transfer states can weaken the spin-exchange energy of an individual charge-transfer state.[118, 157] Here we find that when we introducing magnetic nanoparticles to form organic-magnetic nanocomposites, the stronger coupling between π electrons and d electrons under photoexcitation can further weaken the spin-exchange energy in charge-transfer states. Therefore, in excited state the semiconducting π electrons and magnetic d electrons are more strongly coupled as compared to ground state.

4.3.5 Discussion

The mechanisms that could be responsible for the interactions between the π and d-electrons are investigated by changing the π-d separation distance to adjust the interaction strength. A simple way of increasing the distance between π and d-electrons is to replace C_{60}(>DPAF -C_9) with C_{60}(>DPAF-C_{12}) (Figure 30) in the mixture with γ-FeO_x particles. Changing the branched alkyl chain from C_9 to unbranched alkyl chain C_{12} can effectively increase the separation distance between π electrons and d electrons.

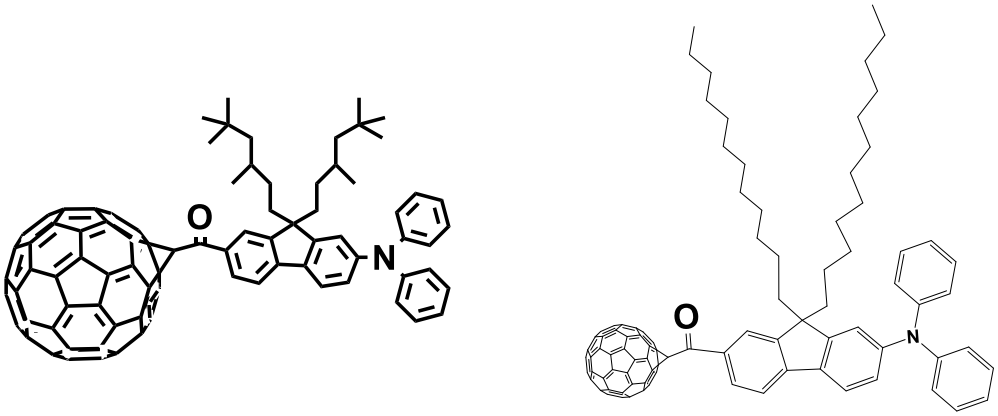

Figure 30 Chemical structure of C_{60}(>DPAF-C_9) and C_{60}(>DPAF-C_{12}).

Increasing in separation distance between π and d electrons lessens amplitude of the magneto-capacitance and the line-shape of the magneto-capacitance as shown in Figure 31. Our former studies indicated two interactions that can change magnetic field effects: the Coulomb interaction and the spin-spin interaction.[118, 157] The Coulomb interaction can weaken the electron-hole Coulomb attraction within the charge-transfer states by redistributing the dipole fields. On the other hand, the Coulomb screening effect increases the distance between electron holes. These two outcomes of the Coulomb interaction can reduce the spin-exchange energy within the individual charge-transfer state, leading to a narrower line-shape and larger magnitude in magnetic field effects. On the contrary, the spin-spin interaction has two outcomes: an increase in the effective spin-orbital coupling and greater spin-exchange energy within charge transfer states. These effects can broaden the line-shape and decrease the magnitude of magnetic field effects.

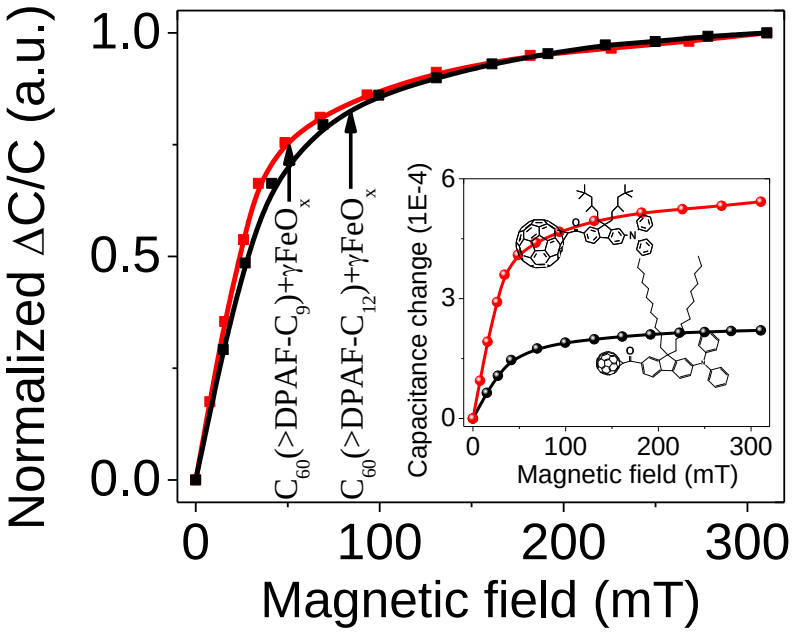

Figure 31 Normalized magneto-capacitance of C_{60}(>DPAF-C_9) and C_{60}(>DPAF-C_{12}) mixing with γ-FeO_x under photoexcitation with 405 nm laser. Inset shows the absolute magneto-capacitance value.

The interactions between π electrons and d electrons in the organic-magnetic nanocomposite, including Coulomb interaction and spin-spin interaction, is described in Figure 32. A Coulomb interaction would result from the coupling of electric dipoles in the charge-transfer states in C_{60}(>DPAF-C_x) (x= 9 or 12) with the electrical polarization of d electrons in γ-FeO_x. A spin-spin interaction would derive from the spin polarization of d electrons in γ-FeO_x and π electrons in C_{60}(>DPAF-C_x) (x= 9 or 12). Increasing the distance between π-electron and d-electron by replacing C_{60}(>DPAF-C_9) with C_{60}(>DPAF-C_{12}) would reduce the Coulomb and spin-spin interactions at the same time. Decreasing the Coulomb interaction would produce a broader magneto-capacitance curve with a smaller value, while decreasing the spin-spin interaction would result in a narrower magneto-capacitance curve with a larger value. The broader line-shape and smaller amplitude of magneto-capacitance thus indicate that the Coulomb interaction would be dominant in π-d electron coupling.

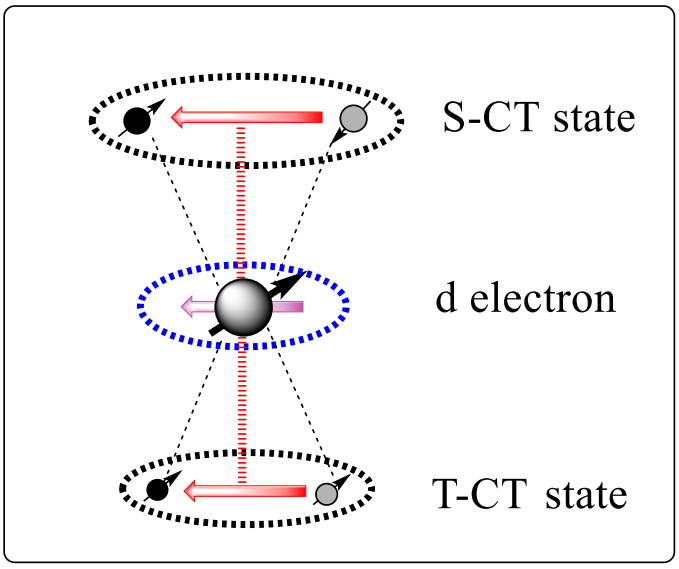

Figure 32 Diagram showing interactions between π and d electrons. Red bold arrows predict the electric polarization while the fine arrows describe the spin. Black dotted lines represent the spin-spin interaction and red dotted ones show Coulomb interaction.

To further verify the Coulomb and spin-spin interactions involved in the coupling of π-electron and d electron in γ-FeO_x-C_{60}(>DPAF-C_9), we study magneto-capacitance by separately changing the electric polarization and spin polarization. Figure 33 (a) shows that simply increasing the intensity of electric polarization through increasing photoexcitation narrows the magneto-capacitance line-shape and raises the magneto-capacitance value of γ-FeO_x-C_{60}(>DPAF-C_9). The narrower line-shape and larger amplitude of magneto-capacitance under higher photoexcitation can be ascribed to two possible Coulomb interactions. First, the Coulomb interaction between charge-transfer states in C_{60}(>DPAF-C_9) becomes stronger due to the increased intensity caused by higher photoexcitation. The increased Coulomb interaction reduces the spin-exchange energy, leading to a larger and narrower magneto-capacitance, as shown in Figure 33 (b). Second, the Coulomb interaction between the charge transfer states in C_{60}(>DPAF-C_9) and d-electrons in γ-FeO_x change the magnitude and line-shape of the magneto-capacitance concurrently. This Coulomb interaction is enhanced by the larger number of charge-transfer states in C_{60}(>DPAF-C_9) that result from the higher photoexcitation. The increased Coulomb interaction can further reduce the spin-exchange energy within charge-transfer states, with an out of smaller value and narrower line-shape of the magneto-capacitance.

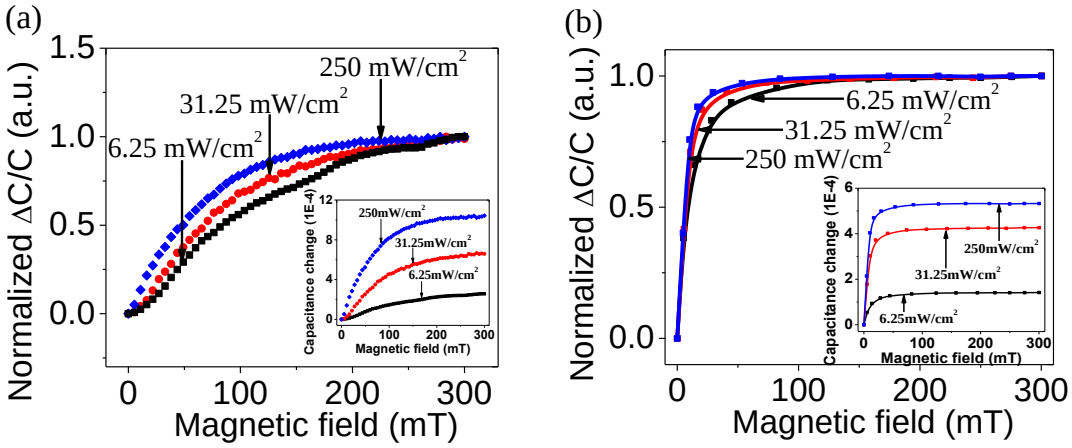

Figure 33 Normalized magneto-capacitance curves from(a) γ-FeO_x-C_{60}(>DPAF-C_9) and (b) C_{60}(>DPAF-C_9) with increasing photoexcitation intensities. Inset: absolute value of magneto-capacitances.

In order to distinguish the Coulomb interaction between charge transfer states and d electrons, we compare the half width at half maximum (HWHM) of magneto-capacitance under varied photoexcitation as shown in Figure 34 (a). It is clear that the HWFM of the magneto-capacitance from the organic-magnetic nanocomposites γ-FeO_x-C_{60}(>DPAF-C_9) decreases as photoexcitation becomes more intense. The large slope of HWHM decrease straightforwardly demonstrates that the Coulomb interaction between π-electron and d electron is dominated to weaken the spin-exchange energy through π-d electron coupling. In addition, combining magnetic nanoparticles γ-FeO_x with C_{60}(>DPAF-C_9) leads to a much larger magneto-capacitance under a given photoexcitation, further illustrating the dominant effect of the Coulomb interaction between the π and d electrons.

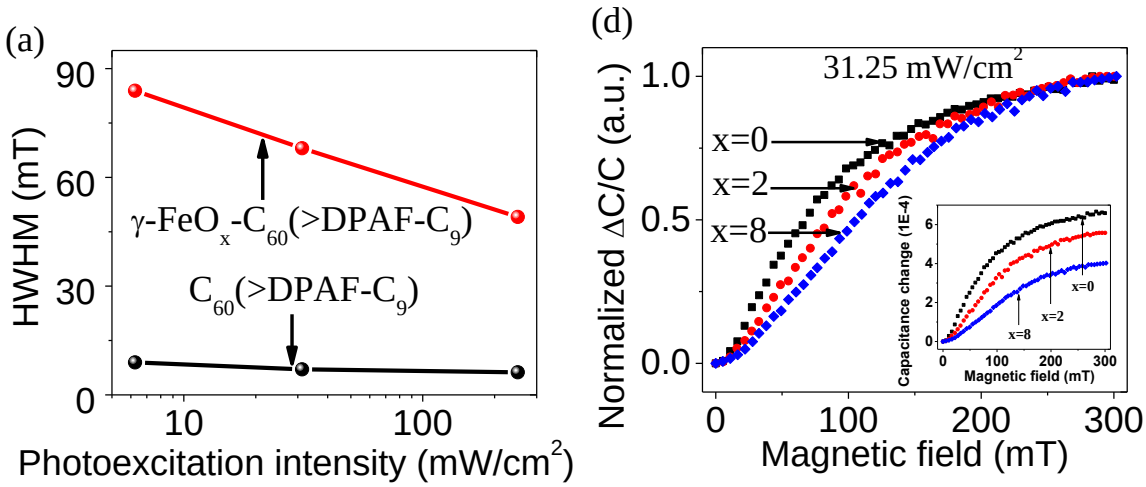

Figure 34 (a) Comparison of HWHM between γ-FeO_x-C_{60}(>DPAF-C_9) and C_{60}(>DPAF-C_9). (b) Normalized magneto-capacitance curves from γ-FeO_x-C_{60}(>DPAF-C_9) mixed with iron oxide nanoparticles with different weight ratios; inset: absolute value of magneto-capacitance.

The HWHM of magneto-capacitance in γ-FeO_x-C_{60}(>DPAF-C_9) is also much larger than that in C_{60}(>DPAF-C_9), as shown in Figure 34 (a), indicating a broader line-shape of magneto-capacitance. It is known that spin-spin interaction occurs in the π-d electron coupling, as illustrated in Figure 32. On one hand, the enhanced spin-spin interaction can increase the spin-orbital coupling within charge-transfer states in

C_{60}(>DPAF-C_9), increasing the spin-spin interaction can also strengthen the spin-exchange energy within charge-transfer states in C_{60}(>DPAF-C_9). Both of these two outcomes retard the changing rate of singlet/triplet ratio under the external magnetic field, producing a magneto-capacitance with a broader line-shape and smaller value. The broader line-shape of magneto-capacitance from organic-magnetic nanoparticles γ-FeO_x-C_{60}(>DPAF-C_9) indicates that spin-spin interaction between π and d electrons also increases as photoexcitation becomes more intense.

To investigate the effect of the spin-spin interaction further, we change the density of spin dipoles by varying the concentration of magnetic nanoparticles. As shown in Figure 34 (b), increasing the intensity of spin polarization results in a magneto-capacitance with a smaller value and a broader line-shape. This phenomenon illustrates that the spin-spin interaction between the π and d electrons becomes stronger as the intensity of spin polarization increases. Consequently, magneto-capacitance measurements with different intensities of π and d electrons demonstrate that the interaction between π-electron and d-electron contains the Coulomb and spin-spin interactions.

4.4 Conclusion

In conclusion, the π-d electron coupling in both ground state and excited state are studied by using magneto-capacitance measurements based on the organic-magnetic γ-FeO_x-C_{60}(>DPAF-C_9) nanocomposites. These magneto-capacitance measurements show that the π-d electron coupling occurs in both ground state and excited state with a largely enhanced π-d electron coupling in excited state. The two mechanisms responsible for this coupling are identified as the Coulomb interaction and the spin-spin interaction, a result verified by varying electric polarization and spin polarization through tuning the intensity of photoexcitation and the concentration of magnetic nanoparticles, respectively. The Coulomb and spin-spin interactions mutually compete to determine the spin-exchange and spin-orbital interactions in the charge-transfer states, as demonstrated by the magnitude and line-shape of magneto-capacitance. This study provides a new method for tuning π-d electron coupling by using excited state for developing excited states-based magnetoelectronic applications.

CHAPTER 5

INTERACTION BETWEEN PHOTO-GENERATED CHARGE-TRANSFER STATES AND MAGNETIZED CHARGE-TRANSFER STATES

The interaction between optical charge-transfer states and magnetized charge-transfer states is studied by the magneto-dielectric measurement. Combining the optical CT states and magnetized CT states yields a new magneto-dielectric signal with distinctive line-shape and amplitude comparing to the signal from individual charge-transfer states, indicating a coupling between optical CT states and magnetized CT states. The coupling between optical CT states and magnetized CT states experiences long-range Coulomb and medium-range spin-orbital interactions by changing (i) the density of optical CT states and (ii) the separation distance between optical CT states and magnetized CT states.

5.1 Introduction

Optical charge-transfer states can be generated at intermolecular interfaces in organic materials under photoexcitation. Actually, they are essentially electrical dipoles generated through a charge-transfer process.[111, 158, 159] In general, the optical CT states process multiple functions in organic semiconducting materials involved in light-emitting, photovoltaic, lasing, and dielectric actions. Furthermore, the optical CT states can be formed as singlets and triplets with respective populations. The ratio between singlets and triplets is determined by the competition between spin-conserving and spin-mixing controlled by spin-exchange interaction and hyperfine or spin-orbital coupling respectively. In particular, the singlet and triplet populations can be facially modified by a low magnetic field (< 100 mT) at room temperature through perturbing either spin-conserving or spin-mixing, leading to magnetic field effects on light-emitting, photovoltaic, and dielectric properties.[12, 108, 111, 118, 129, 130, 160-164] As a result, using optical CT states presents a unique approach to develop magneto-optic and magneto-electric properties in excited states. On the other hand, a 2D ferromagnetic/semiconducting interface can form magnetized CT states due to direct charge transfer or wavefunction hybridization.[165-168] In the magnetized CT states, both spin and electrical dipoles are oriented, leading to an electrically polarized spin interface. It has been experimentally found that magnetized CT states can function as a spin filter to enhance spin transport.[166, 169, 170] Furthermore, through magneto-electric coupling, magnetized CT states can offer a mutual tuning mechanism between magnetic and electric properties based on a ferromagnetic/semiconducting interface.[171-176] Here, we

combine a ferromagnetic/semiconducting interface with molecular donor:acceptor composites through thin-film design in the device with architecture of ITO/TPD:BBOT/TPD/Co/Al to fabricate optical CT states and magnetized CT states under photoexcitation. We find that the Co/TPD interface exhibits a magneto-dielectric function at room temperature by measuring the magneto-dielectric, indicating that the Co/TPD interface becomes an electrically polarized spin interface. Furthermore, the optical CT states are coupled with magnetized CT states under photoexcitation, presenting a convenient approach to generate optically tunable spin interface based on thin-film design.

5.2 Experiments

TPD, BBOT, PMMA and Co were purchased from Aldrich and used as received. For the study of interactions between magnetized CT states and optical CT states, devices with structures of ITO/TPD:BBOT/Al, ITO/TPD:BBOT/TPD/Al and ITO/TPD:BBOT/TPD/Co/Al were fabricated. The pre-cleaned ITO substrates were treated with UV-zone before device fabrication. The TPD: BBOT layers were spin cast onto the ITO substrate from chloroform solutions, resulting in smooth films with a thickness of 300 nm. TPD thin films, Co layers and aluminum electrodes were deposited onto the organic layers by thermal evaporation in a high-vacuum chamber under a pressure of 2×10^{-6} Torr.

The capacitance was measured by an Agilent E4980A LCR meter under zero DC bias and 50 mV AC field. A solid-state, 405 nm CW laser was used for photoexcitation to generate intermolecular excited states in the TPD:BBOT:PMMA composites. The magneto-dielectric (MFC) was defined as $\mathrm{MFC} = \frac{C_B - C}{C} = \frac{\Delta C}{C}$, where C_B and C are the capacitances with and without magnetic field, respectively.

5.3 Results and discussion

5.3.1 Magnetized Charge-Transfer States

The device with the structure of ITO/TPD/Co/Al as shown in Figure 35 (a) is used to generate magnetized charge-transfer states. Figure 35 (b) depicts the magneto-dielectric characteristics from ITO/TPD/Co/Al and ITO/TPD/Al devices measured under a 1 kHz

alternating voltage of 50 mV without a DC bias under dark condition. It is clearly that inserting a thin Co layer between TPD increases the capacitance with magnetic field. The positive magneto-dielectric indicates that there is a magneto-dielectric coupling occurring at the interface between TPD and Co. It is known that CT states formed at the ferromagnetic metal/organic semiconducting interface have spin polarizations due to the coupling between π electrons in semiconducting materials and d electrons in ferromagnetic metals.[177, 178] Consequently, the electric polarization of the magnetized charge carriers can be changed by applying an external magnetic field through manipulating their spin polarization, generating a magneto-dielectric coupling at the interface. In our system, the N atoms in TPD, bearing lone electron pairs, can interact with the d electrons in Co atoms at the Co/TPD interface by electron-transfer from N atoms in TPD to the intermediate state formed by interaction between π electrons in TPD and d electrons in Co. This results in spin polarized charge-transfer states at the TPD/Co interface, which is reflected by the magneto-dielectric signal.

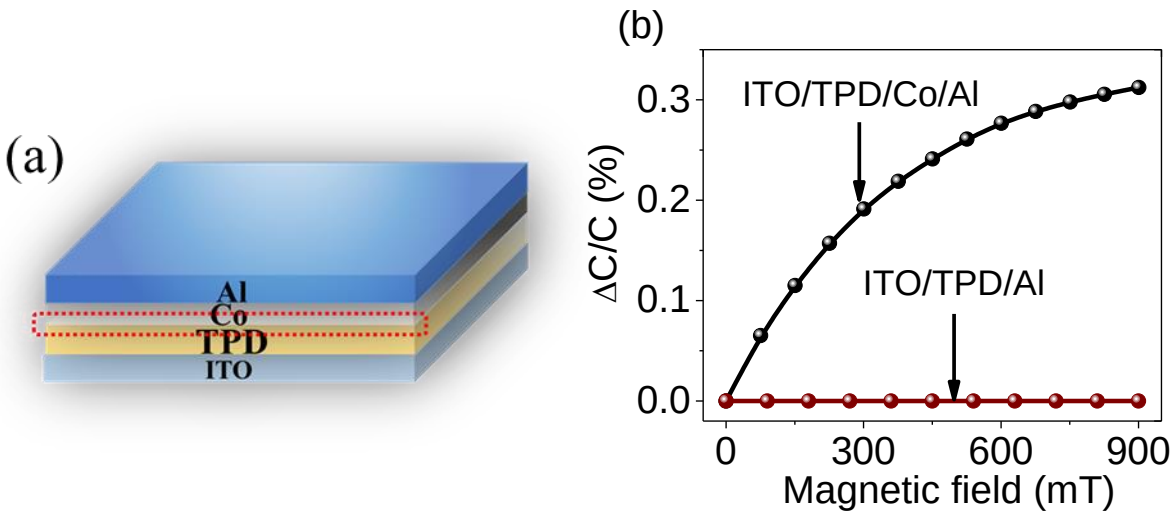

Figure 35 (a) Device structure for generating the magnetized CT states at the TPD/Co interface. (b) Magneto-dielectric signals from devices with the structure of ITO/TPD(60 nm)/Co(7 nm)/Al and ITO/TPD(60 nm)/Al under dark condition.

5.3.2 Optical Charge-Transfer States

The device with structure of ITO/TPD:BBOT/Al as shown in Figure 36 (a) are used to produce optical charge-transfer states under photoexcitation. Figure 36 (b) shows that photoexcitation leads to an increase in magneto-dielectric, which increases fast at low magnetic field and saturates at high magnetic field, leading to a narrow, Lorentzian line-shape. On the contrary, magneto-dielectric from this device is negligible under dark condition. Our former studies show that pure TPD and BBOT do not exhibit magneto-dielectric.[118] Therefore, the positive magneto-dielectric originates from the TPD/BBOT interface in the bulk heterojunction. It is known that intermolecular charge-transfer states can be formed at the TPD/BBOT interface under photoexcitation. Based on the following two facts: (i) the singlet/triplet ratio of intermolecular charge-transfer states can be changed by an external magnetic field through perturbing the intersystem crossing and (ii) singlets and triplets have different electric polarization.[54, 110, 112, 142, 143] The positive magneto-dielectric is ascribed to the optically induced intermolecular CT states at the TPD:BBOT interface in the bulk heterojunction. Accordingly, the positive magneto-dielectric signals from the ITO/TPD:BBOT/Al devices indicate the formation of optical CT states in the TPD:BBOT bulk heterojunction.

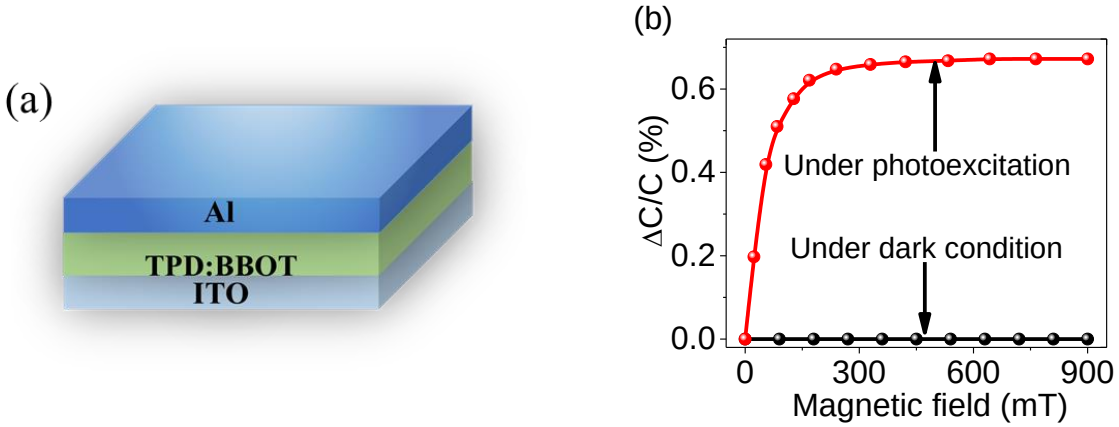

Figure 36 (a) Device structure for generating the optical CT states at the TPD/Co interface. (b) Magneto-dielectric from device of ITO/TPD:BBOT:PMMA/Al both in ground and excited states.

5.3.3 Interaction between Magnetized CT states and Optical CT states

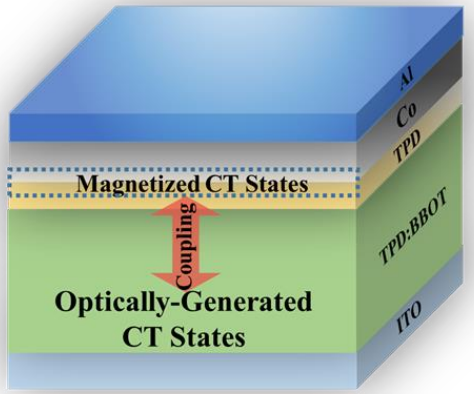

Figure 37 Device structure for demonstrating the interaction between optical CT states and magnetized CT states.

The interaction between the magnetized CT states and the optical CT states is studied by combining them together in the device ITO/TPD:BBOT/TPD/Co/Al as shown in Figure 37. Depositing a thin layer of TPD on optical CT states generates a magneto-dielectric signal exhibiting appreciable value with an initial negative component at low field (< 40 mT) followed by a positive component at high field (> 40 mT) showing in Figure 38 (a). Whilst, no negative magneto-dielectric is observed in the device ITO/TPD:BBOT/Al without the TPD layer (Figure 36 (b)). Therefore, the negative magneto-dielectric signal is ascribed to the interface between the TPD:BBOT bulk heterojunction and the TPD thin layer. Under photoexcitation, excitons in TPD transfer to the interface between TPD and BBOT to dissociate into electron-hole pairs. Therefore, excitons from the thin TPD layer and charge carriers from the TPD:BBOT heterojunction interact with each other at the interface, leading to triplet-charge reaction. In general, an external magnetic field can weaken the triplet-charge reaction, resulting in a reduction of free charge carriers.[103, 179, 180] Together with the fact that singlet optical CT states tend to dissociate into free carriers, the reduced charge carriers from decreased triplet-charge reaction under an external magnetic field promote singlet optical CT states into free

carriers. It reduces the number of singlet optical CT states, producing a negative magneto-dielectric. Combined with the positive magneto-dielectric from optical CT states in TPD:BBOT heterojunction, the magneto-dielectric turns into positive value with increasing external magnetic field. In this study, we focus on the interaction between optical CT states and magnetized CT states. Here, after combining the magnetized CT states and optical CT states by depositing a Co layer on top of the thin TPD layer, the amplitude of magneto-dielectric increases. The increased magneto-dielectric signal demonstrates that the magnetized CT states and optical CT states interact with each other. Furthermore, combining the magnetized CT states and the optical CT states leads to a narrower line-shape in magneto-dielectric as shown in Figure 38 (b). It is known that the decrease of spin-exchange energy in the optical CT states can increase the changing rate of singlet/triplet ratio ($\frac{\partial(\frac{S}{T})}{\partial B}$), leading to a narrower line-shape of magnetic field effects.[12, 118] Therefore, the narrower line-shape of the magneto-dielectric curve illustrates a decrease in spin-exchange energy in optical CT states caused by the interaction between magnetized CT states and optical CT states.

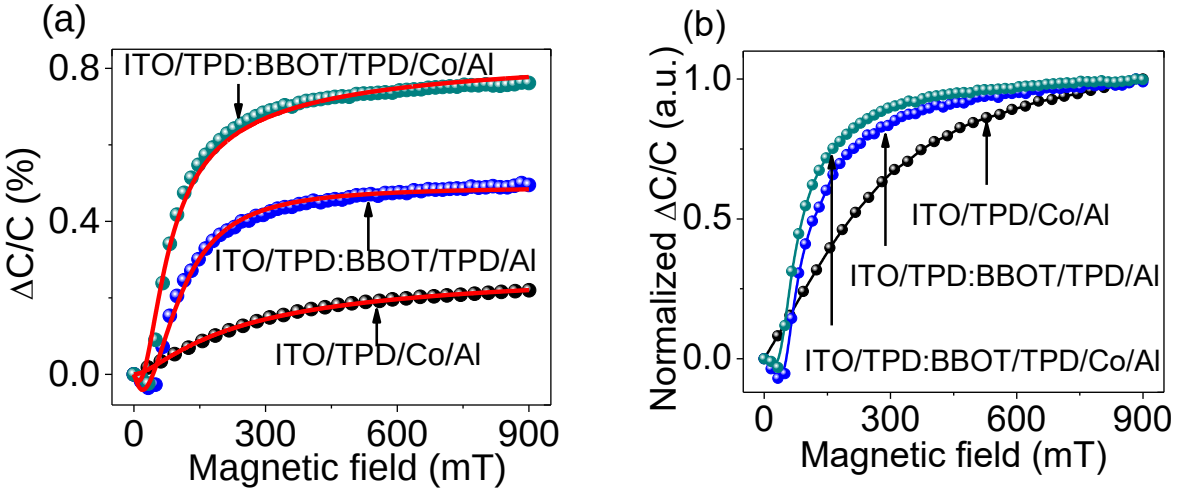

Figure 38 (a) Magneto-dielectric signals from devices ITO/TPD/Co/Al, ITO/TPD:BBOT/TPD/Al and ITO/TPD:BBOT/TPD/Co/Al under photoexcitation. The red solid lines are fitting curves. (b) Normalized magneto-dielectric signals.

Next, the interaction between the optical CT states and the magnetized CT states is theoretically analyzed using the interaction coefficients from fitting the magneto-dielectric signals. Three components that respectively describe (i) the magneto-dielectric from optical CT states, (ii) the magneto-dielectric from magnetized CTs and (iii) the magneto-dielectric from the interaction between optical CT states and magnetized CT states are combined to describe the overall magneto-dielectric as:

$$MFC_{Total} = MFC_{P-CTs} + MFC_{M-CTs} + MFC_{Interaction}$$
$$= \left(\beta \frac{B^2}{(B+B_1)^2} + b\frac{B^2}{B^2+{B_2}^2}\right) + \alpha \frac{B^2}{(B+B_0)^2} + c * b\frac{B^2}{B^2+{B_2}^2} * \alpha \frac{B^2}{(B+B_0)^2} \quad (8)$$

β, b, α and c are the coefficients for the magneto-dielectric signals from triplet charge reaction, optical CT states, magnetized CT states and interaction between optical CT states and magnetized CT states, respectively. B is the external magnetic field. B_1, B_2 and B_0 are constants corresponding to the spin exchange energy in triplet charge reaction, optical CT states and magnetized CT states, respectively. Using Equation (8) requires the determination of the magneto-dielectrics of optical CT states and magnetized CT states. Figure 38 (a) shows that the optical CT states can be fitted by the function: $MFC_{P-CTs} = \beta \frac{B^2}{(B+B_1)^2} + b\frac{B^2}{B^2+{B_2}^2}$, where β=-0.0014, b=0.0063, B_1=9.02 mT and B_2=102.76 mT. Furthermore, the magneto-dielectric from magnetized CT states can be given by the function: $MFC_{M-CTs} = \alpha \frac{B^2}{(B+B_0)^2}$, where α=0.00284 and B_0=120.70 mT. Consequently, fitting the magneto-dielectric curve for ITO/TPD:BBOT/TPD/Co/Al device with Equation (8) determines the magneto-dielectric coefficients of b=0.0068, c=13.15 and B_2=68.24 mT. The large coupling coefficient c=13.15 clearly indicates the interaction between magnetized CT states and optical CT states. Additionally, the spin exchange energy (B_2) in optical CT states decreases from 102.76 mT to 68.24 mT when interaction between optical CT states and magnetized CT states is introduced, indicating a narrower line-shape of magneto-dielectric (Figure 38 (b)). Our earlier studies showed that the Coulomb interaction between the charge-transfer states can weaken the spin-exchange energy within

individual optical CT states, leading to a narrower magnetic field effects line-shape.[12, 118, 164] Here, we find that the combination of optical CT states and magnetized CT states further weakens the spin exchange energy within optical CT states to generate a narrower magneto-dielectric line-shape, indicating the interaction between the optical and magnetized CT states.

5.3.4 Photo-tunable interaction

In order to further confirm the interaction between magnetized CT states and optical CT states, we adjust the interaction strength through tuning the density of the optical CT states by varying photoexcitation intensity. Figure 39 (a) indicates that increasing the photoexcitation intensity leads to a larger magneto-dielectric value. In addition, the line-shape narrows as the photoexcitation intensity increases (Figure 39 (b)). These phenomena indicate that the interaction between magnetized CT states and optical CT states is changeable by tuning the photoexcitation intensity.

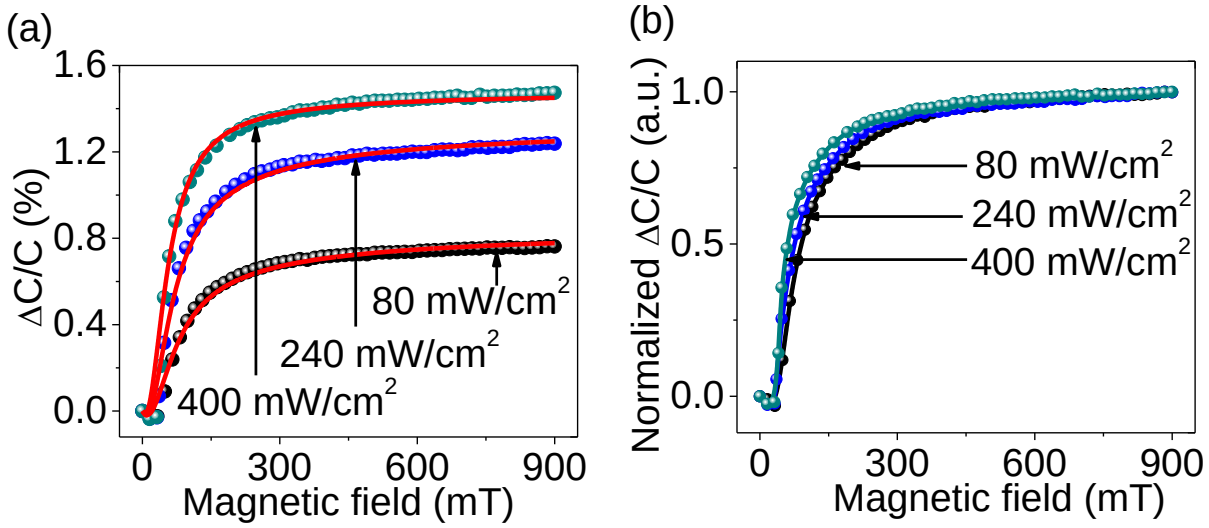

Figure 39 (a) Magneto-dielectric from the device of ITO/TPD:BBOT/TPD(10 nm)/Co/Al under different photoexcitation intensities. Red solid lines are the fitting curves. (b) Normalized magneto-dielectric from the ITO/TPD:BBOT/TPD(10 nm)/Co/Al device.

There are two possible mechanisms responsible for the magneto-dielectric change with the photoexcitation intensity. First, the optical CT states interact with each other to

reduce the spin-exchange energy of individual optical CT states, leading to a larger and narrower magneto-dielectric (Figure 40 (a)). Second, the interactions between optical CT states and magnetized CT states decrease the spin-exchange energy of optical CT states, further increasing and narrowing the magneto-dielectric.

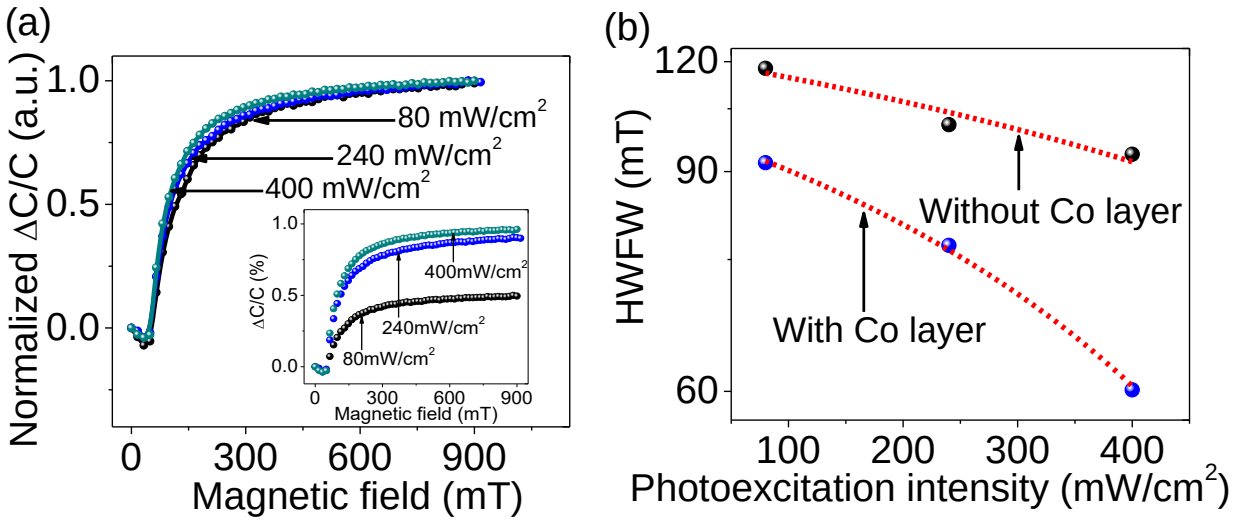

Figure 40 (a) Normalized magneto-dielectric from ITO/TPD:BBOT/TPD(10 nm)/Al under different photoexcitation intensities. Inset: the original magneto-dielectric curves. (b) HWHM of magneto-dielectric between devices with and without Co layer.

In order to distinguish between these two possible mechanisms, the half width at half maximum (HWHM) of the magneto-dielectric from devices with structure of ITO/TPD:BBOT/TPD/Co/Al and ITO/TPD:BBOT/TPD/Al as a function of photoexcitation intensity are compared (Figure 40 (b)). Clearly, increasing photoexcitation leads to a smaller HWHM from the ITO/TPD:BBOT/TPD/Al device, demonstrating the reduced spin-exchange energy in individual optical CT states through the interaction between them. Furthermore, the HWHM of magneto-dielectric from the ITO/TPD:BBOT/TPD/Co/Al device is smaller than that from the ITO/TPD:BBOT/TPD/Al device under the fixed photoexcitation intensity, reflecting a faster changing rate of singlet/triplet ratio ($\frac{\partial(\frac{S}{T})}{\partial B}$). It is known that the change rate of singlet/triplet ratio is determined by the spin-exchange energy of individual optical CT states: external magnetic

field can change the singlet/triplet ratio much faster when the spin-exchange energy is smaller.[12] Therefore, the smaller HWHM from the ITO/TPD:BBOT/TPD/Co/Al device directly illustrates a further reduced spin-exchange energy, anticipating the interaction between magnetized CT states and optical CT states. More importantly, it is clearly shown that the HWFM from the device ITO/TPD:BBOT/TPD/Co/Al decreases much faster with increasing photoexcitation intensity, predicting the stronger interaction between magnetized CT states and optical CT states under higher photoexcitation intensity. Consequently, the magnetized CT states and optical CT states interact with each other. Increasing the density of optical CT states can enhance this interaction.

We also study the photo-enhanced interaction between magnetized CT states and optical CT states by fitting magneto-dielectric under different photoexcitation intensities with Equation (8) (red lines in Figure 39 (a)), as shown in Table 2. The coupling coefficient c greatly increases under higher photoexcitation intensity, demonstrating the enhanced interaction between magnetized CT states and optical CT states. The decreasing of spin exchange energy (B_2) of optical CT states further confirms the larger interaction between optical CT states and magnetized CT states under higher photoexcitation intensity. It is known that higher photoexcitation can enhance the density of electrical dipoles of optical CT states by producing larger number of optical CT states.[157] Therefore, the interaction between magnetized CT states and optical CT states originates from the Coulomb interaction between them through electrical dipole-dipole interaction.

Table 2. Parameters from curve fitting with Eq. (5.1) in Figure 39 (a).

	b	c	B_2
80 mW/cm^2	0.0068	13.15	68.24
240 mW/cm^2	0.0115	109.82	59.14
400 mW/cm^2	0.0155	164.43	50.66

5.3.5 Distance-tunable interaction

The interaction between magnetized CT states and optical CT states is further investigated via tuning the distance between them by manipulating the TPD thickness. Figure 41 (a) shows that increasing the TPD thickness leads magneto-dielectric to a broader line-shape, illustrating a larger spin-exchange energy in individual optical CT states. Increasing the TPD thickness increases the distance between magnetized CT states and optical CT states, generating a weaker interaction between them. Therefore, the weaker interaction increases the spin-exchange energy in individual optical CT states to develop the broader line-shape. Figure 41 (b) describes that the value of magneto-dielectric becomes smaller as the TPD thickness decreases. Normally, increasing the Coulomb interaction between magnetized CT states and optical CT states with a thinner TPD thickness should lead to a larger magneto-dielectric. This smaller magneto-dielectric with a thinner TPD layer illustrates that another mechanism is needed to explain the decreasing magneto-dielectric value with the thinner TPD thickness. Generally, increasing the spin-orbital interaction between two different charge-transfer states can essentially increase the effective spin-orbital coupling of each of the charge-transfer states, generating a decrease of magnetic field effects.[12, 24, 181] Consequently, the decreased value of magneto-dielectric indicates that the spin-orbital coupling is another important mechanism in determining the interaction between optical CT states and magnetized CT states.

We further demonstrate the distance-tunable interaction between magnetized CT states and optical CT states through fitting the magneto-dielectric curves (red lines in Figure 41 (b)) with Equation (8) with parameters shown in Table 3. We can directly see that the coupling coefficient c decreases with increasing TPD thickness. This thickness-induced decreasing of the coupling coefficient illustrates that the interaction between magnetized CT states and optical CT states becomes smaller with thicker TPD thickness. On the other hand, the spin exchange energy (B_2) of optical CT states increases with thickness of the TPD layer. Increasing the distance between optical CT states and magnetized CT states produces a decreased interaction between them, leading to a larger spin-exchange energy in individual optical CT states. Consequently, this distance-related value of spin exchange energy further demonstrates the weaker interaction between

magnetized CT states and optical CT states when the distance between them becomes larger.

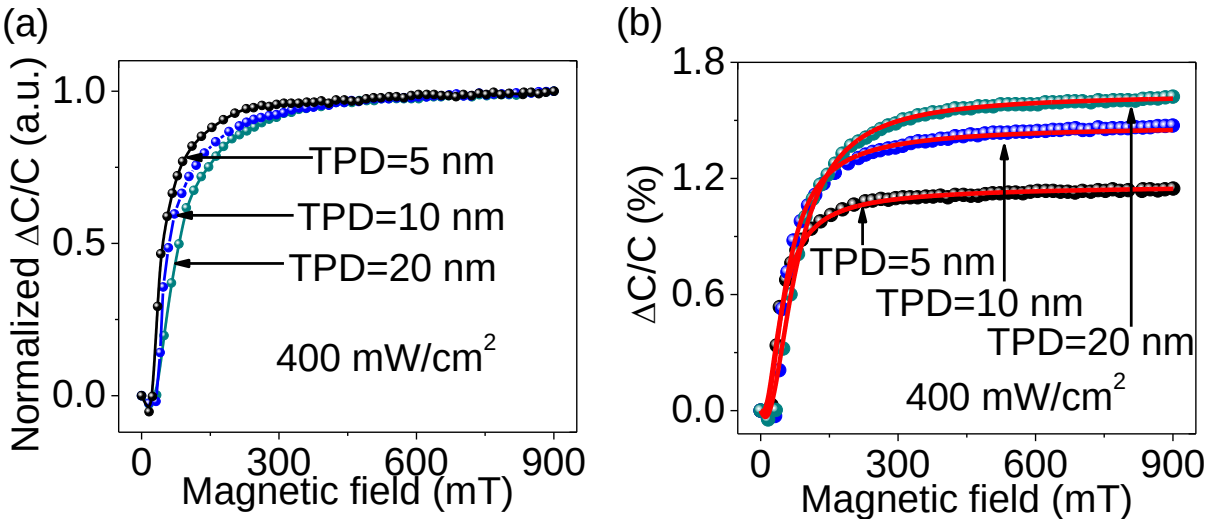

Figure 41 (a) Normalized magneto-dielectric from device ITO/TPD:BBOT/TPD/Co/Al with different TPD thickness. (b) Absolute value of magneto-dielectric from device ITO/TPD:BBOT/TPD/Co/Al with different TPD thickness. The red lines are fitting curves.

Table 3. Parameters from curve fitting with Eq. (5.1) in Figure 41 (b).

	b	c	B_2
5 nm	0.0125	178.91	40.95
10 nm	0.0155	164.43	50.66
20 nm	0.0175	108.27	72.48

5.3.6 Discussion

In general, the interaction between magnetized CT states and optical CT states can occur via two possible mechanisms: Coulomb interaction and spin-orbital interaction. The Coulomb interaction comes from the electrical dipole-dipole coupling since the magnetized CT states and optical CT states can be treated as electrical dipoles. The Coulomb interaction can generate two outcomes: (1) weakening the Coulomb interaction between

the electron and hole in single photo-induced CT states due to the dipole field redistribution; (2) increasing the electron hole distance in single optical CT states via Coulomb shielding effect. These two outcomes can decrease the spin-exchange energy in single optical CT states by increasing the electron-hole separation, leading to a narrower line-shape and larger value of magneto-dielectric. The spin-orbital interaction is equivalent to intermolecular spin-orbital coupling between two molecules.[24, 181] It can increase the effective spin-orbital coupling of single optical CT states, which can generate a broader line-shape and smaller magnitude of magneto-dielectric. Therefore, the interaction between optical CT states and magnetized CT states can be explained by the combination of Coulomb interaction and spin-orbital interaction as shown in Figure 42.

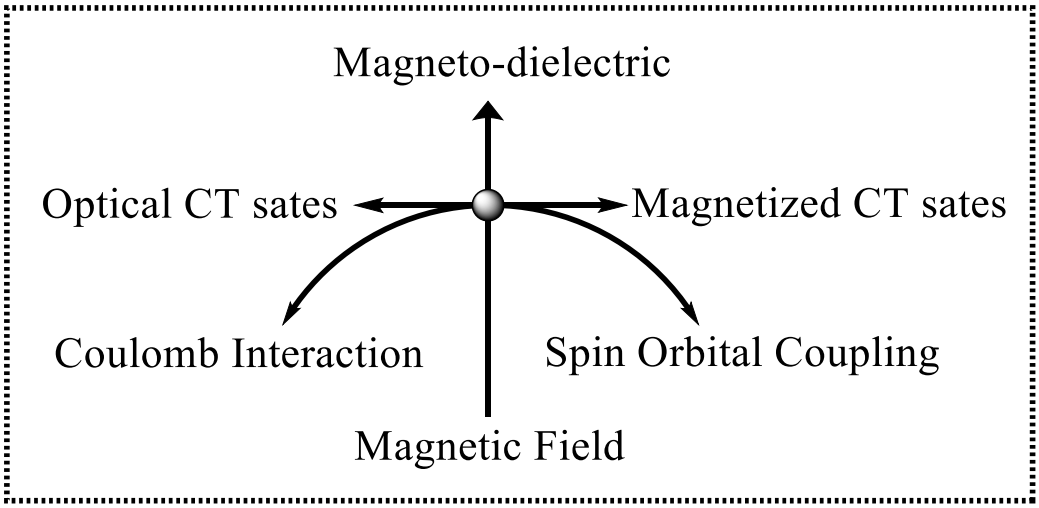

Figure 42 Schematic of the mechanisms to explain the interaction between optical CT states and magnetized CT states.

Higher photoexcitation produces a larger density of optical CT states, leading to more electrical dipoles to Coulombically interact with the magnetized CT states. This increased Coulomb interaction can reduce the spin-exchange energy in individual optical CT states, resulting in a narrower line-shape and larger value of magneto-dielectric. On the other hand, the number of magnetized CT states is reduced under higher photoexcitation demonstrated by the smaller magneto-dielectric signal as shown in Figure 43. Therefore, the spin-orbital coupling between optical CT states and magnetized CT states decreases,

with an outcome of a narrower curve and a larger value of magneto-dielectric. Consequently, increasing the density of optical CT states can enhance the Coulomb interaction and reduce the spin-orbital interaction, leading to a narrower magneto-dielectric line-shape and a larger magnitude.

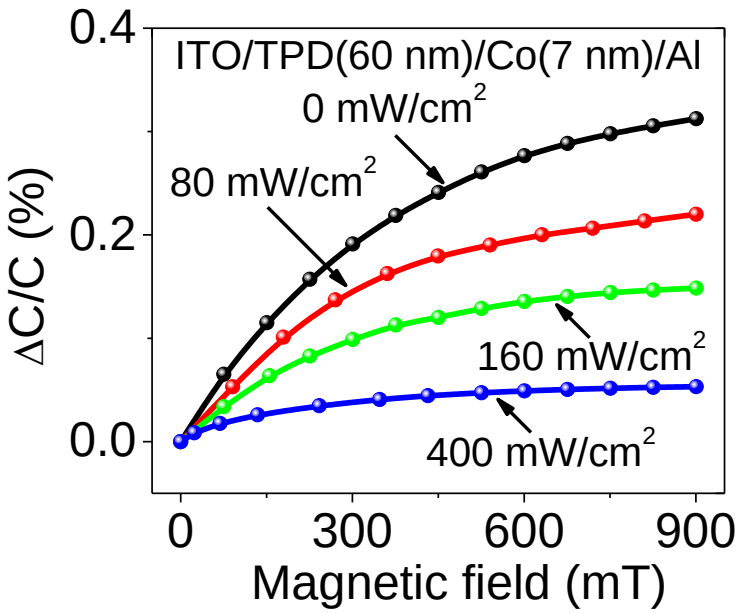

Figure 43 Magneto-dielectric from device of ITO/TPD(60 nm)/Co(7 nm)/Al under different photoexcitation intensities.

When the charge-transfer states are treated as electric dipoles, the energy from the Coulomb interaction between optical CT states and magnetized CT states can be expressed as $U = \frac{\boldsymbol{p_1}\cdot\boldsymbol{p_2}-3(\boldsymbol{p_1}\cdot\hat{\boldsymbol{r}})(\hat{\boldsymbol{r}}\cdot\boldsymbol{p_2})}{4\pi\varepsilon r^3}$. Considering the spin-orbital coupling between optical CT states and magnetized CT states, the energy from spin-orbital coupling can be described as $U = \frac{\mu_B\cdot E}{\hbar mc^2}\cdot\frac{1}{r^2}\cdot\vec{L}\cdot\vec{S}$. It is clear that Coulomb interaction is inversely proportional to the distance cubed while spin-orbital coupling is inversely proportional to the distance squared. Therefore, increasing the distance between magnetized CT states and optical CT states can weaken the Coulomb interaction and spin-orbital interaction directly. The decrease in Coulomb interaction should result in a broader and smaller magneto-dielectric while the

spin-orbital coupling should result in a narrower and larger magneto-dielectric. However, the line-shape of magneto-dielectric is determined by the changing rate of singlet/triplet ratio $\frac{\partial(\frac{S}{T})}{\partial B}$, which is related to the spin-exchange energy in single charge-transfer states. Combining the fact that spin-exchange energy is modified by the Coulomb interaction, it is clear that Coulomb interaction determines the line-shape of magneto-dielectric when changing the distance between photo-induced charge transfer states and magnetized CT states. On the other side, the magnitude of magneto-dielectric is determined by the singlet/triplet ratio. The singlet/triplet ratio in the high magnetic field region in this study is controlled by the competition of external magnetic field and internal magnetic field from spin-orbital coupling. Consequently, the magnitude of magneto-dielectric is determined by spin-orbital coupling. Therefore, increasing the distance between optical CT states and magnetized CT states weakens the Coulomb interaction and spin-orbital interaction, leading to a broader line-shape and larger amplitude, respectively.

5.4 Conclusion

In summary, we study the interaction between optical CT states and magnetized CT states by using magneto-dielectric measurement. The photo-tunable and distance-changeable magneto-dielectric phenomenon demonstrates the variable interaction strength between optical CT states and magnetized CT states. In addition, analysis indicates that this interaction is due to the Coulomb interaction and spin-orbital coupling between the optical CT states and magnetized CT states. This study suggests a new way to combine the electric and magnetic properties through charge-transfer states in organic semiconducting materials under photoexcitation, presenting a new method to study the magneto-electric coupling for future electric, magnetic and optic applications in excited states.

CHAPTER 6

INTERACTION BETWEEN EXCITONS AND FREE CHARGE CARRIERS IN ORGANO-METAL HALIDE PEROVSKITES

Organo-metal halide perovskites, considered to be a semiconducting material with Wannier excitons of low binding energy, provide a new way for next generation solar cells due to the incredible increasing of the efficiency. In this chapter, the magneto-current and magneto-photocurrent studies indicate the coexistence of free charge carries and excitons in perovskites. Furthermore, the interaction between free charge carriers and excitons are also demonstrated by the amplitude and sign change of the magneto-current and magneto-photocurrent signals. This interaction is consolidated by tuning the concentration of excitons through increasing the injection current, rising the photoexcitation intensities, confinement effect and decreasing the temperature.

6.1 Introduction

Organo-metal halide perovskites (OMHPs) have achieved amazing improvements in reaching high efficiency solar cells in the past 5 years. The power conservation efficiencies have dramatically increased from 3% up to 20% by the utilization of materials processing and device engineering.[74, 75, 182-187] The high efficiency of OMHPs is due to their near-optimal direct band gap,[72, 76] high optical absorption,[73, 77] high carrier mobility,[74, 78-82] long carrier diffusion length,[83, 84] and its spontaneous electronic polarization.[85-88] However, there is still a fundamental question involved in photovoltaic mechanism: whether the bound excitons exist in the bulk OMHPs during the photovoltaic process.[188-191] The binding energy of excitons in OMHPs has been reported in the range of 20-150meV, which is in the order of thermal energy at room temperature.[95, 192, 193] Therefore, many studies show that almost neat free charge carriers are generated due to this small binding energy in working solar cells.[68, 194-196] Nonetheless, excitons are also demonstrated to exist based on the observation of coincidence of hot exciton relaxation and cold exciton relaxation.[97, 197] Furthermore, both free charge carriers and excitons are found to be generated simultaneously under higher photoexcitation intensity, larger photoexcitation energy and low temperature.[198-200] Consequently, more studies are needed to answer the fundamental question of the coexistence and interaction between excitons and free charge carriers in OMHPs. In this study, the magnetic field effects on both the injection current (magneto-current) and photocurrent (magneto-photocurrent) are carried

out under different conditions, illustrating the coexistence and interaction of free charge carriers and excitons in OMHPs.

Generally, free carriers in OMHPs can be captured to form electron-hole pairs due to the Coulomb attraction when they are in the mutual capture radius.[197, 201, 202] These electron-hole pairs generate two opposite outcomes: (i) recombining or (ii) dissociating with each other to form luminescence and current respectively. Recently, studies have shown that the charge recombination and dissociation in OMHPs is spin dependent.[96, 97] Therefore, applying an external magnetic field can tune the branching ratio between spin-parallel and spin-antiparallel electron-hole pairs through competing with spin mixing, leading to the magneto-current, magneto-photoluminescence and magneto-photocurrent. Although magneto-absorption was reported for OMHPs at low temperature of 4.2 K and high magnetic field of 20 T in 1994, magnetic field effects from OMHPs at room temperature and low magnetic field (<1 T) were discovered recently.[96, 97] Accordingly, magnetic field effects provide unique and useful ways to explore the spin properties in OMHPs. Here, the spin-parallel and spin-antiparallel excitons, relaxing from the electron-hole pairs, are indicated by appearance of the magneto-current and magneto-photocurrent. In addition, tuning the intensity of carriers via changing the applied voltages, photoexcitation intensities and temperatures alters both magneto-current and magneto-photocurrent, indicating the interactions between free carriers and excitons.

6.2 Experiments

The OMHP ($CH_3NH_3PbI_{3-x}Cl_x$) precursor was prepared with an overall concentration of 30% by mixing methylammonium iodide (MAI) and lead chloride ($PbCl_2$) in anhydrous dimethylformamide (DMF) (Aldrich) with a mole ration of 3:1. The perovskite precursor was then stirred for 12 h at 60 °C and followed by filtration with a 0.45 μm PVDF filter. The TiO_x was prepared by adding a 0.026 M HCl (diluted in isopropyl alcohol) into a 0.46 M titanium isopropoxide solution (diluted in isopropyl alcohol) with stirring for 12 h and then filtered with a 0.2 μm PTFE filter. The TiO_x thin films were spin-cast with the thickness of about 35 nm on the pre-cleaned ITO substrates and then thermally annealed at 130 °C for 15 min. The perovskite ($CH_3NH_3PbI_{3-x}Cl_x$) was

spin-cast with the film thickness of 100 nm on the ITO/TiO_x substrates, followed by thermal annealing at 90 °C for 3 h. The MoO_3 was then thermal evaporated with the thickness of 10 nm. The gold (Au) electrodes were thermally deposited with film thicknesses of 100 nm. All the thermal evaporations were carried out under the vacuum of 7×10^{-7} Torr.

The devices were finally fabricated with the structure of ITO/TiO_x/$CH_3NH_3PbI_{3-x}Cl_x$/MoO_3/Au. The current–voltage (*I–V*) characteristics were measured by using Keithley 2400 source meter. The magneto-current and magneto-photocurrent were defined as $\mathrm{MC} = \frac{J_B - J_0}{J_0}$, where J_B and J_0 are the currents of the devices with and without magnetic field, respectively. The magneto-current and magneto-photocurrent signals were recorded by measuring the injection current and short-circuit current as a function of magnetic field. The photoexcitation was provided from 532 nm CW lasers.

6.3 Results and discussion

6.3.1 Magneto-current from $CH_3NH_3PbI_{3-x}Cl_x$

The current density versus voltage characteristics and the corresponding electroluminescence from the device with structure of ITO/TiO_x/$CH_3NH_3PbI_{3-x}Cl_x$/MoO_3/Au are presented in Figure 44 (a). A clear turn-on of injection is observed around 0.8 V. Additionally, the illumination turns on around 1.2 V, corresponding to the current density around 0.1 mA/cm^2. It directly validates the recombination between electrons and holes in this device, providing facilitated ways to study the charge recombination and dissociation in OMHPS. Figure 44 (b) shows the magneto-currents from this device at different injection current densities. It is obvious that the injection current becomes a function of magnetic field at room temperature, leading to a magneto-current. The magneto-current signal gradually increases and then becomes saturated around 200 mT. Additionally, the magneto-current signal decreases with the increasing injection current and ultimately changes into a negative value when the injection current reaches 1 mA/cm^2.

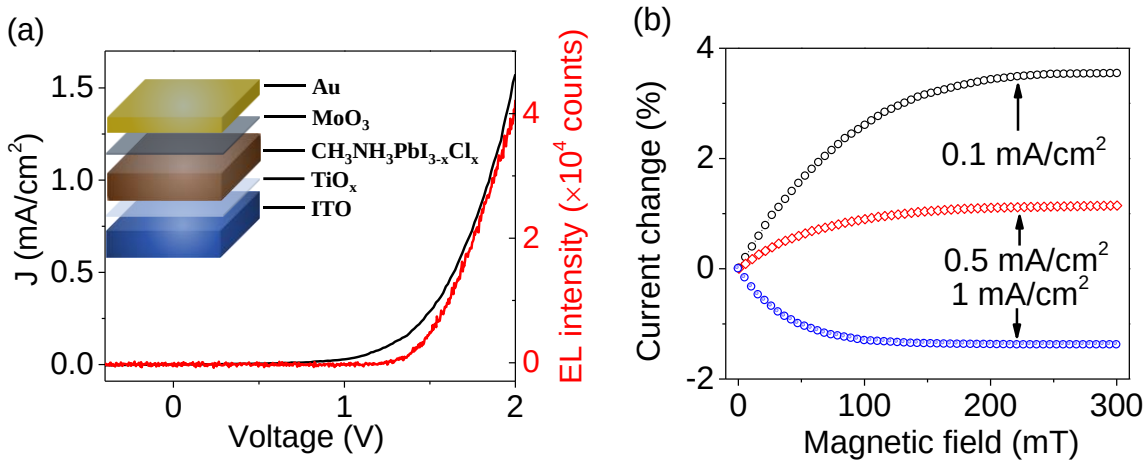

Figure 44 (a) Combined electroluminescence (Red) and current density (Black) versus voltage characteristics of the device with structure of ITO/TiO_x/$CH_3NH_3PbI_{3-x}Cl_x$/MoO_3/Au. Inset shows the device structure. (b) Magneto-current from this device with different injection current intensities.

Considering the fact that no spin-polarized charge injection occurs in the device due to the absence of ferromagnetic electrode, the magneto-current intrinsically originates from the $CH_3NH_3PbI_{3-x}Cl_x$. Researches indicate that electron-hole pairs with different spin configurations, either parallel or antiparallel, are formed when electrons and holes approaching each other during their transportation. Our former study indicated that an external magnetic field suppresses spin mixing between the antiparallel and parallel spin states in electron–hole pairs, increasing the electron-hole pairs with parallel spin configuration to generate a positive magneto-photocurrent.[97] In combination with the different lifetimes of electron-hole pairs with parallel or anti-parallel spin configurations, the electron-pairs in $CH_3NH_3PbI_{3-x}Cl_x$ provides a possibility to generate magneto-current through changing the ratio of spin-configuration by the external magnetic field. As the injection current is low, the density of electron-hole pairs is small. Consequently, the external magnetic field mainly affects the electron-hole pairs, leading to an increasing of pairs with parallel spin. Due to the long lifetime of these spin parallel electron-hole pairs, they have more opportunity to dissociate for current, generating a positive magneto-

current. Increasing the injection current, the density of electron-hole pairs becomes larger to generate the interaction between single carriers and electron-hole pairs. Experimental studies shown that the interaction between spin parallel electron-hole pairs and free carriers results in a negative magneto-current due to the scattering of free carriers.[103, 179, 180] Therefore, the decreasing magneto-current amplitude in this study indicates that the carriers and electron-hole pairs interact with each other in $CH_3NH_3PbI_{3-x}Cl_x$. Further increasing the injection current causes the interaction between carriers and electron-pairs to dominate the magneto-current, changing the sign of magneto-current from positive to negative. Consequently, the experiment results of magneto-current measurement indicate that the interaction between carriers and electron-hole pairs occurs in OMHPs when their densities are high enough.

6.3.2 Magneto-photocurrent from $CH_3NH_3PbI_{3-x}Cl_x$

Magneto-photocurrent is utilized to further confirm the interaction between carriers and electron-hole pairs in OMHPs. In general, free carriers are generated in OMHPs under the photovoltaic working condition due to the small binding energy.[68, 197, 203, 204] However, with increasing the photoexcitation intensity, the excitons are demonstrated to be generated. [198, 200, 205] Consequently, the interaction between exciton and free carriers happens, generating a negative magneto-photocurrent due to the scattering caused by interaction. Figure 45 (a) describes the magneto-photocurrent changing with photoexcitation intensity. Under the photoexcitation intensity of 400 mW/cm^2 which is much higher than the photovoltaic working function, the magneto-photocurrent is negative with the maximum value around -2.3% and tends to saturate around 250 mT. Increasing the photoexcitation intensity enhances the magneto-photocurrent signals with the amplitude changing from -2.3% at 400 mW/cm^2 to -3.00% at 800 mW/cm^2 and ultimately to -3.29% at 1600 mW/cm^2. It also indicates that increasing the photoexcitation intensity from 400 mW/cm^2 to 1600 mW/cm^2 leads the line-shape of magneto-photocurrents narrower with the half width at half maximum (HWHM) decreasing from 62.26 mT to 44.81 mT. In addition, the saturation field is found to decrease from around 260 mT to 150 mT. The negative values of magneto-photocurrent under higher photoexcitation intensities

directly illustrate the interaction between excitons and free carriers in OMHPs. More excitons normally introduce a stronger interaction between free carriers, leading to a larger scattering of free carriers with an outcome of larger negative magneto-photocurrent. Therefore, the increasing value of magneto-photocurrent proves that the density of excitons becomes larger as the photoexcitation becomes stronger. According to the higher intensity of excitons under stronger photoexcitation, the frequency of interaction between excitons and free carriers becomes higher, generating a quicker change of magneto-photocurrent which is demonstrated by the narrower line-shape and smaller saturation magnetic field. As a result, the change of magneto-photocurrent under higher photoexcitation further illustrates the interaction between excitons and free carriers in OMHPs.

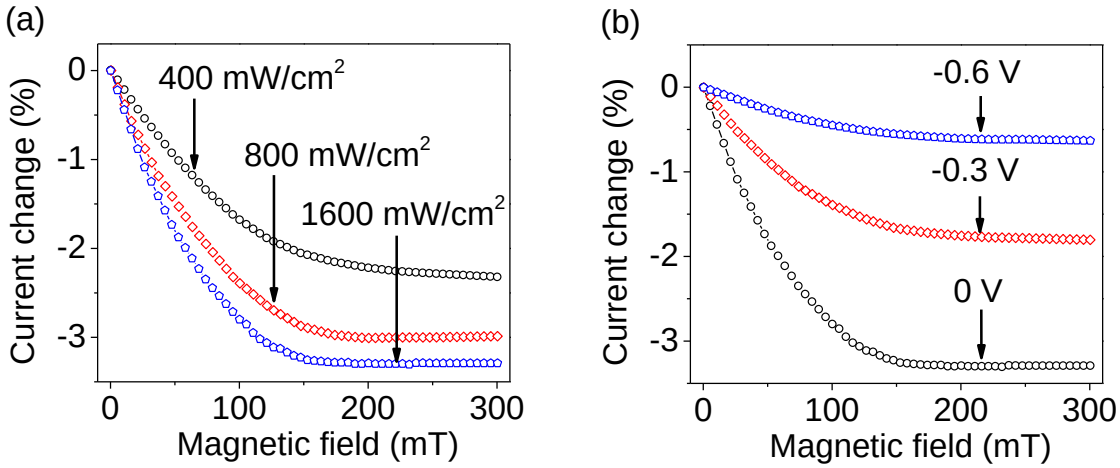

Figure 45 (a) Magneto-photocurrent from device with structure of ITO/TiO_x/$CH_3NH_3PbI_{3-x}Cl_x$/MoO_3/Au under different photoexcitation intensities. (b) Magneto-photocurrent from this device under 1600 mW/cm^2 with different bias voltages.

In order to additionally demonstrate the interaction between excitons and free carriers in OMHPs, different bias is applied to the devices under photoexcitation for tuning the density of free carriers to further influence the number of excitons. Figure 45 (b) indicates that adding a negative biases declines the value of magneto-photocurrent from -3.3% at 0 V to -1.8% at -0.3 V and -0.6% at -0.6 V under 1600 mW/cm^2. In general, adding the negative bias helps to extract the electrons and holes to the electrodes, reducing the

density of free carriers and excitons. Therefore, the interaction between excitons and free carriers reduces, generating a magneto-photocurrent with smaller amplitude. Since the interaction between excitons and free carriers becomes weak due to the less number of carriers and excitons, the frequency of the interaction becomes smaller and the rate of changing the photocurrent becomes slower. As a result, the line-shape and the saturation point of magneto-photocurrent becomes broader and larger respectively. As shown in Figure 2 (b), adding a negative bias leads the HWFM of the magneto-photocurrent to increase from 44.27 mT to 62.08 mT and the saturation point changes from around 150 mT to around 230 mT at 0 V and -0.6 V, respectively. In consequence, the change of magneto-photocurrent by adjusting the density of free carries through varying the applied bias proves the interaction between excitons and free carriers. In addition, this interaction is demonstrated to depend on the density of excitons and free carriers in the OMHPs.

6.3.3 Confinement effect on magneto-photocurrent from $CH_3NH_3PbI_{3-x}Cl_x$

The interaction between excitons and free carriers in OMHPs is further demonstrated by using interfacial confinement in the device. In general, the interfacial confinement can be used to unbalance the density of the injected electrons and holes, leading to spare charge carriers for interacting with the excitons. In this study, the hole transport layer of MoO_3 is removed to reduce the hole injection. As a result, an unbalanced concentration of electrons and holes are formed, leading to the formation of excitons with spare electrons. Figure 46 (a) indicates that magneto-current with the injection current of 0.5 mA/cm^2 turns from positive to negative after eliminating the MoO_3 layer. It is caused by the interaction between electrons and excitons with the scattering between them to reduce the mobility of carriers, transferring the magneto-current into negative. The magneto-photocurrent from the devices with and without hole transport layer MoO_3 is also studied as shown in Figure 46 (b). Under the photoexcitation of 800 mW/cm^2, removing the MoO_3 layer increases the magneto-photocurrent from the value of -3.00% to -4.67% at 300 mT. In general, the holes generated by photoexcitation becomes difficult to be extracted by the anode of Au without MoO_3 layer while the electrons are easy to be extracted by the cathode of ITO with TiO_x layer, leading to an unbalanced electrons and

holes with more holes left in the device. Consequently, interaction between excitons and holes occurs to scatter the free carriers, leading to an increase of the negative magneto-photocurrent. Therefore, the studies of magneto-current and magneto-photocurrent under the condition of interfacial confinement indicate that interaction between excitons and carriers, both electrons and holes, exists in OMHPs.

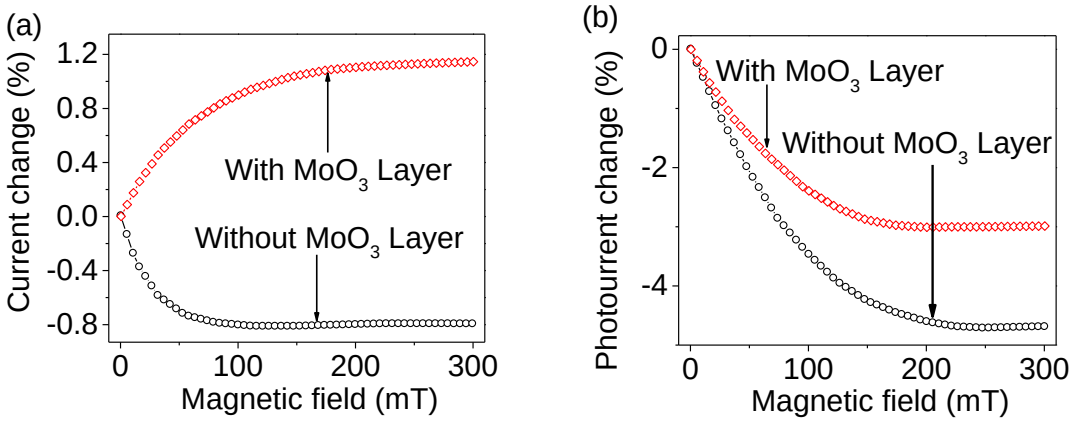

Figure 46 (a) Magneto-current from devices with and without MoO_3 at the injection current of 0.5 mA/cm^2. (b) magneto-photocurrent from devices with and without the MoO_3 layer under the photoexcitation of 800 mW/cm^2.

6.3.4 Temperature effect on magneto-photocurrent from $CH_3NH_3PbI_{3-x}Cl_x$

Former study shown that the density of exciton in OMHPs increases with decreasing temperature.[198] Consequently, changing the temperature provides another way to tune the interaction between excitons and free carriers in OMHPs. Figure 47 clearly indicates that the magneto-current from device with the injection current of 0.1 mA/cm^2 decreases and ultimately changed into negative with the temperature decreasing from 330 K to 77 K. It has been discussed that low density of excitons generates a positive magneto-current due to the suppression of spin-mixing caused by the external magnetic field while high density of excitons produces a negative magneto-current owe to the carrier scattering arising from the interaction between excitons and free carriers. Consequently, the decreasing value and the sign change of magneto-current with decreasing temperature

demonstrate the increasing density of excitons and the interaction between the excitons and free carriers.

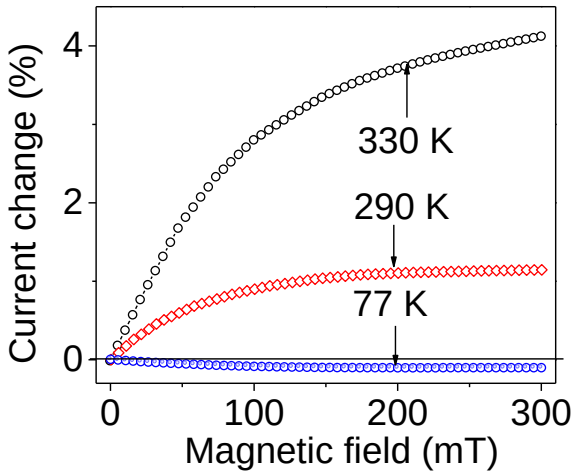

Figure 47 Magneto-current from device with structure of ITO/TiO_x/$CH_3NH_3PbI_{3-x}Cl_x$/MoO_3/Au with the injection current of 0.1 mA/cm^2 under different temperatures.

6.3.5 Discussion

Generally, free carriers dominate in OMHPs due to the small binding energy no matter they originate from photoexcitation or electric injection. Subsequently, the free electrons and holes can be captured to form electron-hole pairs due to the Coulomb interaction when they enter their mutual capture radius.[197, 201, 202] The recombined electron-hole pairs on one hand can relax into excitons with an ultimate outcome of photoluminescence through recombination.[202, 206] On the other hand, they can dissociate again into free carriers for the generation of current.[101] It is known that the electron-hole pairs has spin-parallel and spin-antiparallel configurations. Applying a magnetic field can decrease the number of spin-antiparallel states but increase the number of spin-parallel states through suppressing the spin mixing process between these two states. Eventually, the modification between different spin states in electron-hole pairs influence the exciton formation when the electron-hole pairs relaxing into excitons. Because the excitons with

antiparallel and parallel have high and low annihilation rate due to the Pauli Exclusion Principle, decreasing the number of electron-hole pair with antiparallel spin states enhances the formation of exciton with parallel spin states, which generates a positive magneto-current. Owing to the coexistence of exciton and free carriers in OMPHs by increasing the density of carriers, the exciton charge reaction is possible to take place, decreasing the mobility of free carriers due to the scattering. The external magnetic field increases the number of excitons with spin parallel states, which enhances the decrease of mobility of free carriers to generate a negative magneto-current. Therefore, the total magneto-current or magneto-photocurrent from OMHPs are constructed by the combination of positive signal from suppression of spin mixing and the negative signal from the exciton charge reaction. In the region of free carriers with low density, the suppression of spin mixing due to the external magnetic field generates a positive value as shown in our results. In the region of free carriers with high density due to the larger injection current, higher photoexcitation and low temperature, the exciton charge reaction produces the negative value. Additionally, studies have demonstrated the excitons turns to be more in very higher photoexcitation or low temperature.[198] It leads to a stronger exciton charge reaction, generating the negative signal of magneto-photocurrent and magneto-current as indicated in this study.

6.4 Conclusion

In conclusion, the magneto-current and magneto-photocurrent from OMHPs are studied in different conditions. Increasing the density of free carriers generates a decreasing in value of magneto-current, which ultimately changes the sign from positive to negative. The results indicate that exciton can be formed with the increasing density of free carriers, leading to the interaction between excitons and free carriers. This phenomenon is further proved by magneto-photocurrent under higher photoexcitation and adding different bias voltage and by magneto-current under low temperature, where both the excitons and free carriers coexist to interact with each other. The study here provides the information for balancing the ratio between excitons and free carriers in OMHPs to further improve the efficiency of photovoltaic devices.

CHAPTER 7

INTERACTION BETWEEN RASHBA PEROVSKITE AND FERROMAGNETIC METAL AT THE INTERFACE

This chapter reports magneto-dielectric phenomenon at the interface by combining ferromagnetic metal (Co) and Rashba perovskite ($CH_3NH_3PbI_{3-x}Cl_x$) based on thin-film design. The magneto-dielectric effect shows broader and narrower line-shapes when the magnetization is vertically and horizontally operated on the Co surface，generating an anisotropic magneto-electric coupling at the Co/$CH_3NH_3PbI_{3-x}Cl_x$ interface. It is proposed that the spins on ferromagnetic surface interact with the asymmetric orbitals on the Rashba perovskite surface based on two conditions: (i) the residual polarization from asymmetric orbital fields on Rashba perovskite surface and (ii) the interaction between the spins on the ferromagnetic surface and the asymmetric orbitals on the Rashba perovskite surface. Additionally, a frequency-tunable interaction between ferromagnetic surface and Rashba perovskite surface is demonstrated based on tuning the frequency in the process of magneto-dielectric measurement.

7.1 Introduction

Organo-metal halide perovskites have demonstrated multifunctional properties such as photovoltaic, light-emitting, lasing, and magneto-optic effects due to dual electrical polarization and semiconducting functions.[64, 65, 69, 74, 89, 183, 207-209] Recently, it has been theoretically shown that such multifunctional perovskites can demonstrate Rashba effects based on coexisted strong spin-orbital coupling and asymmetric polarizations.[210-213] Studies based on theoretical calculation show that the strong spin-orbital coupling in the organo-halide perovskites can generate the inversion symmetry-breaking field. This asymmetrical field can develop a Rashba effect by lifting the spin degeneracy with the spin splitting and the helical spin texture. In addition, the inversion symmetry-breaking field can also be produced by the polarization in the perovskites. Therefore, the polarization and the strong spin-orbital coupling can directly couple with each other through this inversion symmetry-breaking field in the Rashba perovskites. Consequently, we can expect asymmetric spin-orbital coupling on the Rashba perovskite surface ready for developing electric-magnetic coupling. On the other hand, a ferromagnetic surface possesses anisotropic spin polarizations at room temperature. Our early experimental studies have shown that the spin polarizations in ferromagnetic nanoparticles (γ-FeO_x) can interact with

nearby orbital field in organic molecules, generating spin-orbital interaction between ferromagnetic nanoparticles and organic molecules.[164] Furthermore, the spin valve studies have found that a spin interface can be formed at semiconducting/ferromagnetic interface through the hybridized interfacial states based on the interaction between the π electrons and d electrons, leading to a different density of states for spin splitting at the organic semiconducting/ferromagnetic interface.[214] Clearly, the spin interface provides further evidence that electric polarization and spin polarization can be coupled at semiconducting/ferromagnetic interface. Therefore, combing the Rashba surface with ferromagnetic surface presents opportunities to introduce the interaction between the asymmetric orbitals with anisotropic spin properties for developing electric-magnetic coupling at room temperature.

7.2 Experiments

The OMHP ($CH_3NH_3PbI_{3-x}Cl_x$) precursor was prepared with an overall concentration of 30% by mixing methylammonium iodide (MAI) and lead chloride ($PbCl_2$) in anhydrous dimethylformamide (DMF) (Aldrich) with a mole ration of 3:1. The perovskite precursor was then stirred for 12 h at 60 °C and followed by filtration with a 0.45 μm PVDF filter. The PMMA solution was prepared in chloroform solvent with a weight concentration of 20 mg/ml. The PMMA thin films were spin-cast with the thickness of about 100 nm on the pre-cleaned ITO substrates. The perovskite ($CH_3NH_3PbI_{3-x}Cl_x$) was spin-cast with the film thickness of 100 nm on the ITO/PMMA substrates, followed by thermal annealing at 90 °C for 3 h. The Co layer was then thermal evaporated with the thickness of 10 nm. The second layer of PMMA was spin-casted on the prepared perovskite layers. The gold (Au) electrodes was thermally deposited with film thicknesses of 100 nm. All the thermal evaporations were carried out under the vacuum of 7×10^{-7} Torr.

The capacitance was measured by an Agilent E4980A LCR meter under zero DC bias and 50 mV AC field. The magneto-dielectric (MFC) was defined as $\mathrm{MFC} = \frac{C_B - C}{C} = \frac{\Delta C}{C}$, where C_B and C are the capacitances of the capacitors with and without magnetic field, respectively. The PUND measurement was measured by using Precision LC. The M-H hysteresis were performed by using SQUID at room temperature.

7.3 Results and discussion

7.3.1 Interaction between Co and $CH_3NH_3PbI_{3-x}Cl_x$

The magneto-capacitance signals are measured at 1 KHZ from the device with the structure of ITO/PMMA/$CH_3NH_3PbI_{3-x}Cl_x$/Co/PMMA/Al as shown in Figure 48 (a). Clearly, inserting a thin layer of Co increases the capacitance with magnetic field, leading to a positive magneto-dielectric effect as shown in Figure 48 (b). In general, the magneto-dielectric effect originates either from (1) the bulk $CH_3NH_3PbI_{3-x}Cl_x$ or (2) the $CH_3NH_3PbI_{3-x}Cl_x$/Co interface. However, the bulk $CH_3NH_3PbI_{3-x}Cl_x$ shows a negligible magneto-dielectric signal as described in Figure 48 (b), indicating that the magneto-dielectric signal is formed at the interface between $CH_3NH_3PbI_{3-x}Cl_x$ and Co instead of the $CH_3NH_3PbI_{3-x}Cl_x$ bulk.

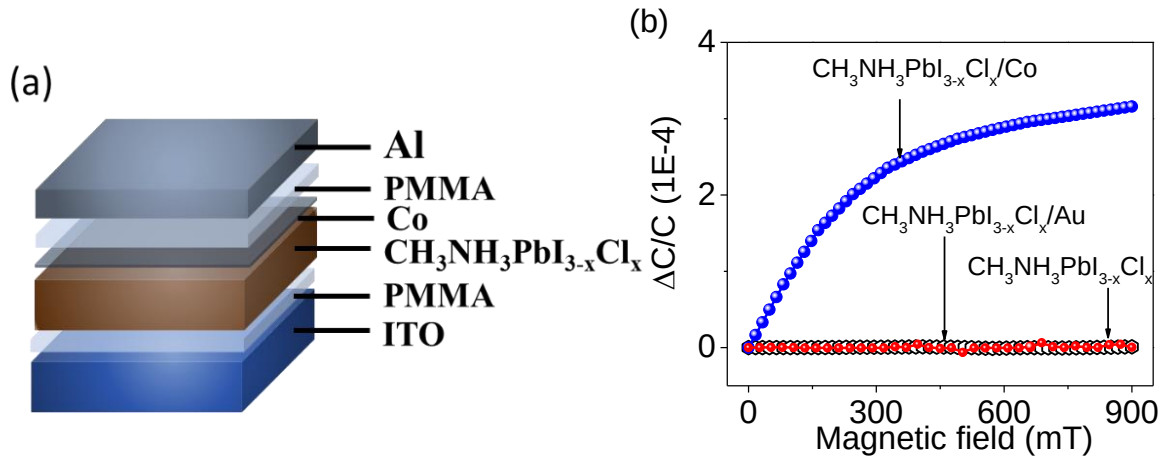

Figure 48 (a) The device structure used in this study. The PMMA layers are used for eliminating the effect of magneto-current. (b) Capacitance change from $CH_3NH_3PbI_{3-x}Cl_x$ coupled without (black) Co thin layer, with Co thin layer (blue) and Au thin layer (red) under the external magnetic field.

We should note that magneto-capacitance can be generated in two different channels: polarization-based magneto-capacitance and transport-based magneto-capacitance.[127, 128, 215] Former experimental and theoretical studies have indicated that the

polarization-based magneto-dielectric phenomenon dominates in the capacitance measurement.[118] Here, in order to further exclude the effect from the magneto-current in this study, active layers are sandwiched between the two layers of PMMA with the thickness around 100nm. Therefore, the transport-based magneto-capacitance is eliminated due to the insulating property of PMMA. Additionally, coupling $CH_3NH_3PbI_{3-x}Cl_x$ with Au presents a negligible magneto-dielectric signal as shown in Figure 48 (b). This phenomenon indicates that the spin polarization on Co surface is a prerequisite for realizing the magneto-dielectric effect at the interface between Co and $CH_3NH_3PbI_{3-x}Cl_x$ surfaces.

7.3.2 Anisotropy of interaction between Co and $CH_3NH_3PbI_{3-x}Cl_x$

We further study the magneto-dielectric effect at the interface with the angle-dependent characterization as shown in Figure 49 (a). Swiping the external magnetic field from in-plane to out-of-plane direction increases the amplitude of magneto-dielectric signal from 4.92E-4 to 6.34E-4 by 29% at 900 mT. At the same time, the HWHM (half width at the half maximum) of the magneto-dielectric curve increases from 120 mT to 303 mT, leading to a broader line-shape with increasing magnetic field. The results demonstrate that the magneto-dielectric effect at the $CH_3NH_3PbI_{3-x}Cl_x$/Co interface is an anisotropic phenomenon. The magnetic M-H curves in Figure 49 (b) indicate that the coercivity of the magnetic hysteresis increases from the value of 17 mT to 30 mT after changing the direction of the external magnetic field from in-plane to out-of-plane. Furthermore, the spin polarization on Co surface changes from a soft ferromagnetic characterization to a hard ferromagnetic characterization as the magnetic field changes from in-plane to out-of-plane direction. This reveals that the anisotropic magneto-dielectric effect at the interface is related to the magnetic anisotropy of Co surface. Additionally, theoretical studies have shown that the organo-metal halide perovskites can exhibit ferroelectric Rashba effects when the spin splitting and spin helicity are generated by the strong spin-orbital coupling and electric polarization in asymmetric structures. Former experimental study illustrates that the angle-dependent Rashba effect at the graphene/Ni interface is generated through interaction between the spin-polarized electrons and the gradient electric field, which is demonstrated by the angle-resolved photoelectron spectroscopy.[216] This phenomenon

indicates a possibility for the spin-orbital interaction at the interface between ferromagnetic metal Co and Rahsba perovskite $CH_3NH_3PbI_{3-x}Cl_x$ in this study. Here, the interaction between spins on the Co surface with the asymmetric orbitals on the $CH_3NH_3PbI_{3-x}Cl_x$ provides a way for generating the magneto-dielectric effect through spin-orbital interaction at the interface. In general, the Rashba effect can be expressed by the Rashba Hamiltonian $H_R = \alpha_R(\boldsymbol{\sigma} \times \boldsymbol{p}) \cdot \hat{\boldsymbol{z}}$, where σ is the Pauli matrix vector, $\boldsymbol{p}$ is the momentum, $\hat{\boldsymbol{z}}$ is the direction of electric field and α_R is the Rashba coefficient depending on the spin-orbital interaction strength. When the spin polarization on the Co surface changes from the soft to the hard direction by swiping the external magnetic field from in-plane to out-of-plane direction, the spin-orbital interaction between the spins on Co surface and asymmetric orbitals on $CH_3NH_3PbI_{3-x}Cl_x$ surface becomes weak and strong respectively. As a consequence, the change of the electric polarization on $CH_3NH_3PbI_{3-x}Cl_x$ surface based on this spin-orbital interaction are small and large respectively, leading to an angle-dependent magneto-dielectric effect in the device with structure of ITO/PMMA/$CH_3NH_3PbI_{3-x}Cl_x$/Co/PMMA/Al.

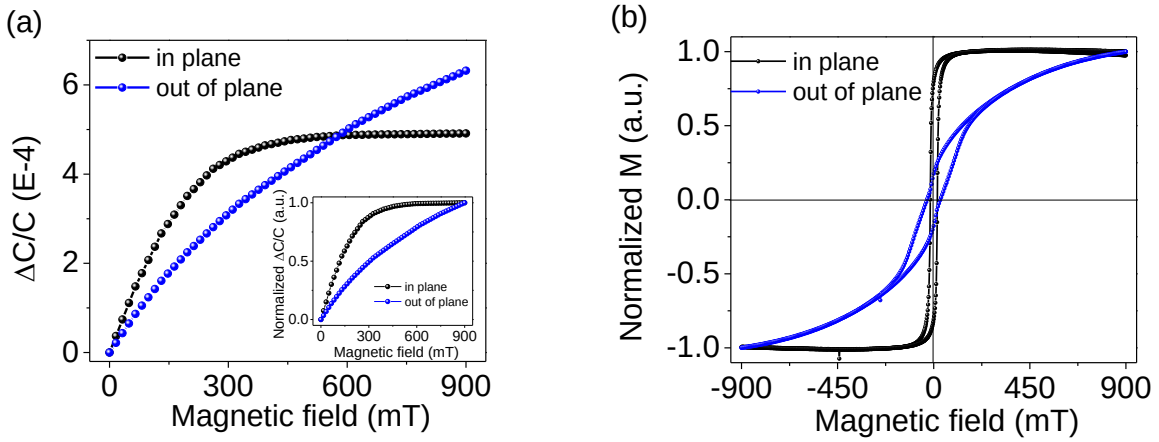

Figure 49 (a) Capacitance change from the device under the external magnetic field with in pane and out of plane directions different directions. Inset shows the normalized magneto-dielectric signals. (b) Normalized magnetic M-H hysteresis measured under the magnetic field with in pane and out of plane directions.

7.3.3 Effect of interaction between Co and $CH_3NH_3PbI_{3-x}Cl_x$

Now we discuss the effect of the spin-orbital interaction at $CH_3NH_3PbI_{3-x}Cl_x$/Co interface on the residual polarization of the $CH_3NH_3PbI_{3-x}Cl_x$ surface and the spin polarization of the Co surface through interface engineering. Three different devices with the active layers of pristine $CH_3NH_3PbI_{3-x}Cl_x$, spin-casting the $CH_3NH_3PbI_{3-x}Cl_x$ layer on Co surface and depositing Co on $CH_3NH_3PbI_{3-x}Cl_x$ surface are used to tune the spin-orbital interaction by changing the interaction area based on penetration. Depositing Co on $CH_3NH_3PbI_{3-x}Cl_x$ surface generates a large interaction area for the spin-orbital interaction at the $CH_3NH_3PbI_{3-x}Cl_x$/Co interface due to the perennation of Co, leading to a strong spin-orbital interaction.

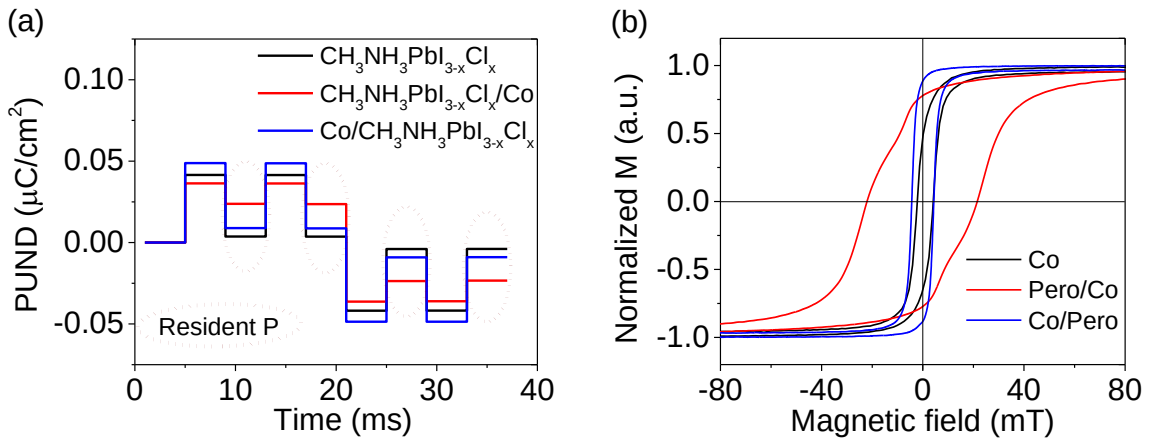

Figure 50 (a) PUND signals from pristine $CH_3NH_3PbI_{3-x}Cl_x$ and $CH_3NH_3PbI_{3-x}Cl_x$ combining with Co on different sides. (b) Magnetic M-H hysteresis from pristine Co layer, Co layer on top of $CH_3NH_3PbI_{3-x}Cl_x$ and Co underneath $CH_3NH_3PbI_{3-x}Cl_x$.

The positive-up/negative-down (PUND) measurements from these devices are shown in Figure 50 (a). It is known that the PUND measurement can be used to demonstrate the residual polarization after the application of positive and negative pulses. Here, the PUND measurement is carried out with a triangle pulse width of 1 ms and delay time of 1000 ms, leading to low frequency and repetition rate to ensure the residual polarization from the Rashba perovskite surface. Figure 50 (a) indicates that the pristine $CH_3NH_3PbI_{3-}$

$_xCl_x$ presents a residual electric polarization with the value of 0.004 μC/cm^2, demonstrating a spontaneous polarization on the $CH_3NH_3PbI_{3-x}Cl_x$ surface. We should also note that the residual electric polarization increases to 0.008 μC/cm^2 when introducing the spin-orbital interaction by spin-casting the $CH_3NH_3PbI_{3-x}Cl_x$ layer on Co surface. In addition, the electric polarization further increases to 0.023 μC/cm^2 when increasing the spin-orbital interaction by improving the interaction area through depositing the Co layer on $CH_3NH_3PbI_{3-x}Cl_x$ surface. Consequently, the strong spin-orbital interaction can enhance the surface polarization of the Rashba perovskite $CH_3NH_3PbI_{3-x}Cl_x$, generating a large residual polarization. On the other hand, the spin polarization on Co surface can also be changed by the spin-orbital interaction at the $CH_3NH_3PbI_{3-x}Cl_x$/Co interface as shown in Figure 50 (b). The coercivity of Co increases from 2.0 mT to 4.5 mT after introducing the spin-orbital interaction with spin-casing $CH_3NH_3PbI_{3-x}Cl_x$ on Co surface. It further increases to 22.3 mT after enhancing the spin-orbital interaction by depositing Co on $CH_3NH_3PbI_{3-x}Cl_x$ surface. Therefore, the increased coercivity of Co illustrates that the spin-orbital interaction at the $CH_3NH_3PbI_{3-x}Cl_x$/Co interface can influence the spin polarization on Co surface. Consequently, the interface engineering can modify the residual polarization on $CH_3NH_3PbI_{3-x}Cl_x$ surface and the spin polarization on Co surface through the spin-orbital interaction by simply changing the interaction area.

7.3.4 Principle for interaction between Co and $CH_3NH_3PbI_{3-x}Cl_x$

In principle, the magneto-dielectric effect at the $CH_3NH_3PbI_{3-x}Cl_x$/Co interface can be realized by satisfying two conditions: (1) the residual polarization on Rashba perovskite surface from the asymmetric orbitals and (2) the interaction between the spins on the ferromagnetic surface and the asymmetric orbitals on the Rashba perovskite surface. The PUND measurement demonstrates the residual polarization on the Rashba perovskite surface. The M-H hysteresis clearly indicates the spin polarization from the ferromagnetic Co film. Based on the structure of ABX_3 with A as the organic cations, B as the heavy metals and X as the halide elements, theoretical calculations indicate that the orbital interaction between B and X in the Rashba perovskites can be modified by the structural modification in the inorganic frame BX_6 and the positional distortion from centro-

symmetry sites.[217] Most perovskites with ABX_3 structure show spontaneous electric polarization due to the breaking of the centro-symmetry as the B cation shifts away from the center of BX_6 octahedron. Especially in organic/inorganic hybrid halide perovskites, this phenomenon is pronounced due to the absence of an inversion center in the crystalline lattice based on the asymmetric organic cations.[85] As a result, the electric polarization in Rashba perovskite is associated with the asymmetric orbitals from BX_6 octahedron. Specifically, the two-dimensional structural inversion asymmetry at the perovskite surface provides stronger asymmetric orbitals than that in the bulk. This asymmetry provides a possibility for generating the spin-orbital interaction between the spins on the ferromagnetic Co surface and the asymmetric orbitals on the Rashba perovskite surface at the $CH_3NH_3PbI_{3-x}Cl_x$/Co interface. Under the influence of an external magnetic field, aligning spins on Co surface increases the interaction between spins and the asymmetric orbitals, leading to an increase of the polarization at the Rashba perovskite surface to generate the positive magneto-dielectric signal as indicated in Figure 48 (b). This interaction between spins and the asymmetric orbitals at the interface is further proved by the anisotropic magneto-dielectric phenomenon in Figure 49 (a). The anisotropic M-H hysteresis in Figure 49 (b) indicates that spin polarization on Co surface can be easily and difficultly aligned by the external magnetic field with in-plane and out-of-plane direction respectively. On one hand, the spin polarization alignment on Co with difficult process decreases the rate of the spin-orbital interaction, generating a broader line-shape of magneto-dielectric curve. On the other hand, this process introduces more interactions between the spins and the asymmetric orbitals, increasing the value of the magneto-dielectric signal. Consequently, the electric polarization on Rashba perovskite surface can be changed by the spin polarization on ferromagnetic metal surface through the spin-orbital interaction at the interface.

7.3.5 Confirmation of interaction between Co and $CH_3NH_3PbI_{3-x}Cl_x$

In order to further confirm the spin-orbital interaction at the $CH_3NH_3PbI_{3-x}Cl_x$/Co interface, we study the magneto-dielectric effect from devices with different spins and asymmetric orbitals by changing the active interaction area and the concentration of iodine

respectively. In Figure 51 (a), increasing the spin-orbital interaction through increasing the interaction area by depositing Co on $CH_3NH_3PbI_{3-x}Cl_x$ surface instead of spin-casting $CH_3NH_3PbI_{3-x}Cl_x$ on Co surface increases the HWFM of the magneto-dielectric curves from 51 mT to 126 mT, generating a broader line-shape. In addition, the amplitude of magneto-dielectric signal at 900 mT also increases from 0.63E-4 to 3.26E-4 by a factor of 5. All these results indicate that the interaction between the spin polarization and the asymmetric orbitals becomes stronger when increasing the spin polarization by depositing Co on $CH_3NH_3PbI_{3-x}Cl_x$ surface. On the other hand, the amplitude of the magneto-dielectric signal is increased from 0.67E-4 to 6.30E-4 by a factor of 9 with increasing the concentration of iodine as shown in Figure 51 (b), indicating a larger spin-orbital interaction at the interface. In general, the asymmetric orbitals in Rashba perovskite $CH_3NH_3PbI_{3-x}Cl_x$ originate from the inorganic octahedral constructed by Pb and halide elements.[218, 219] Increasing the concentration of I enhances the asymmetric orbital in Rashba perovskite, leading to an improvement of the interaction between spins and the asymmetric orbitals to develop a larger magneto-dielectric signal. The experiment results validate the fact that the magneto-dielectric effect at the Co/$CH_3NH_3PbI_{3-x}Cl_x$ interface originates from the interaction between spins on Co surface and asymmetric orbitals on Rashba perovskite surface.

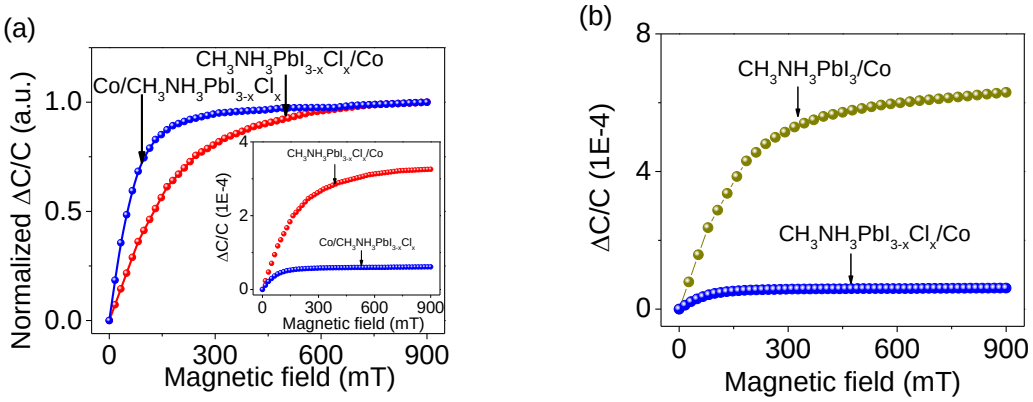

Figure 51 (a) Magneto-dielectric from devices with Co on opposite sides of $CH_3NH_3PbI_{3-x}Cl_x$. Inset: normalized magneto-dielectric signals. (b) Magneto-dielectric from devices with different concentration of Cl in $CH_3NH_3PbI_{3-x}Cl_x$.

7.3.6 Dynamic properties of interaction between Co and $CH_3NH_3PbI_{3-x}Cl_x$

Now we discuss the dynamic properties of the spin-orbital interaction at the Co/$CH_3NH_3PbI_{3-x}Cl_x$ interface by changing the frequency of AC bias during the capacitance measurement. Increasing the frequency clearly narrows the line-shape of magneto-dielectric signals. The HWFM decreases from 137.23 mT at 1 kHz to 118.09 mT at 10 kHz and ultimately to 100.10 mT at 300 kHz as shown in Figure 52 (a). Meanwhile, increasing the frequency also decreases the amplitude of the magneto-dielectric signal from 3.36E-4 to 2.82E-4 and ultimately to 1.09E-4. These results indicate a stronger magneto-dielectric effect at the interface under the lower AC frequency, which originates from the larger spin-orbital interaction. Due to the slow response of electric dipoles at high AC frequencies, higher AC frequency limits the dipole response and decreases the capacitance as shown in Figure 52 (b).

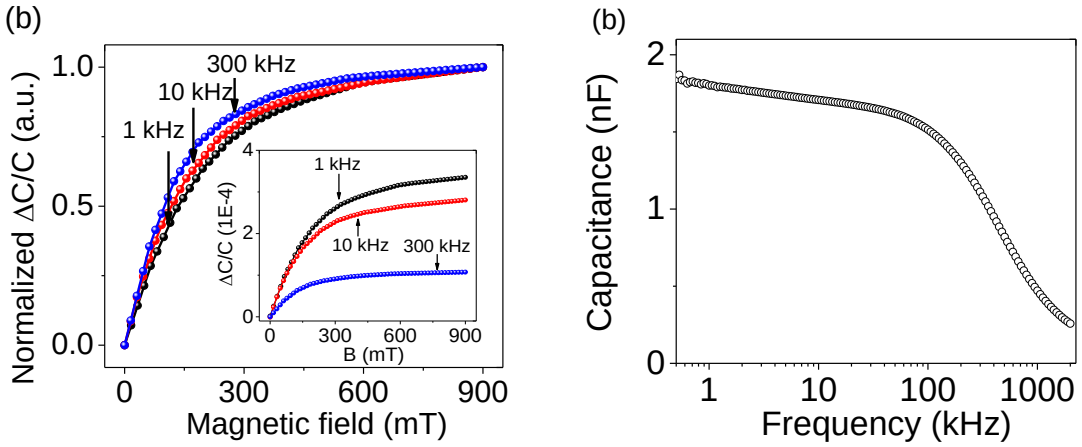

Figure 52 (a) Normalized magneto-dielectric from the device under different frequencies. Inset shows the absolute magneto-dielectric value from the device under different frequencies. (b) Capacitance from the device changing with frequency of the AC bias.

The capacitance from the device with Co deposited on $CH_3NH_3PbI_{3-x}Cl_x$ surface decreases from 1.81 nF to 0.25 nF as the frequency of AC bias increasing from 1 kHz to 2 MHz, leading to a stronger and weaker effective electric potential at the $CH_3NH_3PbI_{3-x}Cl_x$ surface to influence the asymmetric orbitals through Rasbha interaction. Consequently, the

interaction between spins from the ferromagnetic metal and asymmetric orbitals from Rashba perovskite can be strengthened and weakened at the low and high frequencies, generating larger and smaller magneto-dielectric signals. This frequency-dependent phenomenon provides a new way for tuning magneto-electronic coupling.

7.4 Conclusion

In summary, we demonstrate the spin-orbital interaction at the interface between ferromagnetic Co surface and Rashba perovskite $CH_3NH_3PbI_{3-x}Cl_x$ surface based on the measurement of magneto-dielectric effect. This interaction originates from the interaction between spins on Co surface and the asymmetric orbital on the $CH_3NH_3PbI_{3-x}Cl_x$ surface. It is confirmed by tuning the spins on the Co surface through changing the external magnetic field from in-plane to out-of-plane direction. On one hand, operating spins on Co surface by changing the interaction area based on penetration generates a different spin-orbital interaction. On the other hand, tuning the asymmetry orbitals through varying the concentration of iodine also affects the spin-orbital interaction. These two results further demonstrate the spin-orbital interaction at the interface between Co surface and $CH_3NH_3PbI_{3-x}Cl_x$ surface. Furthermore, the frequency-dependent spin-orbital interaction at the interface is also studied with an outcome of decreasing the spin-orbital interaction as increasing the frequency. Our study provides a possible method to use the Rashba perovskite in spintronics based on the magneto-electronic effect in future.

CHAPTER 8
CONCLUSION

It has been found that charge-transfer states are important to determine the electronic and magnetic properties in organic semiconducting materials. However, little work has been done to explore the interaction between them. Therefore, we use magnetic field effect as a tool to study the interaction between charge-transfer states in this thesis.

We first investigated the interaction between intermolecular charge-transfer states based on the P3HT:PCBM bulk heterojunction solar cell by using magneto-photocurrent and magneto-capacitance measurements. The value increasing and line-shape narrowing of magneto-photocurrent signals with increasing photoexcitation intensity is ascribed to the decreasing spin-exchange energy in individual intermolecular charge-transfer state caused by the interaction between intermolecular charge-transfer states at the P3HT/PCBM interface. This interaction is further confirmed by the similar change of magneto-capacitance signals. Furthermore, three possible mechanisms: the long-range Coulomb interaction, the medium-range spin-orbital interaction and short-range spin interaction are proposed to explain the interaction. This interaction on one hand illustrates the fundamental physics on changing the spin-exchange interaction in single intermolecular charge-transfer states. On the other hand, it provides researchers and engineers with information on developing new devices for applications in controlling spin-exchange energy.

Getting the information on the interaction between intermolecular charge-transfer states attracts our attention on combining the charge-transfer states (π electrons) with d electrons for spintronics application. In order to study the interaction between π electrons in organic semiconducting materials and d electrons in ferromagnetic nanoparticles for realizing the magneto-electronic coupling, we explored the interaction between intramolecular charge-transfer states and d electrons in the magneto-organic nanocomposites. Based on the magneto-capacitance measurement, we found the interaction between intramolecular charge-transfer states and d electrons is greatly enhanced under photoexcitation. Changing the distance between intramolecular charge-transfer states and d electrons and varying the concentrations of intramolecular charge-transfer states and d electrons indicate that the interaction is controlled by the competition of Coulomb interaction and spin-spin interaction. The interaction between π electrons and

d electrons leads to an opportunity for developing the photo-assisted magnetization in nanocomposite at room temperature.

Studies on the π-d electron coupling leads to an interest on studying the interaction between organic semiconducting materials and ferromagnetic metals. Lots of studies have been focused on the spin properties at the interface between organic semiconducting materials and ferromagnetic metals for improving the spin injection and spin filtering. Here, we considered the interaction between magnetized charge-transfer states at the interface of TPD/Co and the photo-generated charge-transfer states in the TPD:BBOT bulk under photoexcitation. The enhanced magneto-capacitance signal after combing magnetized charge-transfer states and photo-generated charge-transfer states reveals the interaction between these two kinds of charge-transfer states. Furthermore, the interaction between magnetized charge-transfer states and photo-generated charge-transfer states is demonstrated to be photo-changeable and distance-tunable, providing us plenty of information for improving the spin properties at the interface between organic semiconducting materials and ferromagnetic metals. The photo-controllable spin properties at the interface indicates a possibility for realizing the photo-enhanced spin injection, which would be an improvement on spin applications in flexible devices.

We also use the magnetic field effect to study the interaction between excitons and free charge carriers in organo-metal halide perovskite. The sign change of magneto-current from positive to negative indicates the interaction between excitons and free charge carriers in organo-metal halide perovskites. The interaction is further demonstrated by the decreasing of magneto-photocurrent under high photoexcitation intensities where both excitons and free charge carriers coexists. In addition, changing the free charge carrier confinement at the interface also proves the interaction. This study provides further fundamental information for using organo-metal halide perovskites in applications such as photovoltaic cells and light emitting diodes. It can be used in controlling the photoexcitation intensities, injection currents, temperature and device structures for facilitating the efficiencies of devices.

Further information about the magneto-electronic coupling at the interface between Rashba perovskite and ferromagnetic metal is studied through magneto-capacitance

measurement. The positive magneto-capacitance indicates the spin-orbital interaction at the interface due to the spins on ferromagnetic metal and asymmetric orbitals on Rashba perovskite surface. Additionally, this interaction is proved to be anisotropic by the anisotropic magneto-capacitance signals through swiping the direction of the external magnetic field. The spin-orbital interaction at the interface is further consolidated by changing the spins and orbitals based on changing the interaction area and concentration of iodide respectively. The magneto-electronic interaction at the interface is demonstrated to be frequency-tunable. This magneto-electronic coupling provides an experiment evidence for proving the Rashba properties in organo-metal halide perovskites. Furthermore, the coupling illustrates a possibility for realizing the multiferroic applications in data storage based on the organo-metal halide perovskites. This interaction also suggests the possibilities of controlling the coupling by using photoexcitation, which can further improve the multiferroic applications.

As a conclusion, our studies indicates three mechanisms: long-range Coulomb interaction, medium-range spin-orbital interaction and short-range spin-spin interaction in illustrating the fundamental physics in organic semiconducting materials. The interactions between different kinds of charge-transfer states presents possibility to further extend the applications of organic semiconducting materials in photovoltaic cells, light-emitting diodes and flexible spintronics. This study also provides basic information for researchers in controlling the interactions with other parameters such as light, electric field and magnetic field. The second part of our works on organo-metal halide perovskites on one hand provide the experiment evident on both the interaction between excitons and free charge carriers and the Rashba properties. On the other hand, the studies show a platform for realizing the magneto-electronic applications by using organo-metal halide perovskites, which opens new directions for future study by using this material.

All in all, this thesis provides both the fundamental information and future possibilities in magneto-electronic-optical application.

REFERENCES

[1] H. Shirakawa, E. J. Louis, A. G. MacDiarmid, C. K. Chiang, A. J. Heeger, Journal of the Chemical Society, Chemical Communications 1977, 578.

[2] S. R. Forrest, Nature 2004, 428, 911.

[3] H. T. Yi, M. M. Payne, J. E. Anthony, V. Podzorov, Nature communications 2012, 3, 1259.

[4] Y. H. Zhou, C. Fuentes-Hernandez, T. M. Khan, J. C. Liu, J. Hsu, J. W. Shim, A. Dindar, J. P. Youngblood, R. J. Moon, B. Kippelen, Sci Rep-Uk 2013, 3.

[5] M. Pope, C. E. Swenberg, Electronic processes in organic crystals and polymers, Oxford University Press on Demand, 1999.

[6] R. H. Friend, R. W. Gymer, A. B. Holmes, J. H. Burroughes, R. N. Marks, C. Taliani, D. D. C. Bradley, D. A. Dos Santos, J. L. Bredas, M. Logdlund, W. R. Salaneck, Nature 1999, 397, 121.

[7] H. Bässler, phys. status solidi b 1993, 175, 15.

[8] v. S. Mensfoort, Technische Universiteit Eindhoven, 2009.

[9] Z. H. Xiong, D. Wu, Z. V. Vardeny, J. Shi, Nature 2004, 427, 821.

[10] T. Santos, J. Lee, P. Migdal, I. Lekshmi, B. Satpati, J. Moodera, Physical review letters 2007, 98, 016601.

[11] Ö. Mermer, G. Veeraraghavan, T. Francis, Y. Sheng, D. Nguyen, M. Wohlgenannt, A. Köhler, M. Al-Suti, M. Khan, Physical Review B 2005, 72, 205202.

[12] L. He, M. Li, A. Urbas, B. Hu, Physical Review B 2014, 89, 155304.

[13] H. Zang, J. Wang, M. Li, L. He, Z. Liu, D. Zhang, B. Hu, The Journal of Physical Chemistry B 2013, 117, 14136.

[14] H. Zang, L. Yan, M. Li, L. He, Z. Gai, I. Ivanov, M. Wang, L. Chiang, A. Urbas, B. Hu, Sci Rep-Uk 2013, 3.

[15] T. D. Nguyen, G. Hukic-Markosian, F. Wang, L. Wojcik, X.-G. Li, E. Ehrenfreund, Z. V. Vardeny, Nature materials 2010, 9, 345.

[16] T. Nguyen, Y. Sheng, J. Rybicki, M. Wohlgenannt, Physical Review B 2008, 77, 235209.

[17] F. Bloom, M. Kemerink, W. Wagemans, B. Koopmans, Physical review letters 2009, 103, 066601.

[18] S. Majumdar, H. S. Majumdar, H. Aarnio, R. Österbacka, physica status solidi (RRL)-Rapid Research Letters 2009, 3, 242.

[19] F. Wang, H. Bässler, Z. V. Vardeny, Physical review letters 2008, 101, 236805.

[20] J. Bergeson, V. Prigodin, D. Lincoln, A. Epstein, Physical review letters 2008, 100, 067201.

[21] B. Hu, Y. Wu, Nature materials 2007, 6, 985.

[22] F. Bloom, W. Wagemans, M. Kemerink, B. Koopmans, Physical review letters 2007, 99, 257201.

[23] P. Bobbert, T. Nguyen, F. Van Oost, v. B. Koopmans, M. Wohlgenannt, Physical Review Letters 2007, 99, 216801.

[24] Y. Wu, Z. Xu, B. Hu, J. Howe, Physical Review B 2007, 75, 035214.

[25] P. Desai, P. Shakya, T. Kreouzis, W. Gillin, N. Morley, M. Gibbs, Physical Review B 2007, 75, 094423.

[26] V. Prigodin, J. Bergeson, D. Lincoln, A. Epstein, Synthetic Metals 2006, 156, 757.

[27] C. Yang, E. Ehrenfreund, Z. Vardeny, Physical review letters 2007, 99, 157401.

[28] D. McCamey, H. Seipel, S.-Y. Paik, M. Walter, N. Borys, J. Lupton, C. Boehme, Nature Materials 2008, 7, 723.

[29] V. Dediu, M. Murgia, F. Matacotta, C. Taliani, S. Barbanera, Solid State Communications 2002, 122, 181.

[30] V. Dediu, L. Hueso, I. Bergenti, A. Riminucci, F. Borgatti, P. Graziosi, C. Newby, F. Casoli, M. De Jong, C. Taliani, Physical Review B 2008, 78, 115203.

[31] N. Morley, A. Rao, D. Dhandapani, M. Gibbs, M. Grell, T. Richardson, Journal of Applied Physics 2008, 103, 07F306.

[32] F. Wang, C. Yang, Z. V. Vardeny, X. Li, Physical Review B 2007, 75, 245324.

[33] H. Vinzelberg, J. Schumann, D. Elefant, R. Gangineni, J. Thomas, B. Büchner, Journal of Applied Physics 2008, 103, 093720.

[34] V. A. Dediu, L. E. Hueso, I. Bergenti, C. Taliani, Nature materials 2009, 8, 707.

[35] J. Schoonus, P. Lumens, W. Wagemans, J. Kohlhepp, P. Bobbert, H. Swagten, B. Koopmans, Physical review letters 2009, 103, 146601.

[36] J. Shim, K. Raman, Y. Park, T. Santos, G. Miao, B. Satpati, J. Moodera, Physical review letters 2008, 100, 226603.

[37] G. Szulczewski, H. Tokuc, K. Oguz, J. Coey, Applied Physics Letters 2009, 95, 202506.

[38] J.-W. Yoo, H. Jang, V. Prigodin, C. Kao, C. Eom, A. Epstein, Synthetic Metals 2010, 160, 216.

[39] H. Schwob, D. Williams, "Magnetic-field modulation of electroluminescence in anthracene and tetracene", presented at BULLETIN OF THE AMERICAN PHYSICAL SOCIETY, 1972.

[40] R. Merrifield, The Journal of Chemical Physics 1968, 48, 4318.

[41] V. Ern, R. Merrifield, Physical Review Letters 1968, 21, 609.

[42] F. Bloom, W. Wagemans, B. Koopmans, Journal of Applied Physics 2008, 103, 7F320.

[43] P. Desai, P. Shakya, T. Kreouzis, W. Gillin, Journal of Applied Physics 2007, 102, 073710.

[44] P. Shakya, P. Desai, T. Kreouzis, W. Gillin, Journal of Applied Physics 2008, 103, 3706.

[45] L. Xin, C. Li, F. Li, S. Liu, B. Hu, Applied Physics Letters 2009, 95, 123306.

[46] J. Kalinowski, M. Cocchi, D. Virgili, P. Di Marco, V. Fattori, Chemical Physics Letters 2003, 380, 710.

[47] E. Frankevich, A. Lymarev, I. Sokolik, F. Karasz, S. Blumstengel, R. Baughman, H. Hörhold, Physical Review B 1992, 46, 9320.

[48] F. Ito, T. Ikoma, K. Akiyama, A. Watanabe, S. Tero-Kubota, The Journal of Physical Chemistry B 2005, 109, 8707.

[49] S. Karabunarliev, E. R. Bittner, Physical review letters 2003, 90, 057402.

[50] K. Tandon, S. Ramasesha, S. Mazumdar, Physical Review B 2003, 67, 045109.

[51] M. Wohlgenannt, X. M. Jiang, Z. V. Vardeny, R. Janssen, Physical review letters 2002, 88, 197401.

[52] H. J. Werner, Z. Schulten, K. Schulten, The Journal of Chemical Physics 1977, 67, 646.

[53] Z. Schulten, K. Schulten, The Journal of Chemical Physics 1977, 66, 4616.

[54] K. Schulten, H. Staerk, A. Weller, H.-J. Werner, B. Nickel, Zeitschrift für Physikalische Chemie 1976, 101, 371.

[55] B. Brocklehurst, Univ. of Sheffield, Eng., 1969.

[56] W. W. Wagemans, Technische Universiteit Eindhoven, 2010.

[57] P. Desai, P. Shakya, T. Kreouzis, W. Gillin, Physical Review B 2007, 76, 235202.

[58] I. V. Khudyakov, Y. A. Serebrennikov, N. J. Turro, Chemical reviews 1993, 93, 537.

[59] V. Dyakonov, G. Zoriniants, M. Scharber, C. Brabec, R. Janssen, J. Hummelen, N. Sariciftci, Physical Review B 1999, 59, 8019.

[60] J. De Ceuster, E. Goovaerts, A. Bouwen, J. Hummelen, V. Dyakonov, Physical Review B 2001, 64, 195206.

[61] G. E. Eperon, S. D. Stranks, C. Menelaou, M. B. Johnston, L. M. Herz, H. J. Snaith, Energy & Environmental Science 2014, 7, 982.

[62] T. M. Koh, K. Fu, Y. Fang, S. Chen, T. Sum, N. Mathews, S. G. Mhaisalkar, P. P. Boix, T. Baikie, The Journal of Physical Chemistry C 2013, 118, 16458.

[63] N. Pellet, P. Gao, G. Gregori, T. Y. Yang, M. K. Nazeeruddin, J. Maier, M. Gratzel, Angewandte Chemie 2014.

[64] Z. K. Tan, R. S. Moghaddam, M. L. Lai, P. Docampo, R. Higler, F. Deschler, M. Price, A. Sadhanala, L. M. Pazos, D. Credgington, F. Hanusch, T. Bein, H. J. Snaith, R. H. Friend, Nat Nanotechnol 2014, 9, 687.

[65] Y. H. Kim, H. Cho, J. H. Heo, T. S. Kim, N. Myoung, C. L. Lee, S. H. Im, T. W. Lee, Adv Mater 2015, 27, 1248.

[66] D. Di, K. P. Musselman, G. Li, A. Sadhanala, Y. Ievskaya, Q. Song, Z. K. Tan, M. L. Lai, J. L. MacManus-Driscoll, N. C. Greenham, R. H. Friend, J Phys Chem Lett 2015, 6, 446.

[67] R. L. Hoye, M. R. Chua, K. P. Musselman, G. Li, M. L. Lai, Z. K. Tan, N. C. Greenham, J. L. MacManus-Driscoll, R. H. Friend, D. Credgington, Adv Mater 2015.

[68] F. Deschler, M. Price, S. Pathak, L. E. Klintberg, D. D. Jarausch, R. Higler, S. Huttner, T. Leijtens, S. D. Stranks, H. J. Snaith, M. Atature, R. T. Phillips, R. H. Friend, Journal of Physical Chemistry Letters 2014, 5, 1421.

[69] G. Xing, N. Mathews, S. S. Lim, N. Yantara, X. Liu, D. Sabba, M. Gratzel, S. Mhaisalkar, T. C. Sum, Nat Mater 2014, 13, 476.

[70] Q. Zhang, S. T. Ha, X. Liu, T. C. Sum, Q. Xiong, Nano Lett 2014.

[71] D. Giovanni, H. Ma, J. Chua, M. Gratzel, R. Ramesh, S. Mhaisalkar, N. Mathews, T. C. Sum, Nano Lett 2015, 15, 1553.

[72] A. Kojima, K. Teshima, Y. Shirai, T. Miyasaka, Journal of the American Chemical Society 2009, 131, 6050.

[73] J.-H. Im, C.-R. Lee, J.-W. Lee, S.-W. Park, N.-G. Park, Nanoscale 2011, 3, 4088.

[74] M. M. Lee, J. Teuscher, T. Miyasaka, T. N. Murakami, H. J. Snaith, Science 2012, 338, 643.

[75] M. A. Green, K. Emery, Y. Hishikawa, W. Warta, E. D. Dunlop, Progress in photovoltaics: research and applications 2015, 23, 1.

[76] T. Baikie, Y. Fang, J. M. Kadro, M. Schreyer, F. Wei, S. G. Mhaisalkar, M. Graetzel, T. J. White, Journal of Materials Chemistry A 2013, 1, 5628.

[77] M. R. Filip, G. E. Eperon, H. J. Snaith, F. Giustino, Nature communications 2014, 5.

[78] L. Etgar, P. Gao, Z. Xue, Q. Peng, A. K. Chandiran, B. Liu, M. K. Nazeeruddin, M. Gratzel, J Am Chem Soc 2012, 134, 17396.

[79] C. C. Stoumpos, C. D. Malliakas, M. G. Kanatzidis, Inorganic chemistry 2013, 52, 9019.

[80] P. Umari, E. Mosconi, F. De Angelis, Scientific reports 2014, 4.

[81] W. Geng, L. Zhang, Y.-N. Zhang, W.-M. Lau, L.-M. Liu, The Journal of Physical Chemistry C 2014, 118, 19565.

[82] M.-H. Du, Journal of Materials Chemistry A 2014, 2, 9091.

[83] S. D. Stranks, G. E. Eperon, G. Grancini, C. Menelaou, M. J. Alcocer, T. Leijtens, L. M. Herz, A. Petrozza, H. J. Snaith, Science 2013, 342, 341.

[84] Q. Dong, Y. Fang, Y. Shao, P. Mulligan, J. Qiu, L. Cao, J. Huang, Science 2015, 347, 967.

[85] J. M. Frost, K. T. Butler, F. Brivio, C. H. Hendon, M. van Schilfgaarde, A. Walsh, Nano Lett 2014, 14, 2584.

[86] S. Y. Yang, J. Seidel, S. J. Byrnes, P. Shafer, C. H. Yang, M. D. Rossell, P. Yu, Y. H. Chu, J. F. Scott, J. W. Ager, 3rd, L. W. Martin, R. Ramesh, Nat Nanotechnol 2010, 5, 143.

[87] I. Grinberg, D. V. West, M. Torres, G. Gou, D. M. Stein, L. Wu, G. Chen, E. M. Gallo, A. R. Akbashev, P. K. Davies, J. E. Spanier, A. M. Rappe, Nature 2013, 503, 509.

[88] S. Liu, F. Zheng, N. Z. Koocher, H. Takenaka, F. G. Wang, A. M. Rappe, Journal of Physical Chemistry Letters 2015, 6, 693.

[89] H. Zhu, Y. Fu, F. Meng, X. Wu, Z. Gong, Q. Ding, M. V. Gustafsson, M. T. Trinh, S. Jin, X. Y. Zhu, Nat Mater 2015.

[90] L. Dou, Y. M. Yang, J. You, Z. Hong, W. H. Chang, G. Li, Y. Yang, Nature communications 2014, 5, 5404.

[91] Y. Guo, C. Liu, H. Tanaka, E. Nakamura, J Phys Chem Lett 2015, 6, 535.

[92] X. Hu, X. Zhang, L. Liang, J. Bao, S. Li, W. Yang, Y. Xie, Advanced Functional Materials 2014, n/a.

[93] S. Yakunin, M. Sytnyk, D. Kriegner, S. Shrestha, M. Richter, G. J. Matt, H. Azimi, C. J. Brabec, J. Stangl, M. V. Kovalenko, W. Heiss, Nature Photonics 2015.

[94] Y. Fang, Q. Dong, Y. Shao, Y. Yuan, J. Huang, Nature Photonics 2015.

[95] M. Hirasawa, T. Ishihara, T. Goto, K. Uchida, N. Miura, Physica B: Condensed Matter 1994, 201, 427.

[96] C. Zhang, D. Sun, C. X. Sheng, Y. X. Zhai, K. Mielczarek, A. Zakhidov, Z. V. Vardeny, Nature Physics 2015, 11, 428.

[97] Y. C. Hsiao, T. Wu, M. Li, B. Hu, Adv Mater 2015, 27, 2899.

[98] B. Hu, L. Yan, M. Shao, Advanced Materials 2009, 21, 1500.

[99] F. Ito, T. Ikoma, K. Akiyama, A. Watanabe, S. Tero-Kubota, The journal of physical chemistry. B 2005, 109, 8707.

[100] J. Kalinowski, M. Cocchi, D. Virgili, P. Di Marco, V. Fattori, Chemical Physics Letters 2003, 380, 710.

[101] J. Wang, A. Chepelianskii, F. Gao, N. C. Greenham, Nature communications 2012, 3, 1191.

[102] T. L. Francis, Ö. Mermer, G. Veeraraghavan, M. Wohlgenannt, New Journal of Physics 2004, 6, 185.

[103] B. Hu, Y. Wu, Nat Mater 2007, 6, 985.

[104] P. Janssen, M. Cox, S. H. Wouters, M. Kemerink, M. M. Wienk, B. Koopmans, Nature communications 2013, 4, 2286.

[105] S. Ren, M. Wuttig, Adv Mater 2012, 24, 724.

[106] J. Lohrman, Y. Liu, S. Duan, X. Zhao, M. Wuttig, S. Ren, Adv Mater 2012, 25, 783.

[107] P. Shakya, P. Desai, T. Kreouzis, W. P. Gillin, S. M. Tuladhar, A. M. Ballantyne, J. Nelson, Journal of Physics: Condensed Matter 2008, 20, 452203.

[108] Z. Xu, B. Hu, Advanced Functional Materials 2008, 18, 2611.

[109] H. Tajima, M. Miyakawa, H. Isozaki, M. Yasui, N. Suzuki, M. Matsuda, Synthetic Metals 2010, 160, 256.

[110] E. L. Frankevich, A. A. Lymarev, I. I. Sokolik, F. E. Karasz, S. Blumstengel, R. H. Baughman, H. H. Horhold, Physical review. B, Condensed matter 1992, 46, 9320.

[111] H. Zang, L. Yan, M. Li, L. He, Z. Gai, I. Ivanov, M. Wang, L. Chiang, A. Urbas, B. Hu, Scientific reports 2013, 3, 2812.

[112] B. Brocklehurst, R. Dixon, E. Gardy, V. Lopata, M. Quinn, A. Singh, F. Sargent, Chemical Physics Letters 1974, 28, 361.

[113] N. J. Turro, B. Kraeutler, Accounts of Chemical Research 1980, 13, 369.

[114] J. Kalinowski, J. Szmytkowski, W. Stampor, Chemical Physics Letters 2003, 378, 380.

[115] M. Wohlgenannt, Z. Vardeny, J Phys-Condens Mat 2003, 15, R83.

[116] S. Kersten, Schellekens, A., Koopmans, B., Bobbert, P., Physical Review Letters 2011, 106.

[117] G. H.-M. Tho D. Nguyen, Fujian Wang, Leonard Wojcik, Xiao-Guang Li, Eitan Ehrenfreund & Z. Valy Vardeny, Nature Materials 2010, 9, 345.

[118] L. He, M. Li, A. Urbas, B. Hu, Adv Mater 2014, 26, 3956.

[119] B. Hu, L. Yan, M. Shao, Advanced materials 2009, 21, 1500.

[120] J. Kalinowski, J. Szmytkowski, W. Stampor, Chemical physics letters 2003, 378, 380.

[121] L. He, M. Li, A. Urbas, B. Hu, Advanced materials 2014, 26, 3956.

[122] H. Zang, Y. Liang, L. Yu, B. Hu, Advanced Energy Materials 2011, 1, 923.

[123] L. E. H. V. Alek Dediu, Ilaria Bergenti & Carlo Taliani, Nature Materials 2009, 8, 707.

[124] L. J. A. Koster, V. D. Mihailetchi, R. Ramaker, P. W. Blom, Applied Physics Letters 2005, 86, 123509.

[125] K. T. McCarthy, A. F. Hebard, S. B. Arnason, Physical Review Letters 2003, 90.

[126] M. Fiebig, Journal of Physics D-Applied Physics 2005, 38, R123.

[127] G. Catalan, Applied Physics Letters 2006, 88, 102902.

[128] D. O'Neill, R. Bowman, J. Gregg, Applied Physics Letters 2000, 77, 1520.

[129] Y. Zhang, T. P. Basel, B. R. Gautam, X. Yang, D. J. Mascaro, F. Liu, Z. V. Vardeny, Nature communications 2012, 3, 1043.

[130] H. Zang, J. Wang, M. Li, L. He, Z. Liu, D. Zhang, B. Hu, The journal of physical chemistry. B 2013, 117, 14136.

[131] J. H. Burroughes, D. D. C. Bradley, A. R. Brown, R. N. Marks, K. Mackay, R. H. Friend, P. L. Burns, A. B. Holmes, Nature 1990, 347, 539.

[132] T. W. Ng, M. F. Lo, M. K. Fung, W. J. Zhang, C. S. Lee, Adv Mater 2014, 26, 5569.

[133] A. W. Hains, Z. Liang, M. A. Woodhouse, B. A. Gregg, Chemical reviews 2010, 110, 6689.

[134] T. D. Nguyen, G. Hukic-Markosian, F. Wang, L. Wojcik, X. G. Li, E. Ehrenfreund, Z. V. Vardeny, Nat Mater 2010, 9, 345.

[135] H. Jarrett, W. Cloud, R. Bouchard, S. Butler, C. Frederick, J. Gillson, Physical Review Letters 1968, 21, 617.

[136] J. M. Coey, M. Venkatesan, C. B. Fitzgerald, Nat Mater 2005, 4, 173.

[137] L. Nicole, C. Laberty-Robert, L. Rozes, C. Sanchez, Nanoscale 2014, 6, 6267.

[138] O. Riou, B. Lonetti, P. Davidson, R. P. Tan, B. Cormary, A. F. Mingotaud, E. Di Cola, M. Respaud, B. Chaudret, K. Soulantica, M. Mauzac, The journal of physical chemistry. B 2014, 118, 3218.

[139] M. Blanchard-Desce, R. Wortmann, S. Lebus, J.-M. Lehn, P. Krämer, Chemical Physics Letters 1995, 243, 526.

[140] L. Yan, M. Wang, N. P. Raju, A. Epstein, L. S. Tan, A. Urbas, L. Y. Chiang, B. Hu, J Am Chem Soc 2012, 134, 3549.

[141] I. V. Tolstov, A. V. Belov, M. G. Kaplunov, I. K. Yakuschenko, N. G. Spitsina, M. M. Triebel, E. L. Frankevich, Journal of Luminescence 2005, 112, 368.

[142] D. Beljonne, Z. Shuai, R. H. Friend, J. L. Brédas, The Journal of Chemical Physics 1995, 102, 2042.

[143] R. N. Dixon, M. R. Gunson, Journal of Molecular Spectroscopy 1983, 101, 369.

[144] A. K. Kundu, R. Ranjith, V. Pralong, V. Caignaert, B. Raveau, Journal of Materials Chemistry 2008, 18, 4280.

[145] G. Lawes, A. P. Ramirez, C. M. Varma, M. A. Subramanian, Phys Rev Lett 2003, 91, 257208.

[146] A. Kumar, K. L. Yadav, Materials Science and Engineering B-Advanced Functional Solid-State Materials 2011, 176, 227.

[147] C. Tengstedt, W. Osikowicz, W. R. Salaneck, I. D. Parker, C.-H. Hsu, M. Fahlman, Applied Physics Letters 2006, 88, 053502.

[148] S. Braun, W. Osikowicz, Y. Wang, W. Salaneck, Organic Electronics 2007, 8, 14.

[149] W. Osikowicz, M. P. de Jong, W. R. Salaneck, Advanced Materials 2007, 19, 4213.

[150] M. Wohlgenannt, K. Tandon, S. Mazumdar, S. Ramasesha, Z. V. Vardeny, Nature 2001, 409, 494.

[151] L. Onsager, Physical Review 1938, 54, 554.

[152] W. Wagemans, B. Koopmans, physica status solidi (b) 2011, 248, 1029.

[153] Ö. Mermer, G. Veeraraghavan, T. Francis, Y. Sheng, D. Nguyen, M. Wohlgenannt, A. Köhler, M. Al-Suti, M. Khan, Physical Review B 2005, 72.

[154] S. van Reenen, S. P. Kersten, S. H. W. Wouters, M. Cox, P. Janssen, B. Koopmans, P. A. Bobbert, M. Kemerink, Physical Review B 2013, 88.

[155] M. P. Singh, K. D. Truong, P. Fournier, Applied Physics Letters 2007, 91, 042504.

[156] G. A. Smolenskii, Soviet Physics-Solid State 1962, 4, 807.

[157] M. X. Li, H. F. Wang, L. He, H. D. Zang, H. X. Xu, B. Hu, Applied Physics Letters 2014, 105, 023302.

[158] S. De, T. Pascher, M. Maiti, K. G. Jespersen, T. Kesti, F. Zhang, O. Inganas, A. Yartsev, V. Sundstrom, J Am Chem Soc 2007, 129, 8466.

[159] X. Y. Zhu, Q. Yang, M. Muntwiler, Accounts Chem Res 2009, 42, 1779.

[160] F. J. Wang, H. Bassler, Z. V. Vardeny, Phys Rev Lett 2008, 101, 236805.

[161] T. D. Nguyen, E. Ehrenfreund, Z. V. Vardeny, Science 2012, 337, 204.

[162] D. N. Congreve, J. Lee, N. J. Thompson, E. Hontz, S. R. Yost, P. D. Reusswig, M. E. Bahlke, S. Reineke, T. Van Voorhis, M. A. Baldo, Science 2013, 340, 334.

[163] A. H. Devir-Wolfman, B. Khachatryan, B. R. Gautam, L. Tzabary, A. Keren, N. Tessler, Z. V. Vardeny, E. Ehrenfreund, Nature communications 2014, 5, 4529.

[164] M. Li, M. Wang, L. He, Y.-C. Hsiao, Q. Liu, H. Xu, T. Wu, L. Yan, L.-S. Tan, A. Urbas, L. Y. Chiang, B. Hu, Advanced Electronic Materials 2015, 1, n/a.

[165] T. Moorsom, M. Wheeler, T. Mohd Khan, F. Al Ma'Mari, C. Kinane, S. Langridge, D. Ciudad, A. Bedoya-Pinto, L. Hueso, G. Teobaldi, V. K. Lazarov, D. Gilks, G. Burnell, B. J. Hickey, O. Cespedes, Physical Review B 2014, 90.

[166] S. Steil, N. Großmann, M. Laux, A. Ruffing, D. Steil, M. Wiesenmayer, S. Mathias, O. L. A. Monti, M. Cinchetti, M. Aeschlimann, Nature Physics 2013, 9, 242.

[167] K. V. Raman, A. M. Kamerbeek, A. Mukherjee, N. Atodiresei, T. K. Sen, P. Lazic, V. Caciuc, R. Michel, D. Stalke, S. K. Mandal, S. Blugel, M. Munzenberg, J. S. Moodera, Nature 2013, 493, 509.

[168] N. Atodiresei, J. Brede, P. Lazic, V. Caciuc, G. Hoffmann, R. Wiesendanger, S. Blugel, Physical Review Letters 2010, 105.

[169] T. Methfessel, S. Steil, N. Baadji, N. Grossmann, K. Koffler, S. Sanvito, M. Aeschlimann, M. Cinchetti, H. J. Elmers, Physical Review B 2011, 84.

[170] C. Barraud, P. Seneor, R. Mattana, S. Fusil, K. Bouzehouane, C. Deranlot, P. Graziosi, L. Hueso, I. Bergenti, V. Dediu, F. Petroff, A. Fert, Nature Physics 2010, 6, 615.

[171] H. Vita, S. Bottcher, P. Leicht, K. Horn, A. B. Shick, F. Maca, Physical Review B 2014, 90.

[172] E. Annese, F. Casolari, J. Fujii, G. Rossi, Physical Review B 2013, 87.

[173] Y. J. Hsu, Y. L. Lai, C. H. Chen, Y. C. Lin, H. Y. Chien, J. H. Wang, T. N. Lam, Y. L. Chan, D. H. Wei, H. J. Lin, C. T. Chen, Journal of Physical Chemistry Letters 2013, 4, 310.

[174] M. Callsen, V. Caciuc, N. Kiselev, N. Atodiresei, S. Blugel, Phys Rev Lett 2013, 111, 106805.

[175] G. Nenert, U. Adem, E. M. Bauer, C. Bellitto, G. Righini, T. T. M. Palstra, Physical Review B 2008, 78, 054443.

[176] B. K. Shaw, S. K. Saha, Journal of Physical Chemistry C 2012, 116, 20700.

[177] M. Cinchetti, S. Neuschwander, A. Fischer, A. Ruffing, S. Mathias, J. P. Wustenberg, M. Aeschlimann, Phys Rev Lett 2010, 104, 217602.

[178] A. R. Rocha, V. M. Garcia-Suarez, S. W. Bailey, C. J. Lambert, J. Ferrer, S. Sanvito, Nat Mater 2005, 4, 335.

[179] N. J. Thompson, E. Hontz, D. N. Congreve, M. E. Bahlke, S. Reineke, T. Van Voorhis, M. A. Baldo, Adv Mater 2014, 26, 1366.

[180] M. Shao, L. Yan, M. X. Li, I. Ilia, B. Hu, Journal of Materials Chemistry C 2013, 1, 1330.

[181] Z. S. Romanova, K. Deshayes, P. Piotrowiak, Journal of the American Chemical Society 2001, 123, 2444.

[182] J. Burschka, N. Pellet, S. J. Moon, R. Humphry-Baker, P. Gao, M. K. Nazeeruddin, M. Gratzel, Nature 2013, 499, 316.

[183] H. Zhou, Q. Chen, G. Li, S. Luo, T. B. Song, H. S. Duan, Z. Hong, J. You, Y. Liu, Y. Yang, Science 2014, 345, 542.

[184] J. Y. Jeng, K. C. Chen, T. Y. Chiang, P. Y. Lin, T. D. Tsai, Y. C. Chang, T. F. Guo, P. Chen, T. C. Wen, Y. J. Hsu, Advanced Materials 2014, 26, 4107.

[185] Q. Wang, Y. Shao, Q. Dong, Z. Xiao, Y. Yuan, J. Huang, Energy & Environmental Science 2014, 7, 2359.

[186] P.-W. Liang, C.-Y. Liao, C.-C. Chueh, F. Zuo, S. T. Williams, X.-K. Xin, J. Lin, A. K. Y. Jen, Advanced Materials 2014, 26, n/a.

[187] P. Docampo, J. M. Ball, M. Darwich, G. E. Eperon, H. J. Snaith, Nature communications 2013, 4, 2761.

[188] M. A. Loi, J. C. Hummelen, Nature materials 2013, 12, 1087.

[189] A. Y. Olga Malinkiewicz, Yong Hui Lee, Guillermo Mínguez Espallargas, Michael Graetzel, Mohammad K. Nazeeruddin & Henk J. Bolink, Nature Photonics 2014, 8, 128.

[190] D. L. T. L. Kelly, Nature Photonics 2014, 8, 133.

[191] J. You, Z. Hong, Y. M. Yang, Q. Chen, M. Cai, T. B. Song, C. C. Chen, S. Lu, Y. Liu, H. Zhou, Y. Yang, ACS Nano 2014, 8, 1674.

[192] S. Y. Sun, T. Salim, N. Mathews, M. Duchamp, C. Boothroyd, G. C. Xing, T. C. Sum, Y. M. Lam, Energy & Environmental Science 2014, 7, 399.

[193] K. Tanaka, T. Takahashi, T. Ban, T. Kondo, K. Uchida, N. Miura, Solid State Communications 2003, 127, 619.

[194] T. C. Sum, N. Mathews, Energy & Environmental Science 2014, 7, 2518.

[195] M. Hu, C. Bi, Y. Yuan, Z. Xiao, Q. Dong, Y. Shao, J. Huang, Small 2015, 11, 2164.

[196] J. Even, L. Pedesseau, C. Katan, The Journal of Physical Chemistry C 2014, 118, 11566.

[197] H. Y. Hsu, C. Y. Wang, A. Fathi, J. W. Shiu, C. C. Chung, P. S. Shen, T. F. Guo, P. Chen, Y. P. Lee, E. W. Diau, Angewandte Chemie 2014, 53, 9339.

[198] V. D'Innocenzo, G. Grancini, M. J. Alcocer, A. R. Kandada, S. D. Stranks, M. M. Lee, G. Lanzani, H. J. Snaith, A. Petrozza, Nature communications 2014, 5, 3586.

[199] C. Sheng, C. Zhang, Y. Zhai, K. Mielczarek, W. Wang, W. Ma, A. Zakhidov, Z. V. Vardeny, Physical Review Letters 2015, 114.

[200] K. G. Stamplecoskie, J. S. Manser, P. V. Kamat, Energy Environ. Sci. 2015, 8, 208.

[201] Y. Yamada, T. Nakamura, M. Endo, A. Wakamiya, Y. Kanemitsu, J Am Chem Soc 2014, 136, 11610.

[202] J. S. M. P. V. Kamat, in Nature Photonics, Vol. 8, 2014, 737.

[203] W. Zhang, M. Saliba, S. D. Stranks, Y. Sun, X. Shi, U. Wiesner, H. J. Snaith, Nano letters 2013, 13, 4505.

[204] K. Tanaka, T. Takahashi, T. Ban, T. Kondo, K. Uchida, N. Miura, Solid state communications 2003, 127, 619.

[205] C. Sheng, C. Zhang, Y. Zhai, K. Mielczarek, W. Wang, W. Ma, A. Zakhidov, Z. V. Vardeny, Phys Rev Lett 2015, 114, 116601.

[206] A. Marchioro, J. Teuscher, D. Friedrich, M. Kunst, R. van de Krol, T. Moehl, M. Gratzel, J. E. Moser, Nature Photonics 2014, 8, 250.

[207] W. S. Yang, J. H. Noh, N. J. Jeon, Y. C. Kim, S. Ryu, J. Seo, S. I. Seok, Science 2015.

[208] S. Yakunin, L. Protesescu, F. Krieg, M. I. Bodnarchuk, G. Nedelcu, M. Humer, G. De Luca, M. Fiebig, W. Heiss, M. V. Kovalenko, Nature communications 2015, 6, 8056.

[209] B. R. Sutherland, S. Hoogland, M. M. Adachi, C. T. Wong, E. H. Sargent, ACS Nano 2014, 8, 10947.

[210] M. Kepenekian, R. Robles, C. Katan, D. Sapori, L. Pedesseau, J. Even, ACS Nano 2015.

[211] M. Kim, J. Im, A. J. Freeman, J. Ihm, H. Jin, Proceedings of the National Academy of Sciences of the United States of America 2014, 111, 6900.

[212] F. Zheng, L. Z. Tan, S. Liu, A. M. Rappe, Nano Lett 2015.

[213] A. Stroppa, D. Di Sante, P. Barone, M. Bokdam, G. Kresse, C. Franchini, M. H. Whangbo, S. Picozzi, Nature communications 2014, 5, 5900.

[214] S. Lach, A. Altenhof, K. Tarafder, F. Schmitt, M. E. Ali, M. Vogel, J. Sauther, P. M. Oppeneer, C. Ziegler, Advanced Functional Materials 2012, 22, 989.

[215] T. Kimura, T. Goto, H. Shintani, K. Ishizaka, T. Arima, Y. Tokura, Nature 2003, 426, 55.

[216] Y. S. Dedkov, M. Fonin, U. Rudiger, C. Laubschat, Phys Rev Lett 2008, 100, 107602.

[217] J. Kim, S.-C. Lee, S.-H. Lee, K.-H. Hong, The Journal of Physical Chemistry C 2015, 119, 4627.

[218] J. Even, L. Pedesseau, J.-M. Jancu, C. Katan, The Journal of Physical Chemistry Letters 2013, 4, 2999.

[219] A. Amat, E. Mosconi, E. Ronca, C. Quarti, P. Umari, M. K. Nazeeruddin, M. Gratzel, F. De Angelis, Nano Lett 2014, 14, 3608.

VITA

Mingxing Li was born in Xuecheng, Shandong Province, People's Republic of China in September, 1986. He attended the Shandong University in 2004, and received his Bachelor's Degree in Physics from the Department of Physics in 2008. After the graduation, he continued his graduate study in Shandong University and earned his Master's Degree in Physics on condensed matter physics in 2011. In August 2011, he attended the Department of Materials Science and Engineering at University of Tennessee-Knoxville for his Ph. D degree. He has been working on studying the interaction between charge-transfer states in organic semiconducting materials based on magnetic field effects.